Politecnico di Torino

Politecnico di Torino

INGEGNERIA ENERGETICA E NUCLEARE

LM-30

A.a. 2025/2026

Sessione di Laurea Marzo 2026

State of Health (SOH) Analysis of Automotive Lithium-Ion Battery (LIB) Modules for Battery Electric Vehicles (BEVs): Modelling and Experimental Validation

Relatore:

Davide Papurello

Candidato:

Alessandro Thione

Summary

Figure List

Table List

Nomenclature – List of Abbreviation and Symbols

Abbreviation	Description
ASC	Anode Supported Cell
BEV	Battery Electric Vehicle
BESS	Battery Energy Storage System
BMS	Battery Management System
CAES	Compressed Air Energy Storage
CEI	Cathode Electrolyte Interlayer
CL	Composite Electrode
DOD	Depth of Discharge
EC	Ethylene Carbonate
ECM	Equivalent Circuit Model
EChM	Electrochemical Model
EDLC	Electrochemical Double-Layer Capacitor
EIS	Electrochemical Impedance Spectroscopy
EOL	End-of-Life
ESC	Electrolyte Supported Cell
EV	Electric Vehicle
FC	Fuel Cell
FCEV	Fuel Cell Electric Vehicle
GRU	Gated Recurrent Unit
GT	Gas Turbine
HEV	Hybrid Electric Vehicle
ICE	Internal Combustion Engine
IEA	International Energy Agency
LAM	Loss of Active Material
LCA	Life Cycle Assessments
LFP	Lithium Iron Phosphate
LHS	Latent Heat Storage
LIB	Lithium-Ion Battery
LLI	Loss of Lithium Inventory

LSTM	Long Short-Term Memory
MAPE	Mean Absolute Percentage Error
NEDC	New European Driving Cycle
NMC	Nickel Manganese Cobalt
PC	Propylene Carbonate
PHEV	Plug Hybrid Electric Vehicle
PEMFC	Proton Exchange Membrane Fuel Cells
PCM	Phase Change Material
PHS	Pumped Hydro Storage
PV	Photo-Voltaic
P2D	Pseudo-two-Dimensional
RES	Renewable Energy System
RMSE	Root Mean Square Error
SEI	Solid Electrolyte Interphase
SOC	State of Charge
SOH	State of Health
SOFC	Solid Oxide Fuel Cells
SSB	Solid-State Battery
TES	Thermal Energy Storage
WLTP	Worldwide harmonised Light vehicles Test Procedure

Symbol	Description
Q_{tot}	Total discharged capacity of the battery during a cycle [Ah]
ε_0	Vacuum permittivity [F/m]
ε_r	Dielectric constant [-]
I	Discharge current [A]
t	Discharge time [s or h]
c	Capacitance [F]
E_{tot}	Total energy delivered during discharge [Wh or J]
V	Terminal voltage under load [V]
V_{oc}	Open-circuit voltage [V]
V_n	Nominal voltage [V]
V_{cut}	Cut-off voltage [V]
Q_N	Nominal capacity of the battery [Ah]
Q	Thermal Energy [J]
n_{EOL}	Cycle number at End-of-Life (SOH = 80%)
η_{el}	Electric efficiency
p_1	Slope of SOH versus cycle number in linear fit [%/cycle]
p_2	Intercept of SOH versus cycle number in linear fit [%]
C-rate	Normalised current with respect to nominal capacity [1/h]
i	Current density [A/m²]
i_0	Exchange current density [A/m²]
α	Charge transfer coefficient [–]
η	Overpotential [V]
F	Faraday constant [C/mol]
R	Universal gas constant [J/(mol·K)]
T	Absolute temperature [K]
E_k	Kinetic energy of the flywheel [J]
ϕ_s	Potential of solid phase [V]
ϕ_e	Electrolytic potential [V]
U_{eq}	Equilibrium potential of the reaction [V]

ω	Angular speed of the flywheel [rad/s]
n	Rotational speed [rpm]
I_z	Moment of inertia of the flywheel [kg·m²]
ρ	Material density [kg/m³]
k	Number of cycles [-]
R^2	Coefficient of determination
$k(T)$	Degradation coefficient

Abstract

This master thesis investigates different energy storage technologies and their classification according to the storage mechanism and form of energy, with particular emphasis on electrochemical systems. The analysis highlights how battery-based solutions are especially suitable for supporting increased renewable energy penetration in power systems. A review of the main battery families is presented, focusing on their key performance parameters, degradation mechanisms, and safety issues such as thermal runaway and mechanical, electrical, and thermal abuse, together with potential mitigation and improvement strategies. Furthermore, the study introduces the automotive sector with an overview of electric and hybrid vehicles that employ lithium-ion batteries, providing the context for the subsequent analysis of the State of Health (SOH) of automotive lithium-ion battery modules for battery electric vehicles (BEVs). Different SOH estimation and prediction methods are compared, and the most efficient approach in terms of accuracy, computational cost, and experimental feasibility is implemented and experimentally validated on selected battery modules.

Introduction

In 2015, the Paris Agreement set the global ambition of limiting the average temperature rise well below 2°C relative to pre-industrial levels. In addition to realising this goal, it is essential to achieve a deep decarbonisation of the energy and transport sectors, and a key pillar of this transition is the large-scale integration of different renewable energy sources (like wind or solar) together with efficient energy storage solutions [1].

Over time, energy storage technologies have evolved through different approaches: from mechanical ones (e.g. flywheels) to thermal storage systems and nowadays to the most recent electrochemical systems. Regarding renewables, as they penetrate more deeply into power systems, the need for modular, fast and scalable storage increases. Battery energy storage systems (BESS), especially lithium-ion-based ones, have emerged globally as one of the fastest-growing storage technologies. BESS can provide flexibility, smooth supply variability and support grid stability functions such as frequency regulation [2] [3].

In the electrochemical domain, various battery chemistries exist (lead-acid, NiMH, redox-flow). However, lithium-ion batteries (LIBs) have become the dominant choice for mobile and automotive applications thanks to their high energy and power density, long life cycles and a falling cost trend. Nevertheless, they pose safety challenges, related to thermal management, internal short-circuits, overcharge/over-discharge conditions and mechanical abuse. Therefore, ensuring safety in automotive contexts demands strong Battery Management Systems (BMS) and accurate estimation of battery health [4].

The SOH (State of Health) is a critical parameter for battery management. It quantifies the degradation of a battery in comparison to its original capacity, allowing better energy management in hybrid energy systems. There are three main methods to estimate the battery SOH:

1. Experimental/Measurement-based methods: they directly measure capacity decrease; they are accurate but slow.
2. Model-based methods: they use physics-based models or equivalent circuit models and parameter estimation to understand SOH from operating temperature, voltage and current data. These models are promising for online deployment.
3. Machine-learning: they exploit large datasets and use statistical techniques, e.g. Gaussian process regression, to predict SOH from voltage, current and temperature offering flexibility and adaptability.

Due to safety demands, reliability requirements and real-time performance constraints in automotive systems, the comparison and validation of these methods under realistic operating conditions become crucial [5].

Concerning the automotive sector, vehicles can mainly be classified as battery electric vehicles (BEV) or hybrid electric vehicles (HEV). In the first case, the battery pack is the only source of traction energy, making energy capacity and longevity the most important parameters. On the other hand, in the HEV the battery usually supports peak power and regenerative braking, focusing more on power capability and dynamic response.

Therefore, the SOH analysis, concerning thermal constraints and degradation modes, will differ between these two categories.

The aim of the following thesis is to focus on LIB modules intended for automotive BEV applications: first, by reviewing, presenting and selecting the most promising methods for SOH estimation; then, the most relevant method is used to model and validate the test modules by means of experimental analysis, under cycling and appropriate environmental conditions. The final goal is to provide a safe, accurate and practical SOH estimation framework for automotive battery modules.

1. Energy Storage Methods

Historically, energy demand has always increased due to the development of new technologies in different sectors: the First and Second Industrial Revolutions (late 18th century and the 1870s) imposed a new view of processing in the manufacturing sector, which faced the introduction of new sources of energy, namely fossil fuels. The impact on society of these sources has had a major effect on the environment, which has led to the problem of global warming today. In 2015, with the Paris Agreement, the European Commission established new targets for EU Member States to reduce CO2 emissions into the atmosphere and contain greenhouse gas emissions. The goal is to achieve net-zero emissions by 2050 [6].

Nowadays, global energy demand is continuously increasing, and the challenge is to face the decline of fossil fuel supplies, while the urgency of introducing new sustainable energy alternatives has reached a high level. These green energy sources have helped in the transition from a condition in which fossil fuels have been the main source available, to a condition in which their supply and dependence are decreasing. The penetration of clean energy production has therefore played a key role in this process, arriving, in 2023, to a condition in which the global amount of electricity produced by renewable energy sources is around 30%, equal to 8,928 TWh [7].

However, these types of sources are intermittent, and therefore it is difficult to have a continuous supply of energy. For example, solar energy, used in photovoltaic systems, is subject to meteorological conditions, as well as wind turbines, which are vulnerable to changes in wind speed during their operation. Thus, the main problem is the variability of supply and demand over time, which leads to energy waste and high capital costs with systems forced to operate at partial loads for most of the time (*Figure 1*). For this reason, these technologies are expected to play an important role, especially in making renewable sources available and cost-effective in meeting energy demand. Therefore, it is possible to observe a reduction in both energy costs and consumption, as well as investment and maintenance costs and, on the other hand, an increase in energy system flexibility.

The investment cost can be reduced if one of the following solutions is adopted: smart demand management strategies aimed at flattening demand peaks as much as possible; better energy storage allowing to build smaller systems, with a consequent increment in the ability

to operate at a load close to the maximum and storing excess energy in periods of low demand for later use [8].

As highlighted by the UN Sustainable Development Goals (SDGs) in the framework in which water, land and energy interactions are becoming crucially important in the context of sustainable development, there is a need to optimise these interplays to minimize the disadvantageous impacts on the environment while meeting societal and economic demands [9] [10]. In this scenario, pumped hydro storage systems (PHS) have emerged as a valid response to these challenges offering an effective solution to store energy, support the integration of RES (Renewable Energy System), and maintain grid stability while helping in the achievement of multiple SDGs. As *Figure 2* shows, PHS plants are large-scale installations and are among the simplest storage systems available. The upper reservoir is charged during the night, when the energy demand is low: this means that the water is pumped from the bottom up to the top. Vice versa, during the day, when the energy demand reaches its peak, the water is pumped downwards, and its passing activates mechanisms that convert the kinetic motion of a turbine into electricity. This technology comes with some challenges to face: in fact, one of the main constraints is to find a suitable geological formation for energy storage, in which the reservoir can be easily reachable and has a reasonable variable water level to use as storage. In recent years, pumped hydro systems have accounted for 3% of the total installed electricity generation worldwide, and 99% of the electricity storage capacity, which makes them the most used mechanical storage system [11] [12].

Nowadays, most energy storage systems are Li-ion batteries, because of their higher energy capacity and fast response when supply is needed. As reported by the International Energy Agency (IEA) analysis, batteries are described as the fastest-growing clean energy storage technology and highlight their expanding role in both transport and power sectors [13]. As it is possible to observe in *Figure 3*, battery storage was the fastest-growing commercially available energy technology in the power sector in 2023, with deployment more than doubling compared to the previous year.

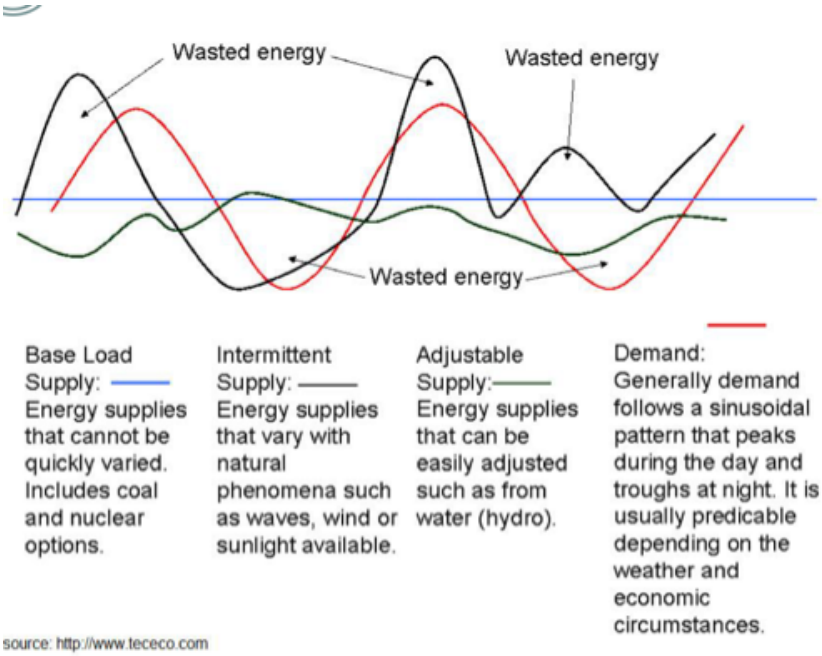

Figure 1 Energy Supply and Demand Mismatch in Power Systems. Source: www.tececo.com

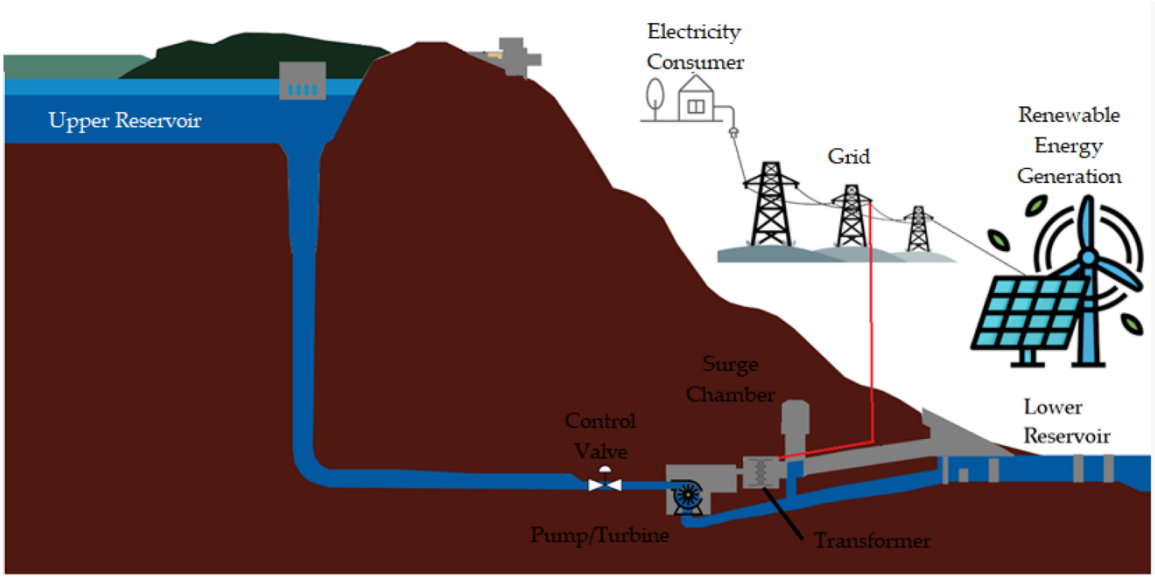

Figure 2 A possible layout of a PHS system [11].

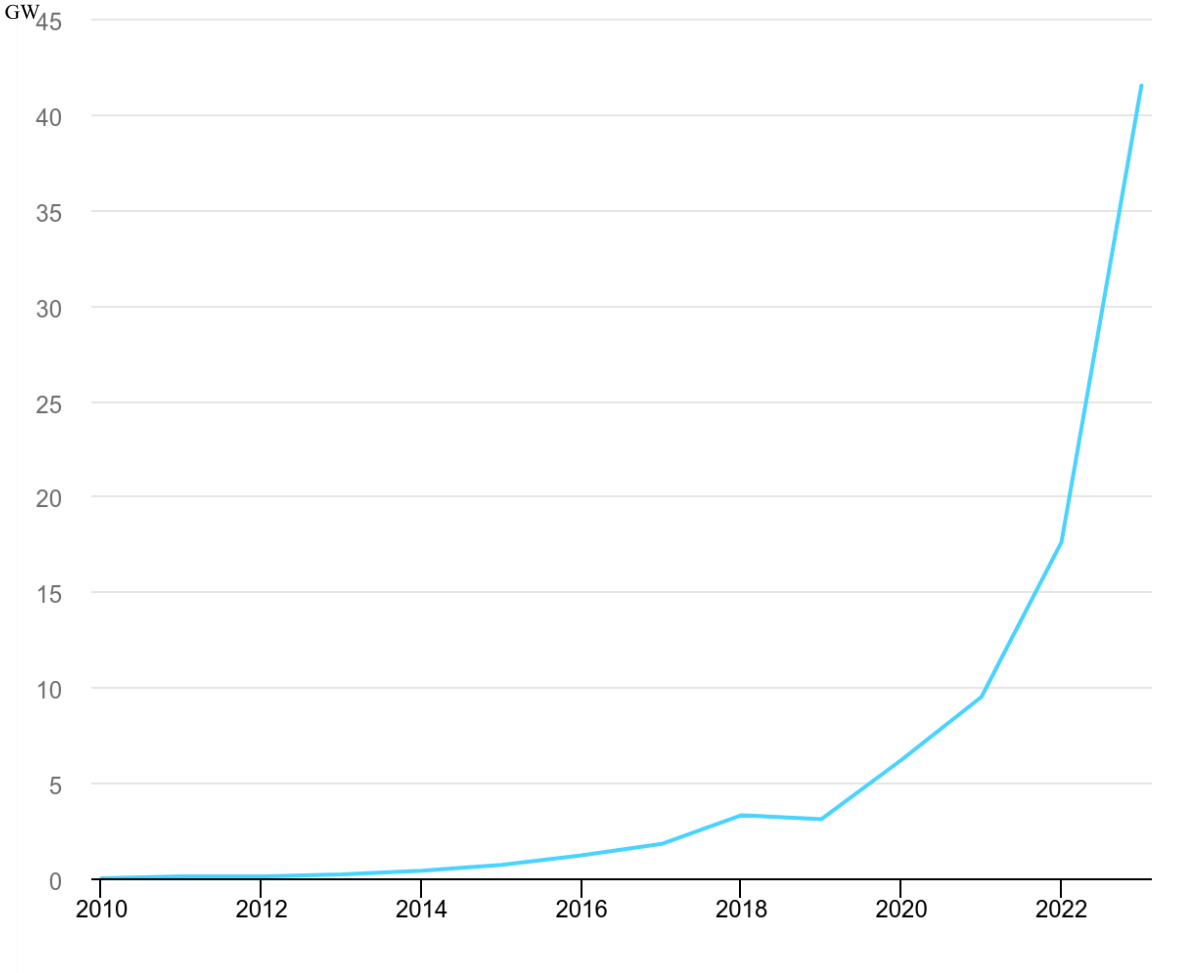

Figure 3 IEA (2024), Global battery storage capacity additions, 2010-2023, IEA, Paris.

1.1 Classification of storage technologies

Energy storage consists of the process of capturing, retaining and subsequently releasing energy when required; in this way, it ensures a more reliable and flexible power supply. In the context of electricity generation, several technologies have been developed to address different operational needs and time scales. Among the most relevant solutions is pumped hydro storage, which remains the most established large-scale method, as mentioned in the previous chapter. However, there are many other storage systems used for electricity generation [14]:

- Mechanical energy storage systems: in this category it is possible to find flywheels, which are one of the simplest energy storage concepts based on significant rotational motion. They are designed to store energy in rotational kinetic form, and since it is a reversible device, the flywheel can work both as a generator and as an alternator

supplying energy to the grid. An application of this technology is the regenerative braking in the transport sector, and it has been analysed that their usage can result in fuel savings of up to 50%, and their round-trip efficiency[1] is about 80-90% [16] [17]. The energy stored can be expressed as follows:

$$E_k = \frac{1}{2} I_z \omega^2 \ [J] \ \ (eq.1)$$

Where ω is the rotational speed of the flywheel equal to $\omega = \frac{2\pi n}{60} \ [\frac{rad}{s}]$ (eq. 2) where n is the velocity expressed in rpm (revolutions per minute); I_z is the moment of inertia, which depends on the reference system; E_k is the kinetic energy produced by the flywheel.

The main problem with this technology is that the amount of energy that can be stored is typically small, and to increase the kinetic energy, either the rotational speed or the moment of inertia must be increased. In the first case, it is not possible to exceed the maximum velocity, gained from the equilibrium condition to translation: $\rho v^2 = \sigma$ (eq. 3), which depends on material properties. Modern flywheels have rotors made of composite materials, work under vacuum conditions, and can have active or non-active magnetic bearings to reduce mechanical friction and vibration. But still, there are inevitable losses concerning aerodynamic and mechanical effects.

Their application can be in full electric vehicles or in combination with a PV (Photo-Voltaic) system, since the most important feature of flywheels is their ability to fully charge or discharge.

Material	Density (kg/m³)	Strength (MN/m²)	Specific strength (MN·m/kg)
Steel (AISI 4340)	7800	1800	0.22
Alloy ($AlMnMg_2$)	2700	600	0.22
Titanium ($TiAl_6V_4$)	4500	1200	0.27
GFRP (60 vol% E-glass)	2000	1600	0.80
CFRP (60 vol% HTC)	1500	2400	1.60

Table 1 Some materials for flywheels and their properties[2], source: ASPES Engineering AG.

[1] The round-trip efficiency (RTE) of a battery is the ratio of useful energy output to useful energy input, expressed as a percentage [15].
[2] GFRP, glass fibre reinforced polymer; CFRP, carbon fibre-reinforced polymer; HTC, heat treated carbon.

Other examples of mechanical storage systems are the so-called CAES (Compressed Air Energy Storage), in which air is compressed and stored in tanks placed underground, typically between 4.0 and 8.2 MPa. The compression process occurs using excess energy from a tertiary electricity production system, which drives a motor that activates a compressor pushing the air into the storage tank. In a second moment, when an energy demand peak is reached, the air is released from the tank and passes through channels that raise the temperature of the stored air before passing through turbines where it is expanded and generates electricity. The main constraint is represented by soil configuration, which allows only a few sites to be prepared to store the tank. It is interesting to highlight the schematic cycle of this technology, where it is possible to see that the CAES cycle is a kind of variation of a gas turbine cycle, in which a reservoir appears as an additional block to the diagram [18].

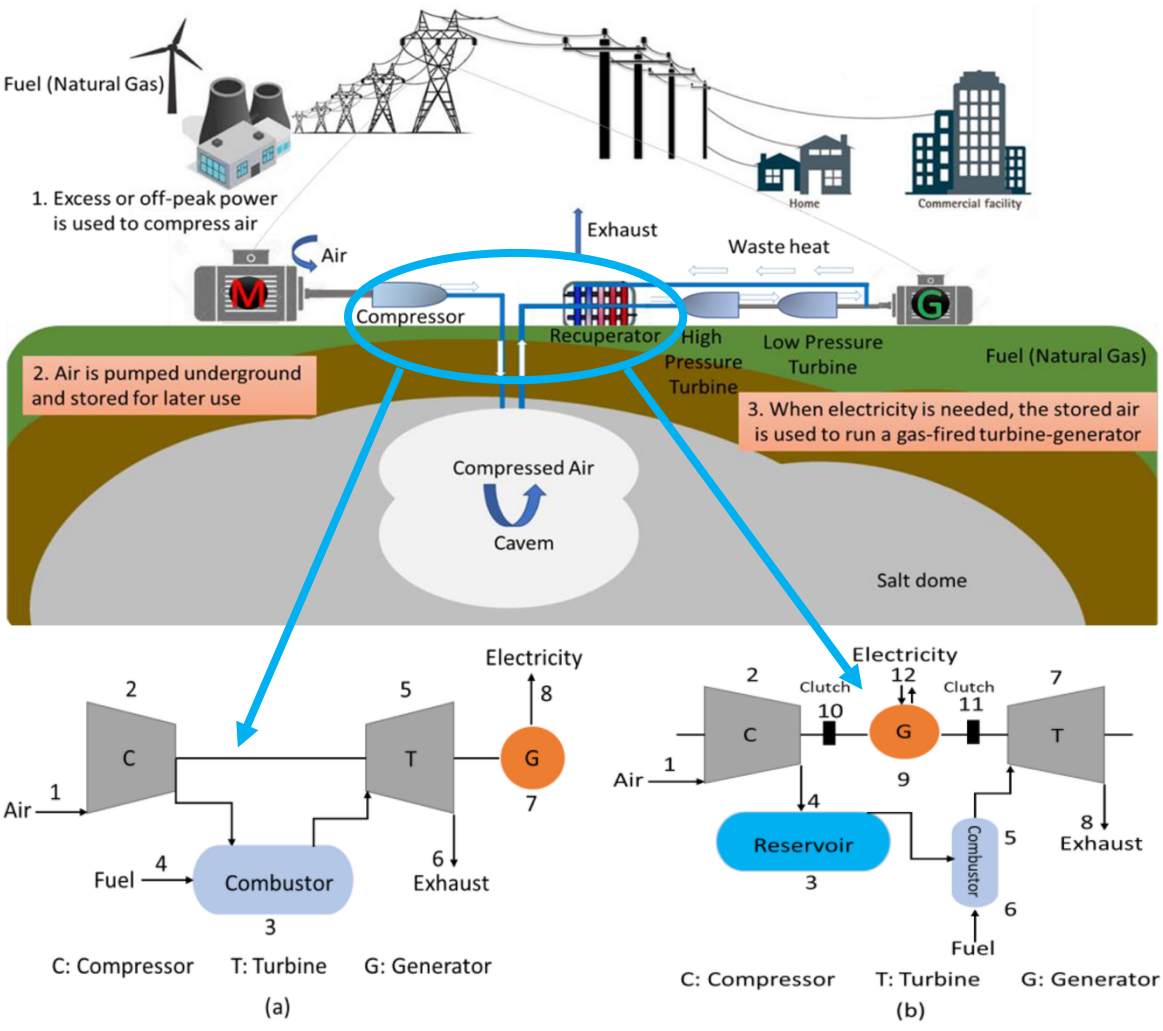

Figure 4 Components of the CAES system. Gas turbine and CAES schematic diagram: (a) schematic diagram of gas turbine system; (b) schematic diagram of storing energy in gas turbine system [18].

- Thermal energy storage (TES) systems are designed to store heat energy by cooling, heating, melting, condensing or vaporising a substance. They are divided into cold storage, in which ice is collected from lakes or rivers and stored in thermally insulated warehouses, sensible heat storage and latent heat storage. The first one stores thermal energy by increasing the temperature of a solid or liquid by a temperature difference (ΔT) without undergoing a phase change. The specific heat capacity of the material determines its ability to store heat, as well as the magnitude of the temperature variation and the required mass of the storage material. The typical tank design of these kinds of TES storages aims at creating and maintaining optimal thermal stratification and thermal insulation from outdoor environment. For domestic hot water use, one of the most common designs is the tank-in-tank configuration, in which the smaller tank inside the larger one is surrounded by a serpentine that is connected to a boiler that supplies energy. This is an example of liquid sensible TES, but as it is possible to gain from *Figure 5,* the other big family is the solid one, where the packed-bed TES are most used. As a matter of fact, they are based on rock materials which are spread in a bed-like structure encircled by two tubes, one for inlet and one for outlet, installed in the storage system and through them the heat exchange takes place (*Figure 6*). During the charging phase, hot air produced by the solar air collector enters the upper section of the storage tank, transferring thermal energy to the rock bed. In the discharging phase, the stored heat is extracted from the rock bed to provide space heating, while the cooled air is redirected to the solar air collector for reuse in the subsequent charging cycle.

  Regarding the rock material, cement can be used due to its low cost, easy availability and processability, and can be integrated with other materials like bricks. Some interesting features of cement are its high specific heat and an advantageous thermal expansion coefficient. Among the constraints, it is important to underline the maximum operating temperature that must be controlled so as not to compromise cement's mechanical properties[3]. Other materials used are rocks, due to their low cost; even if a lower volumetric thermal capacity is obtained compared to water, they have the advantage to work at temperatures higher than 100°C with respect to water and concrete. During operation, rocks can be used in combination with heat pumps.

[3] At 100 °C, cement undergoes a first dehydration ($-130\,\frac{kg_{H_2O}}{m^3}$).

Thanks to the Harry-Thomason method, it is possible to gain both the advantage of the high specific heat of water and large heat transfer surface of a rock bed [20].

In rock beds, important parameters that must be considered are the porosity ε and the packing angle θ.

$$\frac{\pi}{3} \leq \theta \leq \frac{\pi}{2} \quad (eq.4)$$

$$\varepsilon = \frac{Vol_{empty}}{Vol_{tot}} \; [-] \quad (eq.5)$$

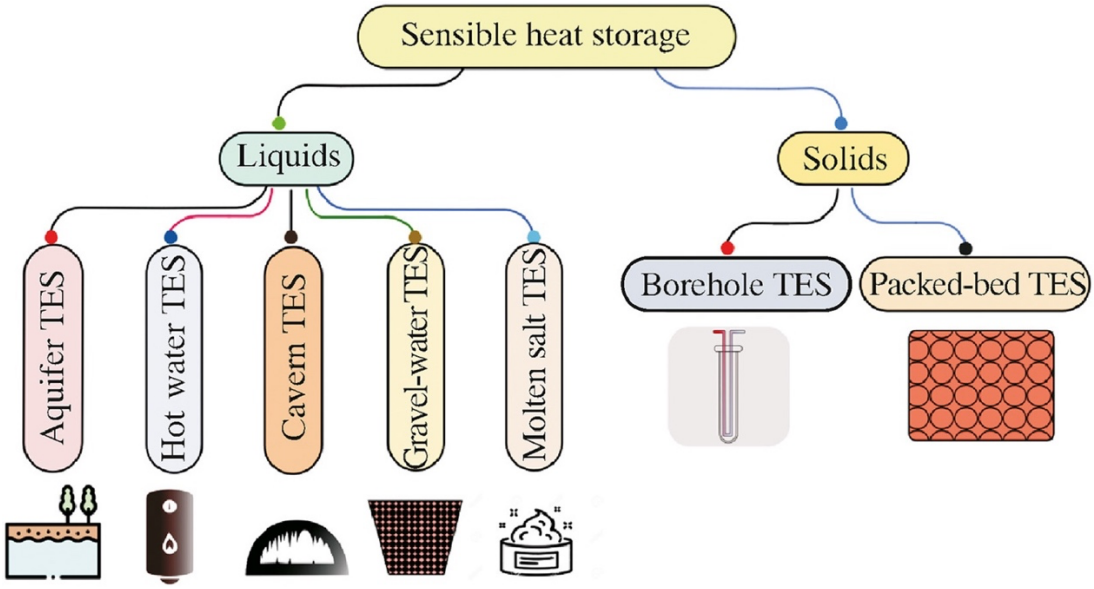

Figure 5 Typologies of Sensible Heat Storages [19].

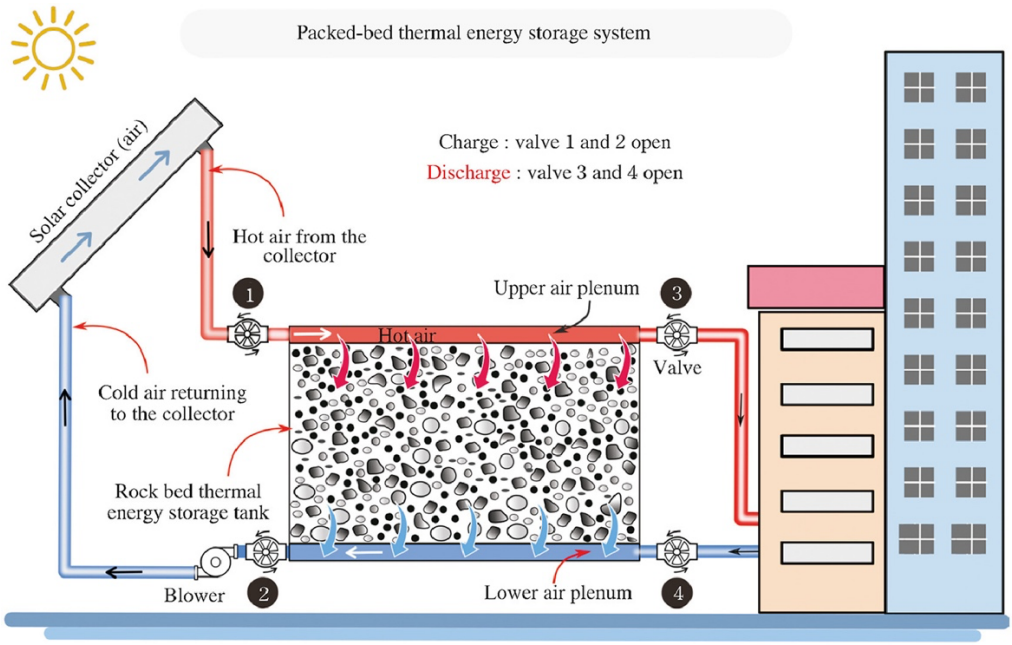

Figure 6 Scheme of packed-bed TES [19].

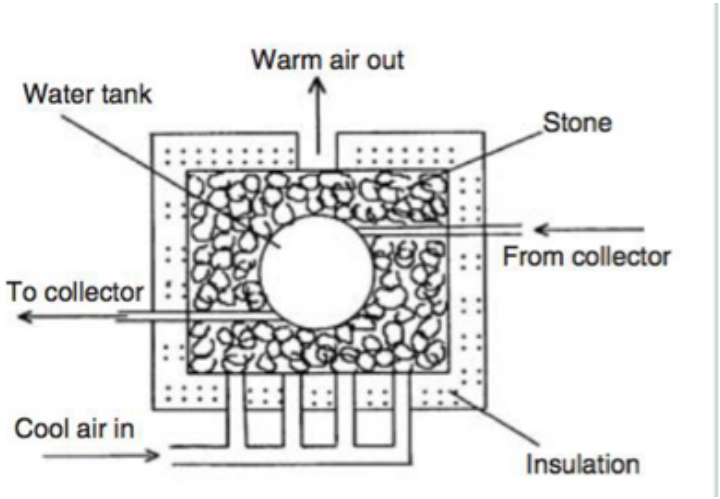

Figure 7 Harry-Thomason rock bed system scheme [20].

In conclusion, latent TES are based on the phase change of a given material, especially its solid and liquid phases, and it is important to note two parameters: the latent heat of solidification $[\frac{kJ}{kg}]$ and the transition temperature. The capacity of the storage material to undergo a phase change at a constant temperature is a key factor influencing the performance of latent heat storage (LHS) systems. *Figure 8* illustrates the phase transition profile of a storage material as heat is added or removed. The diagram shows that, as thermal energy (Q) is supplied, the material initially undergoes a temperature increase within each phase (solid, liquid, and vapour) representing sensible heat storage. Once the phase change temperature is reached,

additional heat input no longer raises the temperature but instead induces a phase transformation, such as melting or vaporisation. Conversely, during cooling, the material releases the stored latent and sensible heat through condensation and solidification processes.

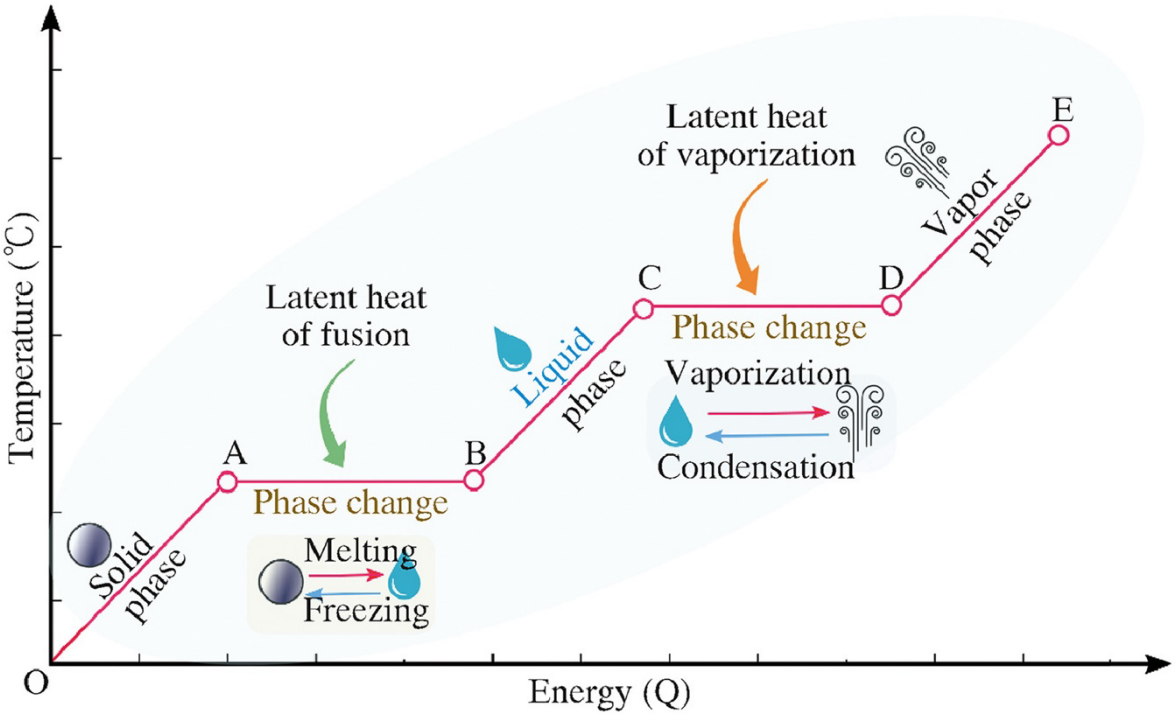

Figure 8 Temperature-Energy diagram for heating and cooling of a substance[4] [19].

The best-known materials in this family are Phase Change Materials (PCM), which provide an effective way of storing thermal energy and offer the advantages of a high thermal energy storage density and an essential isothermal storage process. The fact that PCMs have a wide temperature range in which they solidify and melt makes them suitable for a wide range of applications. As illustrated in *Figure 9*, PCMs are divided by their nature.

[4] Point O: material in the solid phase; Region O–A : sensible heating of material due to heat addition; Region A–B: conversion of material from solid phase to liquid phase due to melting; Region B–C: sensible heating of liquid; Region C–D: liquid-to vapour phase change; Region D–E: sensible heating of the vapour [19]

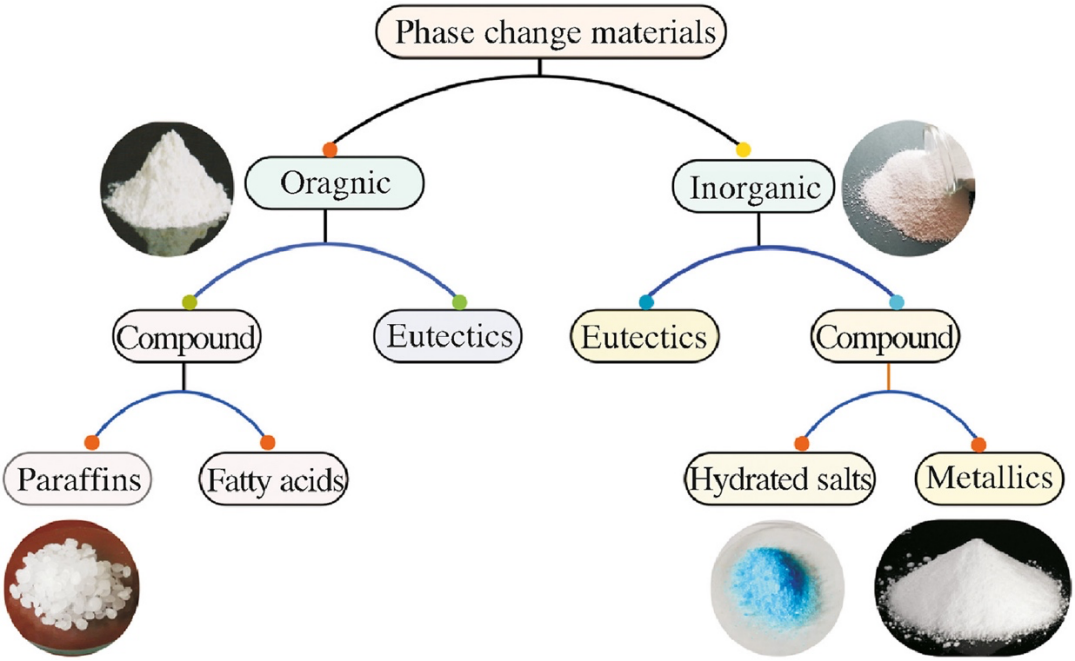

Figure 9 Classification of phase change materials [19].

In the organic category, paraffins at ambient temperature are similar to wax and have molecules with linear structure: $CH_3 - (CH_2)_n - CH_3$, where n varies from 20 to 40. The part containing $(CH_2)_n$ can be engineered to increase the melting temperature. Typically, structures with 14-20 carbon atoms per molecule can be found in a melting temperature range of interest for low temperature TES, from 6°C up to 80°C. Because paraffins have a high specific heat of fusion, they have a higher energy storage capacity. Next, fatty acids are carboxylic acids characterised by a long aliphatic chain, with the general formula $CH_3(CH_2)_{2n}COOH$, where n lies in the range from 12 to 28. They can undergo numerous thermal cycles of freezing and melting without degradation. Fatty acids exhibit superior phase transition properties compared to paraffin wax, although they are more expensive [21]. On the other hand, inorganic materials have a sharp melting point, a high heat of fusion, a high latent heat storage capacity per unit mass, and high thermal conductivity. In this group, hydrated salts are salts that contain molecules of water in the crystallisation process and the ratio between the number of these molecules and the number of ions in the salt is well defined and constant for each hydrated salt. The generic chemical formula is expressed as: $M * nH_2O$, where M is the inorganic salt. Their melting point temperature range goes from 0°C up to 120°C, and they are well known for having the highest storage density, with almost no losses during storage phase [22].

The eutectic salts are in general mixtures of two or more substances whose melting point is less than the one of the individual substances.

Material	Composition (g)	Melting Point (°C)	Latent Heat $\left(\frac{kJ}{kg}\right)$
LiNO3+NH4NO3+NaNO3	2.5+6.5+1	79.5	112
LiNO3+NH4NO3+HNO3	1.77+3.9+1	80.5	114
LiNO3+NH4NO3+NH4Cl	5.4+13.6+1	81.4	109
LiNO3+NH4NO3NaNO3+NaCl	1.77+2.94+1+1	84.4	119

Table 2 Eutectic salts PCM and their properties [23].

- Electrical capacitors are passive components that store electrical energy by accumulating charges on two conductors separated by an insulating material called a dielectric[5]. The key property is the capacitance c, which is determined by plate area, distance between plates, and the type of dielectric: ε_0 is the vacuum permittivity, a constant value of approximately 8.85×10^{-12} F/m; ε_r is the relative permittivity (dielectric constant) of the material filling the gap.

$$c = \frac{\varepsilon_0 \varepsilon_r A}{d} \; [F] \; (eq. 7)$$

The layout of a capacitor is composed of two plates (conductors) with a dielectric material placed between them, like ceramic, glass, plastic or air. When voltage is applied, opposite charges accumulate on the plates, creating an electric field and storing energy in this field. The stored energy can be quickly released when needed, which is why capacitors are used for tasks like filtering, energy storage, and signal coupling in electronic circuits. The following formula expresses the energy stored in a capacitor:

$$E = \frac{1}{2} c \Delta V^2 \; [J] \; (eq. 8)$$

There are many types of capacitors, each of them differs in construction and is chosen for specific applications based on its properties, such as maximum voltage, energy storage, and stability. Capacitors are fundamental in electronic devices for

[5] A dielectric material is a substance that acts as an electrical insulator, meaning it does not conduct electricity, but can store electrical energy when placed in an electric field due to its ability to become polarised internally.

tasks such as smoothing power supply voltage, timing circuits, and blocking direct current while allowing alternating current to pass [24].

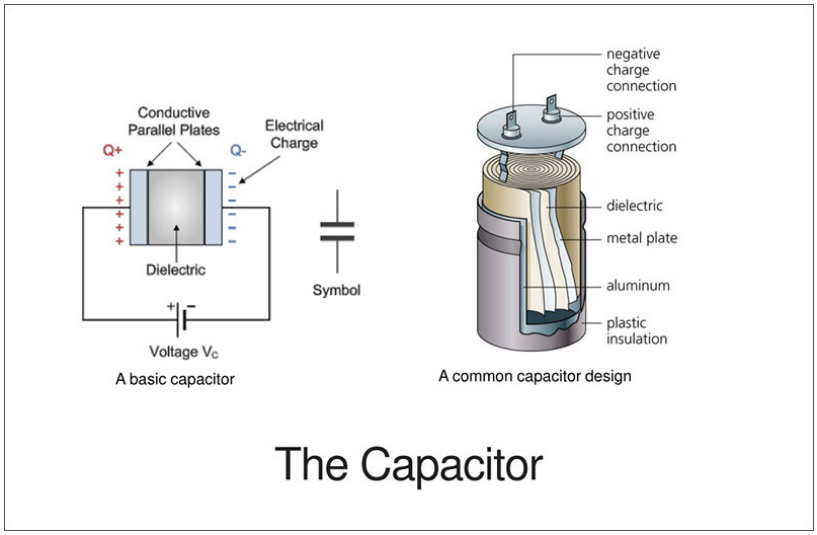

Figure 10 Scheme of a basic capacitor (left) and its common design (right) [25].

An important evolution of capacitors are supercapacitors, which have a higher capacitance, and thus much greater energy storage, than traditional capacitors while enabling rapid charge and discharge cycles. They fill the gap between regular capacitors, which have low energy density but high-power delivery, and batteries, which store more energy but charge/discharge slowly and degrade faster. Supercapacitors can store energy through two main mechanisms: the double-layer capacitance uses an electrostatic charge at the electrode-electrolyte interface, like a traditional capacitor but with electrodes made of porous, high-surface-area materials like activated carbon, and pseudo-capacitance which involves fast, reversible chemical reactions at the surface, allowing additional charge storage. Other important aspects that highlight differences between supercapacitors and batteries are their long cycle life up to millions of cycles, far more than battery cells; their high-power density, 5 to 10 times more than that of batteries, but, on the other hand, a lower energy density [26] [27]. As far as structure is concerned, a supercapacitor's schematic typically features two porous electrodes (often made of carbon materials), separated by a membrane soaked in an electrolyte, enclosed within a cell (*Figure 11*) [28].

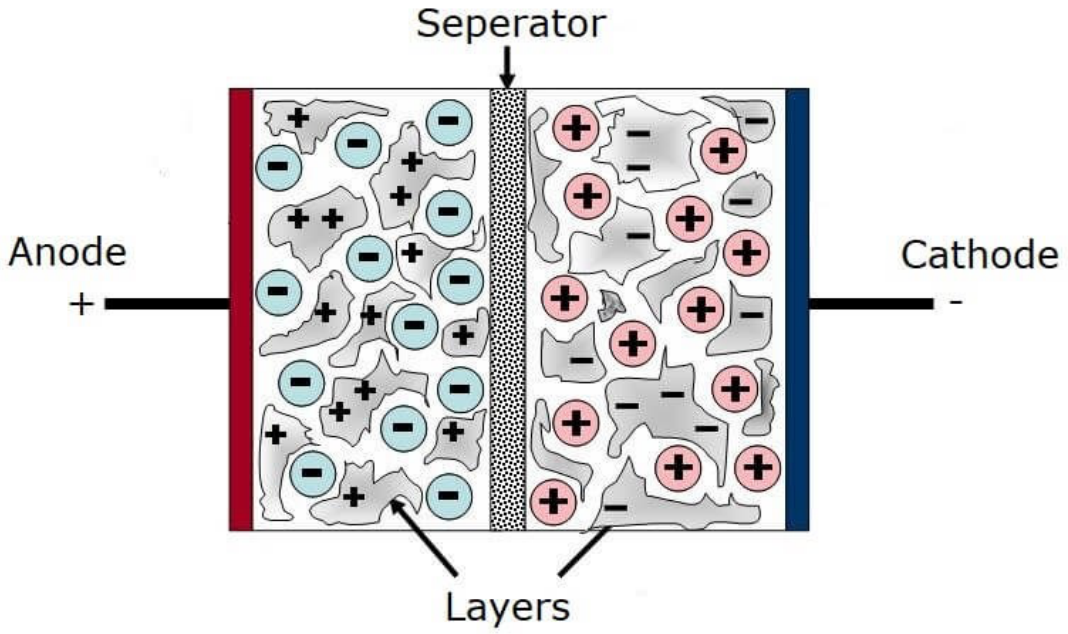

Figure 11 Structure of a supercapacitor [28].

- Batteries are electrochemical devices that convert chemical energy directly into electrical energy and are widely used for energy storage, offering a portable and flexible solution for storing and releasing electrical energy as needed across different applications like renewable energy integration, electric vehicles, and portable electronics. Battery technologies are categorised by their chemical composition and essential mechanisms, which influence their suitability for specific uses based on parameters such as energy density, cycle life, safety, environmental impact, and operational costs. They excel when decentralised, fast-response, or portable energy storage is needed, particularly in balancing grid fluctuations, enabling renewable energy integration, providing backup for critical systems, and powering vehicles and electronics. They outperform other storage types (like pumped hydro or compressed air) in scenarios that require flexibility, rapid discharge, compact size, or deployment independent of geographical constraints. They are characterised by high efficiency (70-80%), but they do not benefit from economies of scale [29] [30]. As *Figure 12* reports, there are many different kinds of batteries that differ in their utilisation and more: for example, lithium-ion batteries are known for high energy density, long cycle life, and efficiency, making them ideal for consumer electronics, electric vehicles, and grid-scale storage, however limitations include safety risks and resource dependency [32]. The lead-acid batteries are cost-effective and robust,

commonly used in backup power and small-scale stationary applications; however, they are heavy, have limited cycle life, and lower energy density compared to Li-ion [33]. Flow batteries (e.g. Vanadium Redox) offer easy scalability, long service life, and suitability for grid balancing and renewable integration; their drawbacks are lower energy density and higher initial costs. Nickel-Cadmium batteries are durable and tolerate deep discharges but are less favoured today due to toxicity and moderate energy density [34].

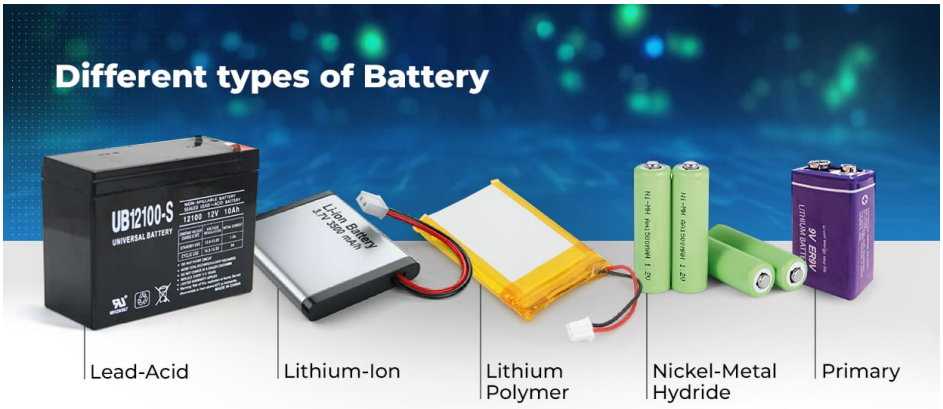

Figure 12 Different types of batteries [31].

System	Lead-Acid	Li-ion	Solid-State
Energy Density	35–40 Wh/kg (1)[6]	150–180 Wh/kg	250–400 Wh/kg
Power Density	250 W/kg	800 W/kg	400–800 W/kg
High Temp. Performance	Up to 50°C	Up to 50°C	Up to 50°C
Low Temp. Performance	Up to –30°C	Up to –20°C	Up to –30°C
Cycle Life	1500–5000	1000–5000	1000–10000
Overall Service Life	15 years	10–15 years	>15 years
Reliability	Proven	Needs to be assessed for longer times	Under development
Sustainability	Excellent	Recovery methods uneconomical	To be established
Safety	Excellent	Issues to be resolved	Improved thermal stability
Cost (battery syst. only)	$150–200/kWh	$600–800/kWh	>$800/kWh (current)

Table 3 Comparison of technical and other features of lead–acid, Li-ion and Solid-State batteries for energy storage service [33].

[6] Note (1): Bipolar lead-acid batteries are being developed which have energy densities in the range from 55 to 60 Wh/kg (120–130 Wh/l) and power densities of up to 1100 W/kg (2000 W/l).

1.2 Evaluating battery technologies against other storage solutions for improved renewable penetration

Batteries play a crucial role in today's global energy landscape and are set to be a key driver of reliable clean energy transitions. In transportation, they are fundamental to powering the millions of electric vehicles sold annually. Within the energy sector, battery storage leads as the fastest-growing clean energy technology. Thanks to their adaptability, batteries can support large-scale utility projects, behind-the-meter[7] storage for homes and businesses, and enable decentralised access to electricity through mini-grids and solar home systems. Additionally, as battery costs continue to decline, electric vehicles and storage solutions are becoming increasingly competitive and attractive in the energy market [35]. In 2023, battery storage capacity reached 42 GW, underlining the unexpected rate of deployment. This phenomenon can be explained by looking at the cost trend and technology improvement: lithium-ion batteries have dominated the market due to rapid cost declines and technical improvements. Since 2010, the cost has fallen by almost 90%, decreasing from around $1,400/kWh to less than $140/kWh in 2023 while, for example, supercapacitors are much more expensive in terms of $/kWh, at $5,000 to $19,000 per kWh for electrochemical double-layer capacitors (EDLCs) in 2025, making them impractical for bulk energy storage [36]. It is important to mention also the faster and easier deployment and application of batteries compared to other energy storages like CAES or pumped hydro: the first are prefabricated and quick to install, whereas the latter often requires years of planning and construction. In addition, batteries are location independent meaning that they can be deployed almost anywhere and do not require specific geographical features, unlike CAES (needs caverns) or pumped hydro (needs elevation). Related to these mechanical aspects, the fast response of batteries is crucial for grid frequency regulation and renewable integration. Mechanical systems like flywheels and CAES may respond quickly but cannot store significant energy for extended durations [37].

The energy in batteries is released through electrochemical reactions, which allows higher energy densities to be achieved: for example, modern Li-ion batteries can reach 250-300 Wh/kg, while supercapacitors typically store just 5-10 Wh/kg. Another aspect is the scalability of chemistry, defined as the ability of a chemical process or system to efficiently

[7] "behind the meter" = residential/commercial

handle an increased workload or to be expanded from a small laboratory scale to a larger industrial scale without losing performance or quality. This scalability, which differs from one battery technology to another (Li-ion, Lithium Iron Phosphate or LFP, flow, lead-acid), allows adjustment based on cost, safety, and performance targets. This flexibility does not exist with purely mechanical or capacitive storage systems [38].

In relation to environmental impact, batteries, especially Li-ion, lead-acid, and flow chemistries, are vital in decarbonising the energy sector by enabling renewable energy storage and replacing fossil-fuel-based backup. Their main positive contributions include grid decarbonisation, in which they facilitate large-scale renewable integration, peak shaving, and grid stability, directly reducing greenhouse gas emissions from power systems and transport sectors. Connected to the last field, fundamental is the support for sustainable transition where the adoption in electric vehicles, marine, and aviation industries supports international decarbonisation targets and United Nations Sustainable Development Goals [40] [41].

Regarding Life Cycle Assessments (LCAs), studies show that Li-ion batteries have lower total impacts (global warming, resource depletion) compared to lead-acid and Nickel-Cadmium batteries, with resource impacts further mitigated by recycling strategies [42]. Compared to batteries, pumped hydropower shows the lowest life cycle greenhouse gas emissions among large-scale options, as long as the environmental impacts associated with initial construction are mitigated [43]. Therefore, their low operational emissions and long lifespan make them more attractive as alternatives to battery-based options in grid-level balancing at utility scale.

On the other hand, supercapacitors can undergo millions of cycles without substantial degradation, such as exfoliation phenomenon, leading to very little need for replacement during their operational lifetime. Their cradle-to-grave LCA is challenged by limited energy density, resulting in a relatively high environmental impact per kWh stored, but extremely low per unit of power delivered [44].

However, challenges in the environmental field persist: the manufacturing phase related to mining and processing of the so-called “critical raw materials”[8], such as cobalt, nickel, lithium and vanadium, which are essential to energy transition, generate emissions and pollution risks that can affect human health through metal contamination in water and soil. Related to this poisoning, another issue is represented by the end-of-life management, where

[8] A critical raw material is defined by the European Union as a raw material that is both of high economic importance and has a high risk of supply disruption. European Commission. (2023). *Critical raw materials*. European Commission.

toxic waste and improper disposal can lead to the same environmental problems. On the contrary, flywheels and supercapacitors generally have a lower environmental impact, given their non-chemical operation and longer life cycles [45].

As is evident from *Table 4*, batteries emerge as the optimal solution for the majority of applications associated with daily utilisation, particularly those pertinent to human-centric operations. This preference arises from their elevated energy density coupled with a competitive cost profile, which is subject to continual reduction through ongoing technological advancements.

Aspect	Batteries (Li-ion, Lead-Acid)	Supercapacitors	CAES & Pumped Hydro	Flywheels
Role	Grid, EV, backup, decentralised access	Power buffer, high-power short-term	Bulk, long-duration, grid	Short-term, frequency reg.
Cost (2023–2025)	$140/kWh (Li-ion, 2023)	$5,000–$19,000/kWh (2025)	Site-dependent	Moderate (depends on size)
Energy Density (Wh/kg)	250–300 (Li-ion)	5–10	Very high	Moderate
Power Density	Good (batteries)	Extremely high	Moderate	High
Cycle Life	Thousands (Li-ion), lower for lead-acid	Millions (very long)	Very long	Very long
Main Limitation	Raw materials, degradation	Low energy density, high cost	Location, construction	Limited storage capacity
Environmental Impact	Mining, pollution, recycling needed	Low emissions per power cycle;	High initial, low op. emissions	Low (mainly manufacturing)

Table 4 Comparative overview of the main characteristics, costs and limitations of different electrical energy storage technologies, including batteries, supercapacitors, CAES and pumped hydro, and flywheels.

2. Types of Batteries

Batteries are mainly divided into three types according to their reversibility and operational principle: primary cells are designed for single use and cannot be easily recharged (e.g. dry cell). They find application in low-drain or sporadically used devices due to their long shelf life and low rates of self-discharge. On the contrary, secondary cells are designed to be recharged (e.g. lead acid, Li-ion) and dominate sectors, requiring repeated cycling, such as consumer electronics, automotive and stationary storage. In conclusion, fuel cells, which are not batteries in the strict sense, need a continuous flux of fuel, for example a hydrogen storage, to convert into electricity and are pivotal where long-duration, high energy conversion is necessary.

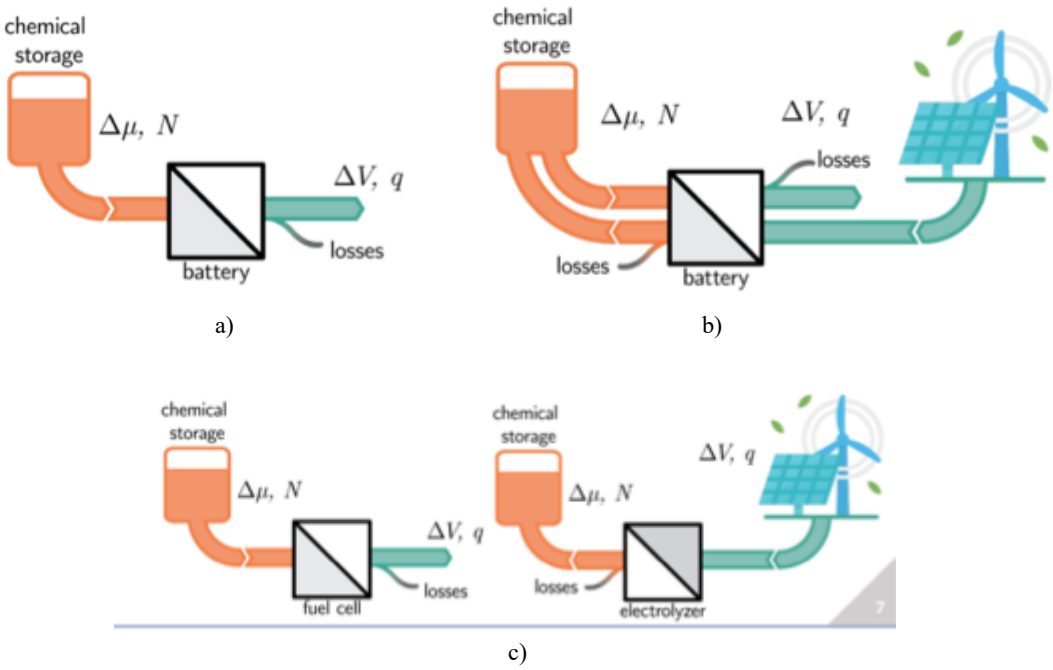

Figure 13 Representation of a) Primary cell, b) Secondary Cell, c) Fuel cells

Within these categories, several chemistries have arisen to serve various technical and economic requirements. Lead-acid batteries, one of the oldest secondary systems, are notable for their low cost and ability to supply high surge currents, which makes them the first choice for automotive starting applications and stationary backup systems. However, their relatively low energy density, significant mass and environmental concerns due to lead content limit their use in portable devices and raise regulatory issues concerning disposal and recycling.

Nickel metal hydride batteries, developed as a safer and less toxic alternative to nickel-cadmium, offer moderate energy density and are better for their eco-friendliness and robust cycle life. They are widely used in hybrid electric vehicles and some consumer electronics but exhibit higher self-discharge rates and a lower cycle life compared to lithium-ion systems, limiting their suitability for high-performance, high-density applications. These types of battery are rechargeable and use Nickel hydroxide as the positive electrode material and hydrogen storage alloy (Metal Hydride) as the negative electrode material.

Lithium-ion batteries are appropriate for a wide range of applications such as electric vehicles, where critical factors are represented by size and weight. They offer a far better energy density than conventional lead-acid batteries. Nowadays, researchers are continuously working to improve the efficiency of current technology in addition to developing new ones. Therefore, there is a crucial need to explore methods that reduce the energy lost during charging and discharging cycles. LIBs have become the energy market's top choice due to a number of essential qualities like high energy density and efficiency, as well as a prolonged life cycle even at high charging and discharging rates. A crucial role is played by the structure of the electrodes materials since it impacts the electrochemical performance as well as the life of the complete battery: concerning the cathode (positive electrode), it allows the intercalation of lithium ions in its crystal lattice (without significant crystal distortion) and has high standard of electrode potential (>Li/ Li^+ =3V), but it represents the bottleneck for the capacity density and typically are made with rare and expensive elements. For this reason, the research direction is oriented towards implementing solutions that are less expensive and include the utilisation of more common materials like Iron (Fe). For the other electrode, the anode (negative electrode), lithium ions can intercalate into its structure, and it has a low standard electrode potential (≈Li/ Li^+ =3V) and, at the moment, are made with graphite and hard carbon. The research direction is set to solve the problem of developing fast charging LIBs by introducing lithium alloys. Then, the electrolyte is placed between anode and cathode: it is characterised by high ion conductivity, thermal and chemical stability, and low toxicity and cost. Nevertheless, it can react with Li^+, forming the so-called Solid Electrolyte Interphase and it shows a low flammable point [46][47].

Redox Flow Batteries are another secondary cell technology that has in common some features with the more traditional fuel cells. A relevant characteristic of these devices

stays in their operation: they use flow of reactants that can assume different states of oxidation, exchanging electrons and ions and, therefore, driving a redox process in both directions. Its structure is characterised by a converter, in which the redox reaction takes place, and it determines the power of the battery. Next there is the vessel, which determines the energy of the process and hosts reactants and products of the mentioned reaction. The most famous real application is the Vanadium-based redox flow battery where are exploited the four oxidation states of Vanadium ($V^{2+}, V^{3+}, V^{4+}, V^{5+}$).

PEMFC (Proton Exchange Membrane Fuel Cells) and SOFC (Solid Oxide Fuel Cells) are the most famous fuel cells. Some relevant features of PEMFC include the electrolyte layer, which consists of a polymeric membrane of Nafion that starts from a backbone of Teflon (CF_2). The Nafion is composed by chain of carbon and fluorine that is then released in form of F^- (very dangerous). An issue of using Nafion is the fact that to allow the flow of hydrogen protons (H^+), it must be hydrated. Therefore, this causes consequences like the presence of water inside the FC stack that must be partially removed, typically using air flows, to not cause damages to other part of the structure. Furthermore, the need for a precious catalyst to activate the electrochemical reaction with a good kinetic is critical. Usually, platinum (Pt) is used but it suffers from carbon deposit which damage the catalyst surface by reducing and deactivating the useful area. Concerning the structure of the cell, a supporting layer is placed next to catalyst layers: it helps with the diffusion and of molecules and electrons. Their working temperature is low (around 70°C), and the future of this type of fuel cell is to use Polybenzimidazole-type membranes that allows higher working temperature (130°C), the absence of fluorine, less precious catalyst, higher efficiencies, no water management and a lower quality of hydrogen. For what concern SOFC, they can achieve higher operating temperature (700-800°C) thanks to a ceramic electrolyte. Regarding its layout, the cathode is made of a Perovskite structure that is a good electron and ion conductor and is composed of rare earth material and transition metals; the anode presents the catalyst to improve electrons conduction and depending on its size (order of 10 up to $10^2 \mu m$), the SOFC single cell structure can be classified as Electrolyte Supported Cell (ESC) or Anode Supported Cell (ASC). This second configuration allows better performances, and, in the future, it is supposed to be replaced by a Metal-supported cell. A very interesting aspect of SOFC is the fuel flexibility, which allows the use of this fuel cell with different fuels (CO, H_2, CH_4). However, carbon deposit phenomena on the anode is a strong challenge to face: a solution to avoid it is represented by the triangle of equilibrium

$C - H - O$, which explain the percentage of fuel mixture to introduce in the anode thanks to the usage of oxygen carrier (CO_2, O_2, H_2O). A fascinating implementation of SOFC in hybrid system is the SOFC-GT (Gas Turbine) where the FC replaces the original combustor of the classical GT. In this case, the SOFC works in not so high pressure (≈ 6 bar) but the incrementation of it increases also the Nernst potential and the diffusion allowing, therefore, higher performances (η_{el} ≈ 75% for the hybrid configuration and the classic GT one η_{el} ≈ 30-38%). Nowadays, there are 10 plants in Japan of hybrid SOFC-GT plants made by Mitsubishi [48].

2.1 Parameters of batteries

Battery performance parameters such as C-rate, capacity, and nominal energy are critical metrics for assessing suitability in energy storage applications, enabling quantitative comparisons across technologies like lithium-ion and lead-acid batteries. These indicators not only define operational limits but also guide selection for renewable integration and electric mobility, as explored in prior chapters on storage alternatives. This chapter provides comprehensive definitions, typical values, and contextual analysis drawn from established literature.

- **Battery Capacity**: from a fundamental point of view, the capacity is simply the total amount of electrical charge stored in a battery and can be obtained using the relation:

$$Q_{tot} = I * \Delta t \ [Ah] \ \ (eq. 9)$$

In every electrochemical battery system, side reactions accompany the primary electrochemical processes, alongside other undesirable phenomena such as crystallisation and oxidation. Higher current densities intensify these issues by diverting more input energy toward irreversible processes, where a portion of the energy is lost to heat generation, side reactions, and related degradation mechanisms.

As a result, discharging a battery at very high current densities converts part of its internal capacity into these losses, meaning the measured cell output underestimates its true total capacity. Temperature further influences performance: cooling increases internal resistance and thus irreversibility, while elevated temperatures enhance measurable capacity by reducing resistance.

Accurate capacity measurement therefore requires strict control of temperature and its variations throughout the discharge process.

- **Energy Capacity**: the energy capacity of a battery represents the total watt-hours (Wh) deliverable during discharge at a specified C-rate, from full state-of-charge (100%) down to the cutoff voltage. It is calculated by multiplying the discharge power (in watts) by the discharge duration (in hours) or by multiplying the battery capacity (in Ampere-hour) by the differential in potential (in Volt), with values typically decreasing as the C-rate increases, mirroring trends observed in capacity measurements.

$$E_{tot} = Q_{tot} * \Delta V \ [J] \ \ (eq. 10)$$

- **State of Charge (SOC) [%]**: expression of the actual battery capacity as a percentage of maximum capacity. SOC is generally calculated using current integration to determine the change in battery capacity over time.
- **Depth of Discharge (DOD) [%]**: the percentage of battery capacity that has been discharged as a percentage of maximum capacity. A discharge to at least 80 % DOD is referred to as a deep discharge.
- **Terminal Voltage (V) [V]**: the voltage between the battery terminals with load applied. The terminal voltage varies with SOC and discharge/charge current.
- **Open-circuit Voltage (Voc) [V]**: the voltage between the battery terminals with no load applied. The open-circuit voltage depends on the battery SOC.
- **Nominal Voltage (Vn) [V]**: the reported or reference voltage of the battery (reported in the data sheet).
- **Cut-off Voltage (Vcut) [V]**: the minimum allowable voltage (below it the battery can break). It is this voltage that generally defines the “empty” state of the battery.
- **Cycle Life (number for a specific DOD)**: the number of discharge-charge cycles the battery can experience before it fails to meet specific performance criteria. Cycle life is estimated for specific charge and discharge conditions. The actual operating life of the battery is affected by the rate and depth of cycles and by other conditions such as temperature and humidity. The higher the DOD, the lower the cycle life.
- **Specific Energy [Wh/kg]**: the nominal battery energy per unit mass, sometimes referred to as the gravimetric energy density. Specific energy is a characteristic of the battery chemistry and packaging. Along with the energy consumption of the vehicle, it determines the battery weight required to achieve a given electric range.

- **Energy Density [Wh/m^3]**: the nominal battery energy per unit volume, sometimes referred to as the volumetric energy density. Specific energy is a characteristic of the battery chemistry and packaging. Along with the energy consumption of the vehicle, it determines the battery size required to achieve a given electric range.
- **Power Density [W/m^3]**: the maximum available power per unit volume. Specific power is a characteristic of the battery chemistry and packaging and determines the battery size required to achieve a given performance target.
- **C-rates**: in describing batteries, discharge current is often expressed as a C-rate in order to normalise against battery capacity, which is often very different between batteries. A C-rate is a measure of the rate at which a battery is discharged relative to its maximum capacity. A 1C rate means that the discharge current will discharge the entire battery in 1 hour. For a battery with a capacity of 100 Amp-hrs, this corresponds to a discharge current of 100 Amps. A 5C rate for this battery would be 500 Amps, and a C/2 rate would be 50 Amps. So, in general, C-rate can be written as:

$$C - rate = I = \frac{Q_N}{3600}\ [A]\ \ (eq.11)$$

- **State Of Health (SOH)**: measures a battery's current maximum capacity relative to its initial nominal capacity when new, expressed as a percentage.

$$SOH = \frac{Q_{tot}}{Q_N} * 100\ [\%]\ \ (eq.12)$$

Together with these definitions, it is important to highlight also some useful graphs that show the principal characteristics of a battery [46]:

  - **Spyder Plot** shows the principal characteristics of a battery, normalising it with the maximum values (scaling factors). It is helpful for a fast comparison of different technologies.

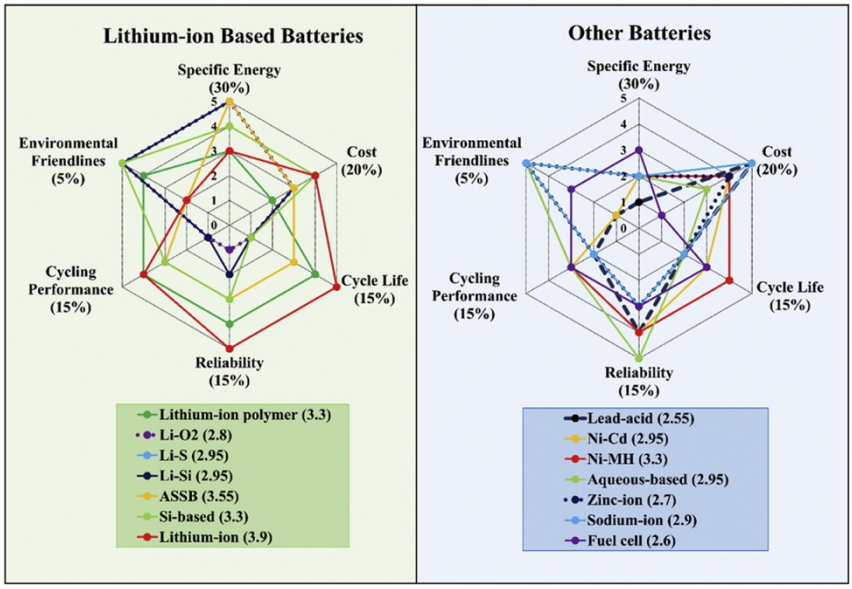

Figure 14 Spider plot shows the principal characteristic of a LIB type vs. other batteries [49].

- **Ragone Plot**: it is used for comparing the energy density of various energy-storing devices. In the plot, the values of specific energy (in Wh/kg) are plotted versus specific power (in W/kg) on a logarithmic scale. The plot is named after David V. Ragone (1930-2023). To get it experimentally (or with a simulation) the battery is discharged at different C-rates (*Figure 15*).
- **Polarisation Plot**: a polarisation curve is a plot of current density (i [A/cm2]) versus terminal potential (V [V]) for a specific cell (is more used for fuel cell) (*Figure 16*).
- **Discharge Plot**: A discharge curve is a plot of time (t [h]) versus terminal potential (V [V]) for a specific cell (*Figure 17*).

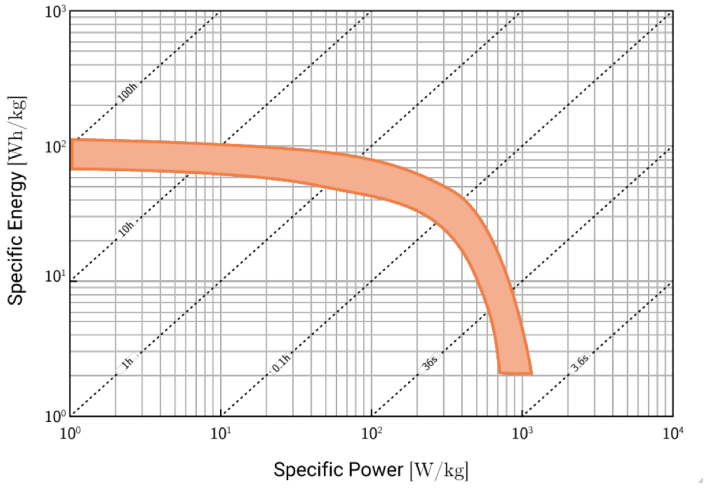

Figure 15 Example of Ragone plot [46].

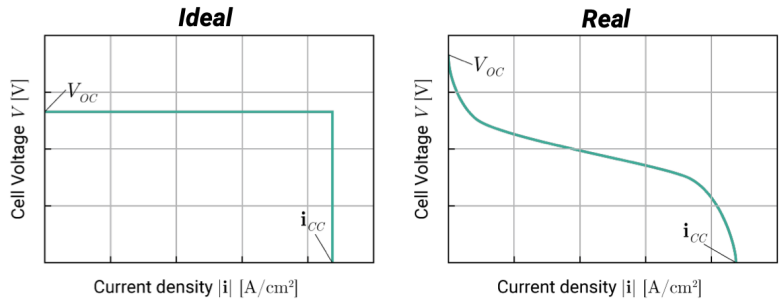

Figure 16 Example of Polarisation plot [46].

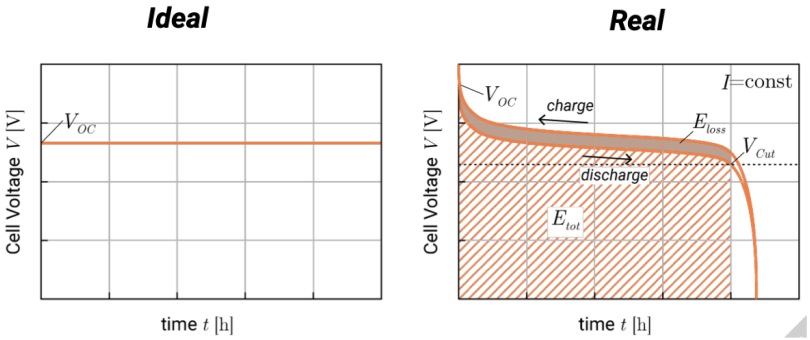

Figure 17 Example of Discharge plot [46].

2.2 Battery Degradation

Lithium-ion batteries dominate energy storage due to their high energy density and cycle-life, and they will continue to play a crucial role in enabling the transition to a sustainable and carbon-free future. Yet persistent degradation mechanisms undermine their long-term viability in applications like electric vehicles and grid storage. Central challenges include solid electrolyte interphase (SEI) instability, lithium plating leading to dendrites, thermal runaway risks from high temperatures, and resource exploitation concerns in supply chains. These issues manifest as capacity fade, impedance rise, and safety hazards, directly impacting state of health metrics discussed in prior chapters. Addressing them is essential for advancing sustainable battery technologies aligned with renewable energy transitions [50].

The degradation of lithium-ion batteries primarily manifests in both the anode and the cathode. At the anode, growth of the solid electrolyte interphase increases interfacial impedance and progressively reduces the accessible capacity; mechanical stresses induce surface cracking, while lithium plating can promote dendrite formation on the anode surface.

In contrast, cathode degradation is mainly associated with the development of surface films, mechanically induced stress and cracking, and the dissolution of transition-metal species from the active material.

2.2.1 Degradation in the anode

In the last three decades, a lot of research has been conducted to improve the anodes for rechargeable batteries. These negative electrodes are typically made of silicon, graphite, metal or different composite materials, but the majority of commercial batteries presents graphite-based anodes since carbon materials have dominated the market thanks to their high electronic/ionic conductivity, availability of raw materials, and suitable mechanical and good thermal qualities.

In the battery anode, degradation occurs due to SEI, lithium plating, cracking and exfoliation.

- SEI: is a layer that is formed on the anode surface during the initial charging. It is a phenomenon that happens because of the different potential of the electrolyte and graphite once the anode is assembled: this means that the graphite potential lies outside the thermodynamic stability window of the electrolyte and, as a result, is reduced during the first cycles, consuming Li^+ and forming surface films that directly contribute to Loss of Active Material (LAM) and Loss of Lithium Inventory (LLI). The rapid electrolyte reduction in the initial cycles produces a passivating solid electrolyte that is permeable to Li^+ but significantly less permeable to solvent and salt species, thereby suppressing further electrolyte decomposition and limiting electrode corrosion. Once it has formed, it continues to evolve during both cycling and storage and its growth rate is strongly influenced by operating conditions such as temperature, state of charge, current rate and electrolyte composition: elevated temperature and SOC enhance electrolyte reduction at the anode-electrolyte interface, resulting in thicker and more resistive SEI layers. It is an irreversible process, where the Li^+ lost cannot be recovered and it leads the battery to a reduction in capacity and efficiency with an increase of the cell impedance [51]. From a mechanistic point of view, LLI mainly arises because cyclable Li^+ ions are irreversibly consumed to sustain SEI growth, lithium plating and other parasitic reactions, so that less lithium is available to shuttle between electrodes during

subsequent cycles; by contrast, LAM is associated with the progressive electrochemical isolation or structural degradation of active electrode particles (for example due to particle cracking, loss of electrical contact or current-collector corrosion) and thus reduces the amount of active host material that can reversibly intercalate Li^+. In practice, SEI thickening can contribute simultaneously to both modes: continued electrolyte reduction and SEI formation consume Li^+ (LLI), while non-uniform SEI growth and stress can fracture or electrically disconnect graphite particles, thereby generating LAM even if the total lithium content of the cell remains unchanged. As an illustrative example, detailed degradation analyses report that, after several years of cycling, total LLI can account for roughly 15-25% of the initial capacity (largely driven by lithium isolation and SEI growth), whereas LAM of the active material may contribute on the order of 10-15%, with LAM becoming more pronounced at lower discharge rates and under conditions that promote mechanical stress and dry-out in the electrodes [52] [53] [54].

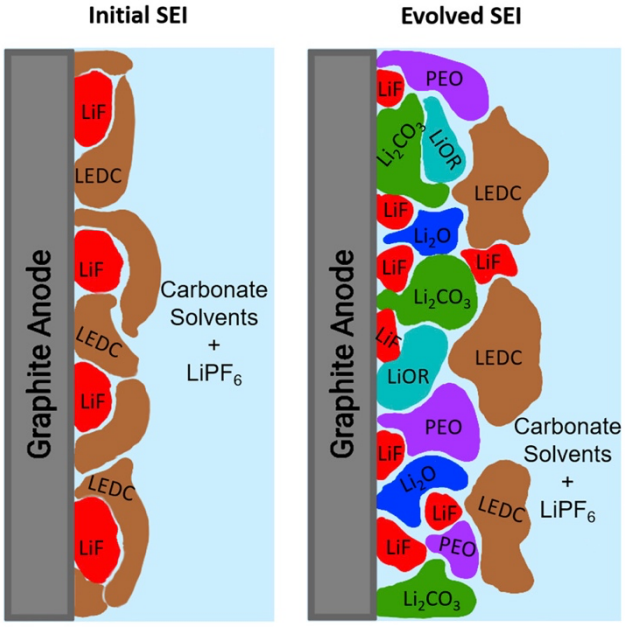

Figure 18 SEI evolution [51].

- Lithium plating: it happens during charging when lithium ions deposit on the anode surface generating metallic lithium, which is one major cause concerning battery degradation. Exposure at low temperature or high charging rates coupled with overcharging or high level of SOC intensify the effect. At low temperatures, especially during charging, the power and energy densities of lithium-ion batteries decline mainly due to three factors: insufficient charge-transfer kinetics at the

electrode-electrolyte interface; reduced solid-state diffusion of Li^+ within the active materials, and decreased ionic conductivity in the electrolyte. The lower ionic conductivity causes an increment of the internal cell resistance, but it is not the primary issue in low-temperature charging process: in fact, the lithium plating in this condition can be referred to poor Li^+ diffusion inside the electrodes [55] [56]. This issue leads to dendrite development, which can result in internal short circuits, overheating or even explosions, and increases internal resistance, capacity loss and safety risks. At low temperatures (typically below 20°C), the graphite intercalation potential shifts closer to that of metallic lithium, while lithium diffusion slows in both the anode and electrolyte. This promotes metallic lithium plating on the anode surface, while high C-rates, low temperatures, and low state of charge worsen this risk [57] [58]. On the other hand, during fast charging, the charging rate may exceed the intercalation rate, resulting into an increase of Li^+ ions transferred from cathode to anode per unit of time during charge-transfer process at high C-rate.

Lithium plating is not as immediately damaging as SEI growth, because it can be seen as a self-reinforcing process in which deposits on the anode reduce the active surface area, increasing current density in remaining accessible pores and promoting further metal plating which results in LLI and may make the cell less safe due to possible internal short circuits by allowing lithium dendrites to form [59]. Lithium plating can be estimated using the Butler–Volmer equation [60]:

$$i = i_0(\exp\left(\frac{(1-\alpha)F\eta}{RT}\right) - \exp\left(\frac{-\alpha F\eta}{RT}\right)) \ [\frac{A}{m^2}] \ (eq.13)$$

Where the i, i_0 are current density $[\frac{A}{m^2}]$; α is the charge transfer coefficient (typically 0.5 for symmetry); F is the Faraday constant equals to 96,485 $[\frac{C}{mol}]$; η is the over-potential given by a difference of potential between solid phase, the electrolytic one and the equilibrium potential of the reaction: $\eta = \phi_s - \phi_e - U_{eq}$ $(eq.14)$; RT is the product of the universal gas constant $R = 8.314\ [\frac{J}{mol\ K}]$ and T in the absolute temperature in Kelvin.

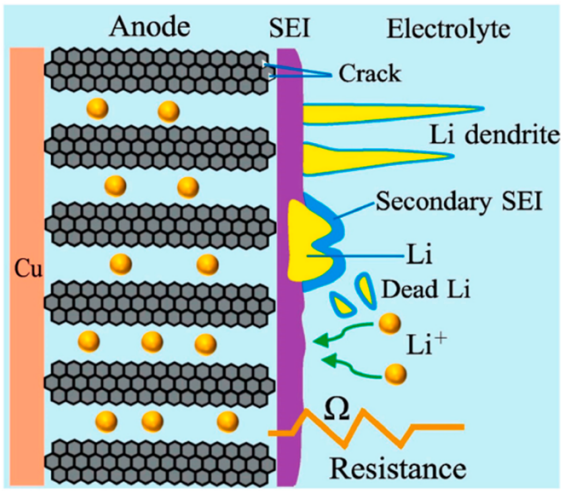

Figure 19 Degradation mechanism in anode due to Lithium plating [61].

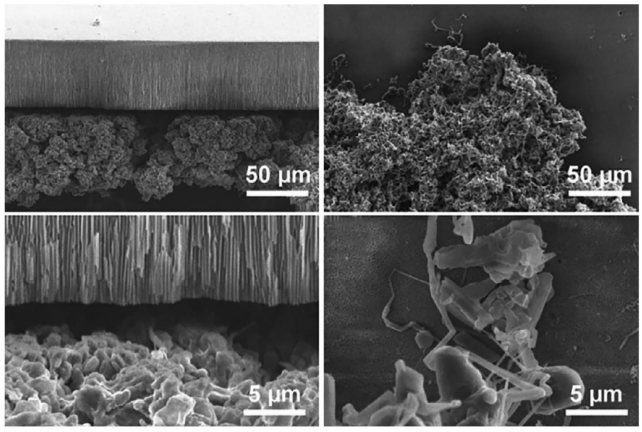

Figure 20 Lithium dendrites [62].

- Stress: mechanical stress, like volume changes, and thermal expansion/contraction at the anode is one of the principal causes of battery degradation, in which the anode experiences physical damage from the stress, such as deformation or cracking, which would damage its structural integrity and reduce its ability to store and release lithium ions during charge-discharge cycles. These damages may lead to an increase of the internal resistance with a consequent reduction of its overall performance and efficiency. Moreover, this kind of stress could allow the penetration of the electrolyte into the anode material and start chemical reactions that eventually weaken the anode structure and reduce battery capacity [63]. Additionally, internal short circuits caused by stress-induced dendritic growth, a process in which microscopic lithium metal fibres extend from the anode surface, can enter the separator, leading to serious safety risks such as thermal runaway, overheating, or explosions. To monitor these mechanical stresses and volume changes in real time, strain sensors, such as strain

gauges placed on the battery casing or explosion-proof valve, offer an effective early warning system for thermal runaway. These sensors detect infinitesimal deformations (e.g., under 10 μm) associated with gas generation and swelling, providing alerts up to 600-906 seconds earlier than temperature-based methods, enabling timely intervention to prevent propagation [64] [65]. During lithium-ion intercalation into the anode, particles undergo a phase transition which may cause sudden volume changes, and these shifts alter molecular orientation, exhibiting unique geometrical and electrical properties that generate mechanical stress. These forces may lead to loss of contact with the electrode layer, cracking of the surface layer and anode structure. Additionally, volume expansion of the active material can reduce electrode porosity, obstructing electrolyte access to the electrode bulk [66] [67].

- Exfoliation: it refers to the separation of graphite layers in lithium-ion battery anode, primarily due to unwanted co-intercalation of solvent molecules alongside lithium ions into the graphite structure. During charging, solvated Li^+ ions from the electrolyte can enter the layered graphite structure instead of losing their solvation first. Solvents like Propylene Carbonate (PC) co-intercalate more easily than Ethylene Carbonate (EC), weakening interlayer bonds and causing graphite sheets to peel apart. This process competes with proper Li^+ intercalation, leading to structural damage visible via techniques like Raman spectroscopy[9]. Exfoliation occurs mainly with incompatible electrolytes, such as PC-based ones, where higher solvation energy allows solvent co-insertion. Fast charging, low temperatures, or repeated cycling worsen it by promoting incomplete SEI formation or increased solvent interaction; on the contrary, elevated temperatures can sometimes suppress it by altering decomposition kinetics resulting in capacity fade, gas generation, continuous SEI growth, and eventual cell failure, as fresh graphite surfaces react further with electrolyte. In commercial cells, this limits fast-charging graphite anodes, reducing cycle life and safety [68][69].

[9] Raman spectroscopy is a non-destructive, inelastic light-scattering technique used for chemical identification, structural characterization, and molecular analysis. Ibsen Photonics. (2025, August 13). *What is Raman spectroscopy – Uses and applications.*

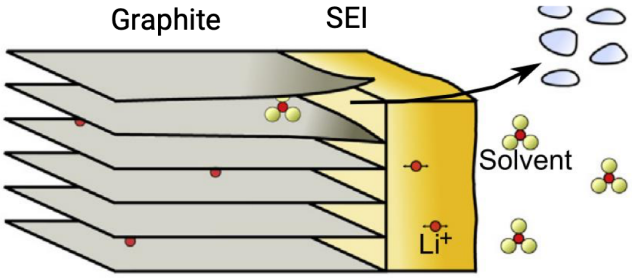

Figure 21 Anode Exfoliation of a Li-ion battery [70].

2.2.2 Degradation in the cathode

Degradation in the cathode of lithium-ion battery is quite different from that in the anode: in this case, it involves mechanisms such as transition metal dissolution, formation of surface layer film, stress, and particle cracking. These processes contribute to capacity loss, reduced cycling stability, decreased energy density, and decreased battery performance over time.

- Film on cathode surface layer: commonly called the Cathode Electrolyte Interlayer (CEI), it is a thin film which develops on the cathode surface due to electrolyte oxidation and salt deposition, similar to what happen at the anode (SEI). Research conducted on $LiMn_2O_4$ structural and compositional changes by Roy et al. (2023) has shown that oxygen deficiency near the pure $LiMn_2O_4$ surface correlates with lithium deficiency and a mean Mn oxidation state lower than expected from the classical intercalation mechanism. This non-stoichiometry creates a thin surface layer with approximate $LiMn_2O_4$ composition that gradually varies to a depth of about 15 nm [71]. Following Li removal, Mn^{3+} ions oxidise into smaller Mn^{4+} ions, reducing lattice volume within the film and generating significant strain in the surface layer during initial charging. This highly strained surface layer destabilises and reconstructs, forming Mn_3O_4 at 2-3 nm depth with additional oxygen loss, followed by Mn^{2+} dissolution and/or spallation[10] of the strained surface film during the first cycle sharply reduce specific capacity. Unlike the SEI layer, the cathode surface exhibits poor Li^+ conductivity, increasing impedance [72].
- Stress: like the anode, the cathode undergoes phase transitions during Li-ion intercalation/deintercalation that cause loss of active material and loss of composite electrode (CL), and, depending on the chemistry, different amounts of volume

[10] Spallation is the process where fragments of material break off from a solid surface due to stress, impact, or strain exceeding the material's tensile strength. Wikipedia contributors. (2024). *Spallation*. Wikipedia.

change. For instance, LFP cells only have a two-phase regime with $FePO_4$ and $LiFePO_4$ [73].

- Dissolution of Transition Metals: transition metals oxides, like those containing cobalt, manganese or nickel, are commonly used as cathode materials in lithium-ion battery. During repeated charge-discharge cycling, especially under high temperatures or extreme conditions, these transition metal ions dissolve into the electrolyte via side reactions at the cathode interface. Once they have been dissolved, they migrate to the anode where they deposit as metallic species or dendrites [74][75]. The dissolution of transition metal during charging is inevitable but can be reduced by using electrolyte with high purity level, cathode dopants and protective coatings to limit direct cathode-electrolyte contact [76].

2.2.3 Other types of degradation

Cycling, or each charge-discharge cycle throughout a battery's lifespan, causes natural degradation as its chemical and physical structure is altered with every cycle, breaking down the electrode material and forming undesirable compounds that lower the battery performance and capacity [77]. Moreover, temperature is a degrading element: high temperatures accelerate chemical processes leading to a faster deterioration of both electrode and electrolyte materials. Similarly, low temperatures play a crucial role by reducing energy efficiency and capacity, and may cause safety risks such as thermal runaway.

- Cycling Degradation: it describes the gradual performance decline that batteries experience through repeated charge-discharge cycles over their operational lifespan [78]. Lithium-ion battery cycling deterioration arises from a combination of chemical and physical processes occurring during repeated charge-discharge cycles, with mechanical stress on electrode materials (particularly the anode) serving as a primary factor due to significant volume changes. This degradation is driven by the combined effects of mechanical, electrochemical, and thermal stressors, ultimately impacting the battery's capacity, energy retention, and overall performance throughout its operational life. Various models exist to estimate this cycling ageing process [79] [80].

  Cycling degradation can be estimated from the following equation:

$$L_{Cyc} = \Sigma_i^N \, n_i f_c \left(\sigma_i, \delta_i, T_{c,i}\right) \quad (eq.15)$$

Where: N is the number of cycles, n_i mentioned that i is a full cycle or half, δ_i is the depth of discharge, σ_i is the average SOC of the cycle and $T_{c,i}$ is the average cell temperature [81].

- Electrolyte breakdown: in lithium-ion batteries it involves the chemical deterioration of the electrolyte triggered by repeated cycling, high temperatures, or overcharging, leading to undesirable side products that increase internal resistance, accelerate capacity fade, and degrade overall performance. This complex process compromises the electrolyte's critical role in facilitating ion transport between electrodes through various chemical and electrochemical reactions, including the continuous growth of the solid electrolyte interphase during charge-discharge cycles (which, despite being essential for normal operation, impedes ion conduction over time) and oxidative decomposition at high voltages that generates heat, gases, and reactive species, further worsening degradation, especially under overcharge or elevated temperature conditions [82] [83].
- Temperature variations affect electrochemical processes within the battery, compromising its overall health. High temperatures significantly impact lithium-ion battery performance and safety by accelerating chemical processes, driven by either external sources or internal heat from charge-discharge cycling, that promote electrolyte decomposition, intensified electrode-electrolyte interface reactions, and amplified thermal runaway risk, while also enhancing solid electrolyte interphase formation and growth on electrode surfaces (essential for operation yet excessive growth raises internal resistance and impedes ion transport) and elevating dendrite formation potential, particularly in lithium metal anodes [84] [85]. In contrast, cold temperatures impact on internal resistance and ion mobility. These temperatures reduce lithium-ion mobility within the battery, slowing electrochemical processes; at 0°C or below, degradation accelerates, while, according to Naga Subramanian, Panasonic 18650 LIBs (exhibiting ~800 W/L power density and 100 Wh/L energy density at 25°C) lose 98.75% and 95% of these values at −40°C (dropping to <10 W/L and ~5 Wh/L), and experience nearly 23% state of charge reduction when temperatures fall from 25°C to −15°C, where SOC represents the ratio of remaining to total available capacity [86] [87]. Charge-transfer resistance, another key factor in lithium-ion battery performance degradation at low temperatures, increases

significantly, with $LiFePO_4$– based cathodes showing a three-fold rise at −20°C compared to ambient conditions, where slowed ion diffusion (particularly evident during discharge) reduces capacity and power output while elevated internal resistance further impedes ion transport [84] [88] [89].

2.3 Battery Safety

Thermal management of batteries under operational conditions represents the main safety challenge, as the heat they generate cannot be entirely removed, especially during hot days or in large battery packs. In particular, rising temperatures trigger parasitic reactions that can lead to thermal runaway, where heat generation becomes uncontrollable. Additionally, mechanical stresses such as compression or shell-casing damage, electrical issues from overcharge/over-discharge or short circuits, and thermal abuse involving thermal shock or local heating, all of which can occur during accidents, further accelerate the thermal runaway process. For these reasons, understanding LIB performance under unsafe conditions is critical for developing safer battery cells [90] [91].

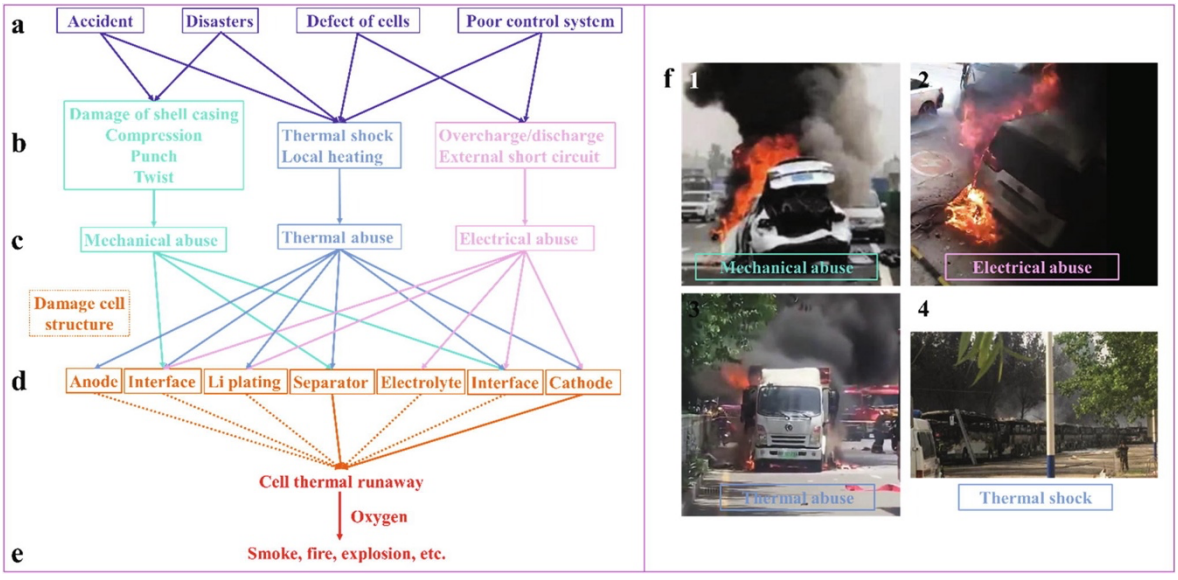

Figure 22 Cause–effect diagram of battery accidents and thermal runaway initiation [92].

As *Figure 22* shows, battery accidents or defects of cells (a) lead to electrical, thermal abuse and mechanical one (b, c) which can activate secondary reactions inside the battery materials (d). The main causes of thermal runaway are the separator collapse and the release of oxygen by the cathode leading to the generation of smoke and to explosion or fires with the interaction of oxygen in air. On the right side of the image, some real events are

illustrated, where four different abuses are presented: a collision can cause the compression of the battery, and the area with the greatest stress may be damaged, resulting in an internal short-circuit and causing thermal runway. An intense charging period results in uncontrollable thermal management, with no possibility of dissipating heat before thermal runaway occurs. Similarly, intense usage coupled with high ambient temperatures increases the difficulty of dissipating the generated heat.

2.3.1 Thermal runaway

Thermal runaway is the most deleterious LIB safety issue. The origin of this phenomenon can be extrapolated from *Figure 22* in addition with side reactions occurring at the cathode, anode and electrolyte as well as reactions evolving on the surface of these materials as already illustrated, all activated by mechanical, thermal and electrical abuse.

It is possible to define five types of causes for this incident: the first one is uncontrollable internal heat generation, which causes oxygen release from the cathode structure resulting in numerous side reactions [93]. Next, due to inducted thermal shrinkage or mechanical damage, the separator defects, in the second type, generate short-circuit with consequently rapid discharge of the stored energy, together with non-desirable chemical reactions and the release of high amount of heat [94]. The third type is represented by electrical abuse, specifically electrolyte decomposition, particularly at high state of charge, which takes place at the cathode interface and causes heat accumulation, which in turn promotes oxygen release from the cathode and damages the separator [95]. The fourth type involves electrochemical side reactions triggered by localised thermal abuse: when heat generated during normal LIB operation cannot dissipate quickly enough, the separator in that area shrinks or ruptures [96]. In conclusion, the fifth type arises from mechanical battery damage, which induces short circuits and/or air ingress into the battery. Among these five categories, the primary causes of battery safety accidents are short-circuiting from separator damage, electrical abuse, and mechanical abuse [97].

2.3.2 Safety issues caused by Mechanical Abuse

Due to the high energy density of LIBs, damage caused by external events such as collisions releases a significant amount of energy, resulting in higher safety risks. In addition, as the number of BEVs on the roads (containing LIBs) increases, safety concerns regarding battery behaviour during potential vehicle collisions are becoming more

significant. A moving car's battery experiences localised forces that, in extreme cases, can cause damage to the LIBs [98]. The structure of each cell is composed of an external shell made of aluminium or iron, and a softer part consisting of cathode, anode and electrolyte.

Under an event like collision, this weaker part is the one that must be protected to avoid thermal runaway; therefore, the outer shell needs to withstand mechanical forces and not break, ensuring the safety of the internal part under deformation condition [98]. For this reason, the development of a resistant shell casing, together with new design, configuration and material, is vital to understand the overall LIBs mechanical behaviour as it is the most vulnerable part during safety accidents [100]. Even when the shell casing is simply deformed, LIB internal components can suffer severe damage, as inflexible metallic current collectors and separators fracture, enabling direct electrode contact. The heat generated by the high energy density LIB following a localised short circuit can then trigger additional internal shorts in the surrounding region, resulting in overall battery thermal runaway [101].

2.3.3 Safety issues caused by Electrical Abuse

Electrical abuse is strictly connected to overcharge or over-discharge state. If there is no control of the voltage by the monitoring system, there will be the risk of overcharging where excess energy will be stored inside the cell. To avoid this problem, batteries are typically charged up to a well-defined SOC level below their maximum, conversely, if a battery already has a high SOC before charging, it will be overcharged. The first cause of this event is the electrolyte decomposition at the cathode surface with a significant increase in battery temperature. Afterwards, excessive Li^+ deintercalation from the cathode occurs, and its material becomes unstable and starts to release oxygen, while lithium dendrites start to form on anode surface. These side reactions comport the generation of heat and gas that lead to safety accident like overheating and rupture [102][103]. The charging rate is typically the most significant factor influencing overcharge, as the overcharging current density controls the rate of heat generation from battery reactions: higher currents produce more heat per unit time, thereby elevating the risk of uncontrollable LIB behaviour.

Similarly to what happens during overcharging, problems also arise when the battery is forced to over-discharge: over-discharge increases the extraction of Li^+ from the anode, which change the graphite structure and destroy the SEI [104].

An external short circuit occurs when a cathode and anode of the same cell connect directly through a conductor, causing both electron and ion transfer at the same location

rather than decoupled transport, which enables rapid Li^+migration and battery discharge. During safety accidents, LIB cathodes and anodes may indeed contact each other, releasing heat relatively equally and quickly [105].

Overcharge represents the most dangerous form of electrical abuse and one of the most frequent causes of LIB safety accidents. The other two types (over-discharge and external short-circuiting) are relatively benign, failing to trigger instant, rapidly developing failures, though they can still degrade a LIB's state of health.

2.3.4 Safety issues caused by Thermal Abuse

When a battery undergoes a thermal abuse, it experiences a thermal shock. When it catches fire, this is usually due to overcharging or to a nearby fire: this happens as a result of combustible airborne materials (such as highly flammable pollen grains, seeds, flowers, or leaves) near a malfunctioning battery may ignite when in proximity or direct contact with the hot surface or emitted sparks, potentially setting surrounding materials on fire. Localised high temperature areas within a battery typically arise from its design, where poor LIB design creates high impedance at metal contacts or uneven heat dissipation, as evidenced by non-uniform temperature distribution during thermal shock testing, simulated by placing the battery in a 155°C oven for 1,200 seconds [106]. Since the elevated surrounding temperature triggers exothermic reactions, the internal temperature distribution became more closely tied to heat generated by these reactions than to the external thermal energy input, with the highest temperatures appearing at the centre and non-uniformity growing more pronounced over time. After 3,600 seconds under these conditions, thermal runaway occurred in the cell.

In theory, battery cycling cannot cause safety accidents because heat generated during normal anodic and cathodic reactions proves insufficient for sharp temperature increases; however, in reality, the electrode heat release rate often exceeds the cooling rate, with LIB heat dissipation depending on external surface area and geometry while radiation helps alleviate some accumulated heat. Consequently, if this residual heat continues building rather than dissipating, exothermic side reactions emerge and intensify thermal stress [107].

2.3.5 Safety Improvements

The intrinsic safety of a battery refers to its essential safety characteristics, which directly determine the probability of battery-related accidents. Various factors influence this intrinsic safety, including cell materials (such as LFP), design parameters (like separator

thickness and the negative-to-positive electrode capacity ratio, or N/P ratio), manufacturing quality (including impurity control and fabrication precision), as well as overall battery consistency and reliability [108] [109].
The following strategies can enhance a battery's intrinsic safety:

- Improving the manufacturing quality level: good manufacturing and production are fundamental for battery safety: over the past decades, rapid development has occurred in battery production technology and equipment. Currently, major battery manufacturers maintain high product qualification rates. Next-generation high energy density batteries demand even stricter manufacturing requirements, making intelligent manufacturing and Industry 4.0 the primary focus for leading producers.
- Improving stability of battery materials: even if a high level of manufacturing quality is achieved, it is still challenging to develop LIBs with both high energy density and high safety. For high energy density batteries, key material and cell-level solutions include the optimisation of surface coating, doping, composition, and structural design to enhance cathode material stability at high temperatures, where recent cathode surface coatings with high ionic conductivity solid electrolytes have gained attention for addressing intrinsic oxygen release in oxide cathodes. Then, employing non-flammable solvents and flame-retardant additives to boost electrolyte thermal stability and mitigate thermal runaway scale. The control of the formation process and designing artificial solid electrolyte interphases to improve SEI thermal stability and battery durability at elevated temperatures. Another strategy is developing inherently safer new systems such as solid-state batteries (SSBs) and aqueous batteries, although their industrial application will require years or even decades of development [110].

Other improvements concern the insulation of the battery, where the core idea is to reduce the impact of battery thermal runaway by preventing heat from a single cell from propagating and causing thermal runaway of the entire battery, which can lead to explosions. Specific strategies at the system level include using heat insulation materials between cells, designing cellular structures, and implementing modular heat insulation, with the ultimate goal of preventing thermal runaway in a single cell from propagating through the battery system and concerning EVs causing fire. Working both on heat dissipation and on heat preservation/preheating also represents an intriguing solution: the first ensures that the

temperature of the battery does not exceed an upper limit, represented by the nominal operating temperature. Therefore, the heat generated must be immediately dissipated through the use of forced air cooling or water cooling instead of natural air flow cooling. The second one, instead, needs preheating to work properly when placed in low-temperature conditions to ensure that the battery is at a temperature above the critical one. In this field, battery self-heating, phase-change heating, and heat pump heating, are being developed [111] [112].

3. Electric Vehicles

Battery electric, hybrid and conventional internal combustion engine (ICE) vehicles are primarily distinguished by how propulsion is partitioned between electric machines and the combustion engine, and by how the battery system is dimensioned, integrated, and managed in the vehicle energy architecture. As reported in the standard IEC 61851 (Electric vehicle conductive charging system), Part 1 (General requirements), the definition of an Electric Vehicle is the following: “any vehicle propelled by an electric motor drawing current from a rechargeable storage battery or from other portable storage devices (rechargeable, using energy from a source off the vehicle such as a residential or public electric service), which is manufactured primarily for use on public streets, roads or highways” [113].

3.1 Hybrid Electric Vehicles

A hybrid electric vehicle integrates multiple propulsion technologies, combining at least two distinct energy and power sources to optimise efficiency, performance and emissions. Typically, this includes an internal combustion engine as the primary power source alongside one or more electric motors powered by rechargeable batteries, but advanced configurations can incorporate alternatives like fuel cells or ultracapacitors [114]. A first categorisation can be applied in terms of hybrid drive: it is possible to distinguish micro hybrids, in which the electric components are only used for the start/stop function; mild hybrids, which are similar to the previous ones but where the electric motor supports the combustion engine, although it is not possible to drive exclusively with electricity; and full hybrids (HEVs), in which, in addition to the mild-hybrid functionality, pure electric drive is also possible.
Some key components are:

- Battery pack: it stores electrical energy for the motor and can be recharged via the ICE or with regenerative braking.
- Electric motor(s): it provides torque for acceleration, low-speed driving or electric-only operation, and is often paired with power electronics like inverters for energy management.
- ICE: smaller than in conventional vehicles. It charges the battery, powers the wheels directly (in parallel hybrids), or drives a generator (in series hybrids).

- Regenerative braking: converts kinetic energy from deceleration into stored electricity, improving efficiency by up to 20-30% in urban driving [115].

A second classification is based on drivetrain architecture: series-type vehicles feature a large battery pack, a compact ICE, and a powerful electric motor, requiring sophisticated control algorithms to maximise driveline efficiency while minimising energy losses.

In this series hybrid configuration, the ICE has no direct mechanical connection to the gearbox, enabling it to operate continuously at its optimal efficiency point (e.g., peak torque and minimal fuel use). However, the major drawback is the multiple energy conversion stages (ICE to generator, electricity to battery/motor, then to wheels) which introduce losses (typically 20-30% overall) and elevate costs due to the pricier high-capacity battery and associated components. In a parallel hybrid configuration both ICE and motor directly drive the wheels, often simultaneously: in this case, the ICE serves as the primary driveline source, while the electric motor provides supplemental traction power through optimised control strategies that enhance overall fuel efficiency. This setup offers key advantages: it requires only a small battery pack (reducing costs compared to series hybrids) and recharges the battery via regenerative braking or during propulsion when the ICE generates excess power. Power-split/series-parallel hybrids use a planetary gearset to blend power variably [116] [117] [118] [119].

Effective energy management strategies and optimisation in HEVs enable extended driving range, lower emissions, and reduced fuel consumption. A key advantage is that if the primary fuel tank (gasoline or diesel) runs empty during operation, the secondary electric power source (typically the battery and motor) serves as a reliable backup, allowing the vehicle to continue driving for its full electric-only range [120].

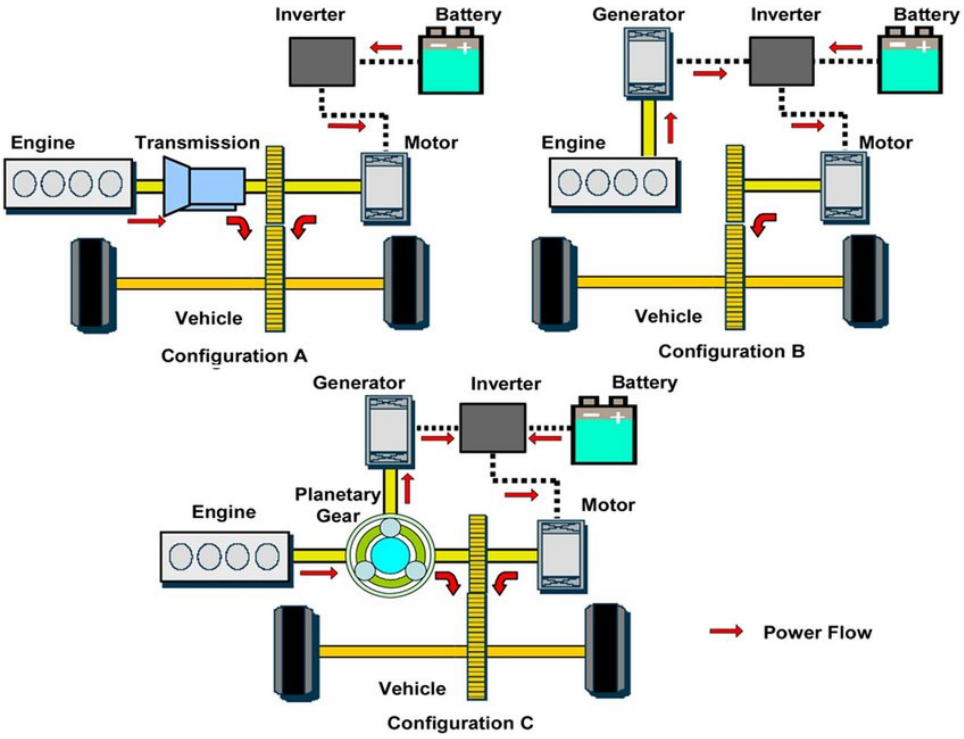

Figure 23 Hybrid vehicle configurations: (A) parallel; (B) series; and (C) power-split (parallel/series) [121].

3.2 Plug-in Hybrid Electric Vehicles

Plug-in hybrid vehicles can run on both gasoline and battery power. These batteries can be charged at public charging stations, at home via a standard electrical outlet or through regenerative braking. They produce no exhaust emissions when operating on battery power: however, emissions occur indirectly during electricity generation at power plants. PHEVs primarily rely on electricity for short weekly trips, switching to gasoline for longer journeys once the battery is discharged [122] [123]. PHEVs provide a solid driving range, yet they come with notable drawbacks, including a higher upfront cost compared to BEVs and reduced eco-friendliness due to emissions generated during electricity production at power plants. For these reasons, BEVs are steadily gaining greater popularity over PHEVs. To address these challenges, researchers are concentrating on developing more efficient batteries while exploring optimisations in packaging, thermal management, testing protocols, range extension, charging times, size, and weight to enhance overall performance [124].

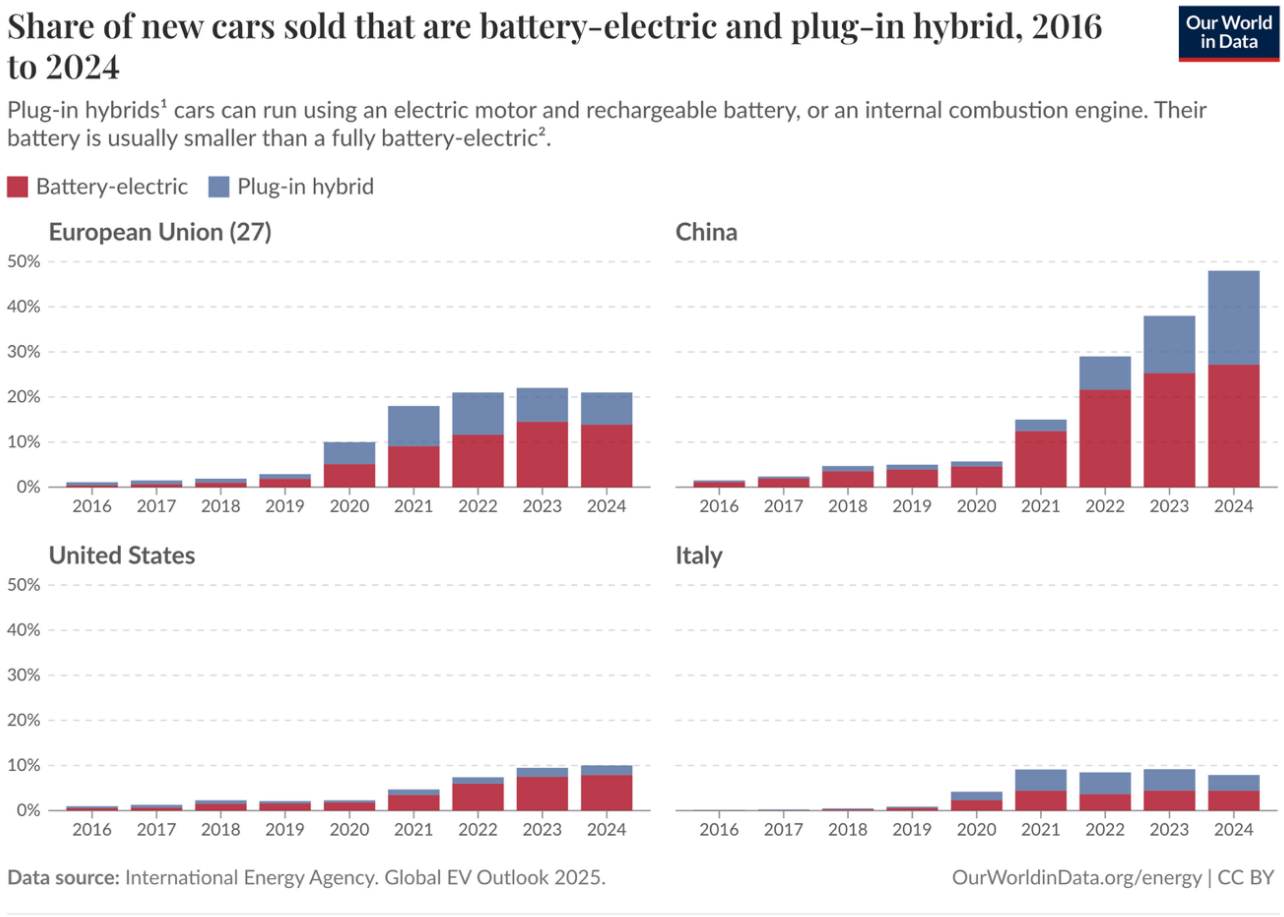

1. **Plug-in hybrid** Cars or other vehicles that have a rechargeable battery and electric motor, and an internal combustion engine. The battery in plug-in hybrids is smaller and has a shorter range than battery-electric cars, so over longer distances, the car starts running on gasoline once the battery has run out.

2. **Fully battery-electric** Cars or other vehicles that are powered entirely by an electric motor and battery, instead of an internal combustion engine.

Figure 24 Share of new cars sold BEV and PHEV, 2016-2024 [125].

3.3 Battery Electric Vehicles

In BEVs, all propulsion electricity comes solely from the onboard battery, eliminating any need for a fuel tank and thus earning them the designation of "pure electric vehicles." These vehicles feature a large rechargeable battery that emits no harmful toxic gases into the environment during operation; however, consumers often express concerns that significant pollution arises indirectly from electricity generation, battery manufacturing processes, and the eventual disposal of discarded batteries. The battery is recharged from grid power or other external energy sources via a dedicated charging plug, with typical charging times averaging 6-8 hours using slow chargers or 20-40 minutes with fast chargers, a duration that clearly contrasts with the rapid refuelling times of traditional ICE vehicles [126] [127] [128]. The performance of BEVs relies entirely on battery capacity and the effectiveness of their

thermal management systems, where battery temperature plays a crucial role in determining both performance and lifespan. In these vehicles, electrical energy is efficiently converted into mechanical energy with minimal losses, making BEVs particularly suitable for short-distance travel and stop-and-go conditions, with ranges typically spanning 100 to 400 km, depending on the installed battery type. Charging times vary according to battery capacity, the chosen charging method, and whether series or parallel connections are employed, while efforts to extend driving range and overall capabilities often lead researchers towards advanced variants such as upgraded HEVs, PHEVs, and related technologies [129].

3.4 Fuel Cell Electric Vehicles

The driveline architecture of fuel cell electric vehicles (FCEVs) closely resembles that of BEVs, except that a fuel cell replaces the battery and utilises hydrogen as the transport fuel, functioning as an electricity generator to power the electric motor for traction. Compared to traditional internal combustion engines, fuel cells offer greater efficiency and improved fuel economy, with the proton exchange membrane fuel cell being the most widely adopted due to its zero emissions, quiet operation, high power density, and flexible operating range [130] [131]. In FCEVs, tank-to-wheel efficiency exceeds 48%, far surpassing the 25%-35% range typical of ICE vehicles, although the primary drawbacks remain the complex hydrogen storage technology and the high costs associated with setup [132] [133] [134].

As evident from *Table 5* each electric vehicle type presents distinct advantages and challenges suited to different use cases and user requirements. BEVs excel in short-distance urban environments with zero direct emissions, while HEVs and PHEVs offer extended range through fossil fuel backup. FCEVs provide the efficiency of electric propulsion with quick hydrogen refuelling, though infrastructure remains limited. The choice amongst these technologies depends on driving patterns, environmental priorities, budget considerations, and available charging or refuelling infrastructure. As battery technology advances and infrastructure expands, the electric vehicle market continues shifting towards increased electrification, with BEVs and FCEVs representing the long-term trajectory towards zero-emission transportation.

Feature	BEV	HEV	PHEV	FCEV
Traction Power	Electrical motor	Electrical motor + ICE	Electrical motor + ICE	Electrical motor
Energy System	Battery + UC	Battery + ICE + UC	Battery + ICE + UC	FC + Battery + UC
Energy Source	Charging power station	Fuel pump + Gasoline	Charging power station + gasoline	Hydrogen fuel
Advantages	Zero emissions; Independence from fossil fuels	Lower emissions; Long-distance capability	Lower emissions; Long-distance capability; Electric-only mode for short trips	Zero emissions; High efficiency; Quick refuelling
Disadvantages	High initial cost; Battery replacement costs; Limited range; Long charging time (6-8 hours slow, 20-40 minutes fast)	Dependence on fossil fuels; Higher complexity; Limited electric-only range	Dependence on fossil fuels; Higher cost than BEVs; Indirect emissions from electricity generation	Hydrogen fuel storage complexity; High cost of fuel cell technology; Limited hydrogen infrastructure

Table 5 Comparison of different electrified powertrain architectures (BEV, HEV, PHEV and FCEV), highlighting their traction sources, energy systems and refuelling/charging needs, along with key advantages and limitations for practical use.

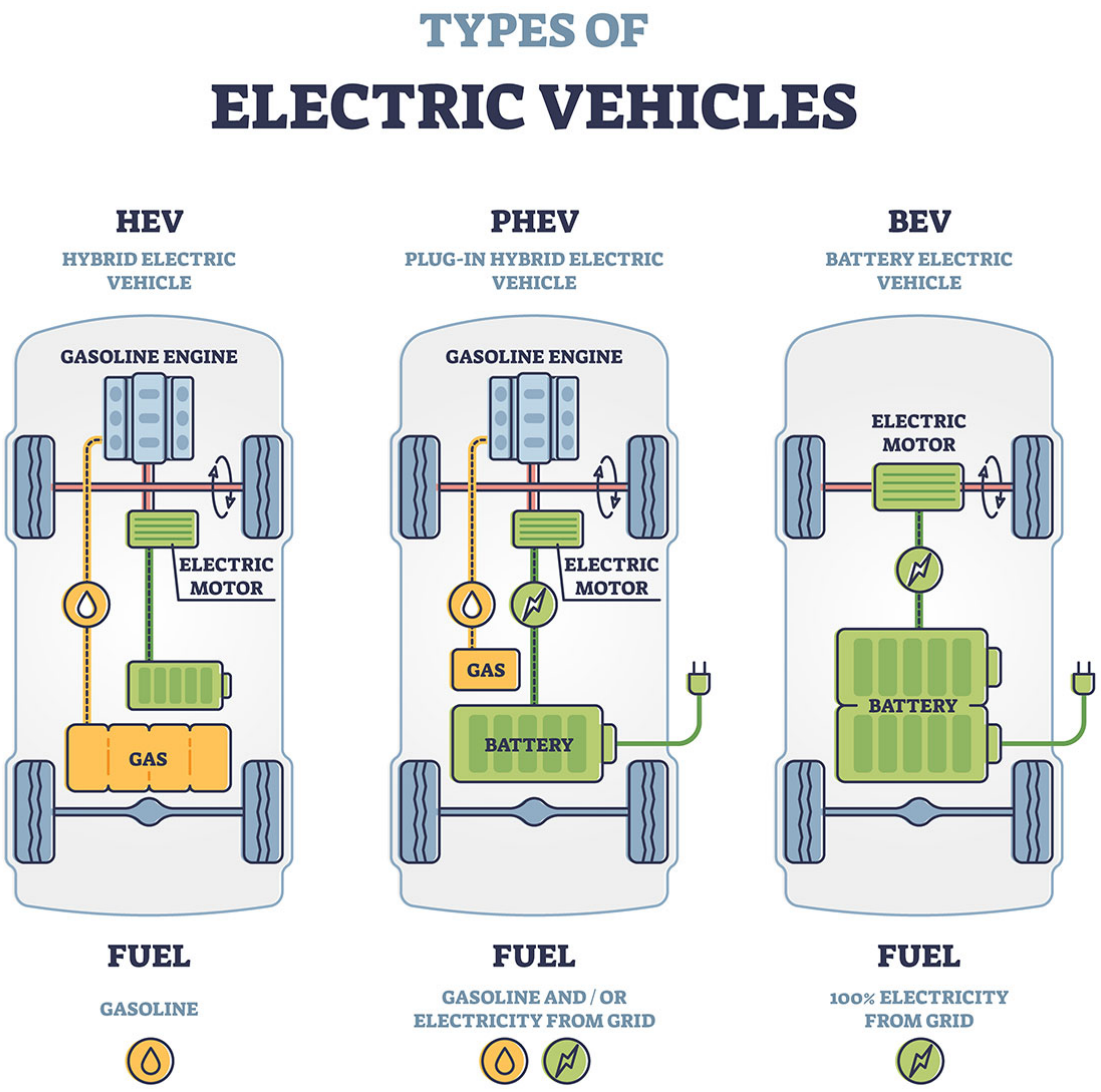

Figure 25 Diagram comparing hybrid, plug-in hybrid and battery electric vehicles [135].

3.5 Regulatory framework for BEVs

Standards and legislation for battery electric vehicle batteries vary across Europe, the US, and China, primarily governed by UNECE Regulation 100 (adopted in the EU), the proposed FMVSS No. 305a (US), and GB 38031-2025 (China). These focus on safety parameters like operating temperatures, voltages, thermal runaway prevention via shock/impact resistance, though physical dimensions are less standardised and often left to manufacturers [136] [137] [138]. UNECE R100 (EU) requires thermal shock tests from −40°C to 60°C with rapid cycling (30 minutes transitions, 4-6 hours holds, 5-10 cycles), requiring no leakage, fire, or explosion post-test, while insulation resistance must exceed

100 Ω/V DC or 500 Ω/V AC. US FMVSS 305a proposes protections for over-temperature and low-temperature operations, and for thermal propagation from single-cell runaway, with post-crash voltage isolation of ≥100 Ω/V DC. China's GB 38031-2025 imposes mechanical impact, collision, and crush tests (no fire/explosion, insulation ≥100 Ω/V DC or 500 Ω/V AC post-test), plus thermal stability and shock without leakage or cracks [139] [140] [141]. EU and US standards for EV battery safety share goals like electrical isolation and mechanical integrity but differ in testing scope, thermal runaway handling, and crash simulations. R100 emphasises comprehensive abuse tests at the battery level, while FMVSS 305a prioritises post-crash vehicle performance with documentation-based mitigations [142]. Regarding thermal runaway approach, R100 requires physical tests to induce and contain thermal runaway propagation across cells, with no fire/explosion allowed. On the other hand, US FMVSS 305a adopts a documentation approach for thermal propagation risks from single-cell runaway, plus emergency response info, without mandatory physical propagation tests [143] [144].

Parameter	EU (UNECE R100)	US (FMVSS 305a)	China (GB 38031-2025)
Operating Temperatures	-40°C to 60°C (shock/cycling)	High/low-temperature protections (not defined)	Thermal shock/stability (not specified)
Voltages/Insulation	>60 VDC/>30 VAC; ≥100 Ω/V DC, 500 Ω/V AC	≥100 Ω/V DC post-crash	≥100 Ω/V DC, 500 Ω/V AC post-test
Thermal Runaway/Impacts	Thermal propagation warning (5 min advance); vibration/shock	Thermal propagation mitigation; mechanical shock	Impact/collision/crush; no fire/explosion

Table 6 Summary of key battery safety requirements in EU, US and Chinese regulations, comparing permitted operating temperatures, voltage and insulation limits, and provisions related to thermal runaway and mechanical impacts.

European standards for BEV energy efficiency centre on the Worldwide Harmonised Light Vehicles Test Procedure (WLTP), required by EU Regulation (EU) 2019/631 and updated in (EU) 2023/443, which measures electric energy consumption in Wh/km and

range in kilometres (km). This replaces the outdated NEDC[11] cycle for more realistic lab-based assessments, supporting CO2 fleet targets that incentivise BEV uptake (e.g., 95 g CO2/km average in 2021, tightening post-2025) [145] [146]. WLTP simulates real-world driving over 23-30 minutes across low/high speeds, with higher accelerations and dynamic phases than NEDC, resulting in 10-20% higher consumption figures. For BEVs, it calculates usable battery energy consumption (city/combined), range, and factors like auxiliary loads (e.g., AC, heating) [147] [148]. Regulation (EU) 2019/631 sets manufacturer-specific CO2 targets, where BEVs count as zero-emission but must declare WLTP efficiency for labelling and compliance. No direct Wh/km efficiency thresholds exist yet, but proposals discuss BEV-specific targets; WLTP values inform consumer labels and fleet averaging[12] [149] [150].

[11] The New European Driving Cycle (NEDC) is a standardised test procedure used to measure vehicle emissions and fuel economy. It simulates driving conditions on a dynamometer to assess performance under controlled lab settings. NEDC consists of four repeated urban driving cycles (ECE-15 or UDC) followed by one extra-urban cycle (EUDC). The urban phase lasts 780 seconds over about 4 km at an average 18.35 km/h, while the full cycle totals 1180 seconds across 11 km at 33.35 km/h average speed [151].

[12] Fleet averaging calculates a manufacturer's average emissions or efficiency across all vehicles sold in a model year, based on production volumes [152].

4. SOH Analysis on BEVs

Battery electric vehicles have become one of the most promising solutions to decarbonise the transport sector, thanks to their high drivetrain efficiency and the possibility of using low-carbon electricity. The central component of a BEV is the lithium-ion battery pack, which must deliver sufficient energy and power over many years of operation while satisfying strict safety and reliability requirements. To meet these requirements, modern BEVs are equipped with a battery management system that acts as the interface between the battery and the vehicle, continuously supervising and controlling pack operation [153]. The BMS performs several key functions: cell voltage and current monitoring, temperature supervision, protection against overcharge, over-discharge and overcurrent, thermal management support, and estimation of internal battery states. By enforcing safe operating limits and optimising utilisation of the available capacity, the BMS contributes to extending battery lifetime, ensuring safety and enabling accurate range prediction for the driver.

Advanced BMS strategies increasingly integrate ageing models and state estimation algorithms to adapt control actions to the actual condition of each cell or module, rather than assuming nominal behaviour over the entire service life [154] [155].

4.1 State of Charge and State of Health

State of charge and state of health are two of the most important internal quantities for BMS operation. SOC represents the fraction of extractable capacity that remains at a given time compared to the actual maximum capacity of the cell or module, and it is often expressed as:

$$SOC = \frac{C_p}{C_{max}} * 100\ [\%]\ (eq. 16)$$

Where C_p is the remaining usable capacity and C_{max} is the maximum available capacity under given conditions. Accurate SOC estimation is essential for energy management, power-limit calculation and range prediction, but it is challenging due to the highly non-linear and time-varying behaviour of lithium-ion batteries [156].

SOH, by contrast, quantifies the deviation of the battery from its initial (beginning-of-life) condition and reflects the cumulative impact of ageing mechanisms. It can be defined in different ways, for example based on capacity fade, increase in internal

resistance, or loss of power capability, and it depends on operating history, temperature, SOC window, current rates and other stress factors. In the present work, SOH is defined experimentally as:

$$SOH = \frac{Dischage\ capacity_i}{Discharge\ capacity_{ref}} * 100\ [\%]\ (eq. 17)$$

Where $Dischage\ capacity_i$ is the measured discharge capacity at cycle i under specified test conditions, while $Discharge\ capacity_{ref}$ is the reference capacity provided [157]. This capacity-based SOH definition directly captures the progressive loss of usable energy that is most relevant for BEV range and is widely adopted in experimental ageing studies.

From a BEV perspective, SOC and SOH play complementary roles: SOC determines how much energy is immediately available for a given trip, while SOH determines how much total energy the battery can store and deliver over its lifetime. Accurate, on-board estimation of both quantities is therefore a prerequisite for safe operation, optimal utilisation of the battery and informed decisions on warranty, second-life and end-of-life strategies [158] [159] [160].

4.2 Methods for SOH Analysis

In the literature, SOH estimation for lithium-ion batteries is usually grouped into three main methodological families: experimental (or measurement-based), model-based and data-driven approaches. Each family reflects a different balance between physical interpretability, data requirements, computational complexity, and suitability for on-board implementation in automotive battery management systems. In this work, the SOH analysis is performed with an experimental, capacity-based method, and the other families are discussed to frame this choice within the broader state of the art [161] [162] [163].

4.2.1 Experimental Methods

The experimental methods determine SOH directly from controlled characterisation tests, without relying on a dynamic model or a data-driven relationship. The most common definition is capacity-based, where SOH is expressed as the ratio between the measured discharge capacity at a given cycle and a reference beginning-of-life capacity under specified test conditions ($eq. 17$), so that the gradual reduction of measured discharge capacity over

cycling directly quantifies the loss of usable energy that is most relevant for BEV range. This definition is widely adopted in ageing campaigns and in many datasets used to benchmark SOH algorithms [164].

To frame the experimental capacity-based method adopted here ($eq.17$) against predictive alternatives, *Table 7* reports a semiquantitative comparison of their main trade-offs for BEV applications. Capacity-based SOH estimation remains the pillar of experimental battery analysis, since it directly quantifies degradation via the ratio between the measured discharge capacity at a given cycle and a beginning-of-life reference under specified test conditions. This definition is widely employed in ageing campaigns and in public datasets used to benchmark SOH algorithms, where it serves as a high-fidelity reference for validation. However, its dependence on controlled characterisation tests and full charge-discharge profiles makes it intrinsically offline and time-consuming, which limits its suitability for continuous, real-time SOH estimation in operating BEVs. In contrast, predictive methods, inclusding both model-based approaches (e.g. equivalent-circuit or reduced-order electrochemical models combined with state observers or Kalman filtering) and data-driven techniques (e.g. Gaussian process regression, random forests, gradient boosting, LSTM or GRU networks), aim to estimate or forecast SOH directly from current, voltage and temperature measurements acquired during normal operation. Model-based methods update internal parameters that act as health indicators and can be embedded in the BMS, thus supporting joint estimation of SOC, SOH and sometimes internal temperature with a degree of physical interpretability, at the cost of careful model selection and computational constraints. Data-driven estimators, by learning a mapping from measured trajectories or engineered features to SOH without an explicit physical model, offer greater flexibility and can achieve very low prediction errors when trained on large, representative datasets, although their performance and universality depend strongly on the training data and their black-box nature complicates safety validation. Within the wider SOH literature, these three families, experimental, model-based and data-driven, thus form a complementary triad. The capacity-based SOH defined by $eq.17$ is frequently used as the ground-truth label even in advanced data-driven and hybrid frameworks, underlining its central role in the assessment of predictive SOH estimators.

Besides capacity tests, other experimental indicators include DC internal resistance measurements, Electrochemical Impedance Spectroscopy (EIS) and incremental capacity or differential voltage analysis, which track characteristic signatures of degradation in the

voltage-current-frequency domain [165]. EIS-based methods, for example, extract relaxation time distributions or specific impedance features that correlate with SEI growth, charge-transfer resistance or diffusion limitations, and use these as direct health markers. Incremental capacity analysis can reveal phase-transition shifts and loss of active material through changes in the differential capacity peaks along the voltage curve [166] [167].

The main strength of experimental methods is their directness: SOH is obtained from measurements that closely reflect the physical degradation of the cell or module, with minimal modelling assumptions, which makes them a natural reference for validating other approaches. Their accuracy can be very high when tests are performed under well-controlled conditions (stabilised temperature, defined current rates, sufficient rest times), and they provide detailed insight into underlying ageing mechanisms. However, these methods are time-consuming, require taking the battery off-line or imposing specific charge–discharge profiles, and therefore are not directly compatible with continuous, real-time SOH estimation in an operating BEV. For this reason, they are primarily used in laboratory studies, in the construction of public ageing datasets and in the calibration and benchmarking of model-based or data-driven estimators [168] [169] [170].

Aspect	Capacity-Based Method	Predictive Models (Model/Data-Driven)
Accuracy	High (<1-2% error in controlled lab tests) [164][168][169]	High (MAPE 0.87-2%, low RMSE across cycles) [175][176][178]
Processing Time	High (hours for full charge-discharge cycles) [168][169]	Low (real-time, milliseconds to seconds in BMS) [164][168][171]
Data/Model Requirements	Minimal (standardised capacity tests only) [164][168]	High (extensive historical data or tuned physics models) [164][168][175][176]
Interpretability	High (direct physical degradation link) [164][168]	Medium/Low (parameter tracking vs. black-box ML) [168][175][176][179]
Onboard Suitability	Low (requires offline testing) [168][169][170]	High (embedded in automotive BMS) [164][168][171][173]
Noise Robustness	High (under stabilised conditions) [168][169]	Medium/High (filtering/ML handles operational noise) [168][171][175][176]
Scalability	Low (cell/module level, not packs) [168][169]	High (fleet-wide with transfer learning) [175][176][178][179]

Table 7 Semiquantitative comparison of capacity-based and predictive SOH estimation methods for BEV applications, highlighting key trade-offs across accuracy, computational demands, interpretability and operational deployment.

4.2.2 Model-based Methods

Model-based methods estimate the SOH by tracking the evolution of parameters within an explicit battery model fitted to measured current, voltage and temperature data, and is then continuously updated during operation. Two main model classes are employed: equivalent-circuit models (ECMs), composed of voltage sources, resistors and capacitor networks that approximate the dynamic behaviour of the cell and electrochemical models (EChMs), which describe the lithium-ion transport and reaction kinetics inside electrodes and electrolyte. In ECM-based SOH estimation, parameters such as ohmic resistance, charge-transfer resistance, diffusion-related time constants or open-circuit-voltage curves are treated as health indicators and are recursively identified using state observers[13] or filtering techniques. Variants of the Kalman filter family (extended Kalman filter, unscented Kalman filter, sigma-point Kalman filter) are extensively used to jointly estimate SOC and SOH while compensating for measurement noise and model non-linearities [168] [171] [172] [173].

Electrochemical model-based methods, often derived from pseudo-two-dimensional (P2D) frameworks, can link SOH to physically meaningful quantities such as loss of lithium inventory, loss of active material and changes in diffusion coefficients or reaction rates. Reduced-order electrochemical models have been proposed to make this level of physical detail compatible with on-board computation, for example by simplifying the controlling partial differential equations and focusing on a small set of combined degradation parameters [163].

Model-based approaches have several important advantages for BEV applications: they can be embedded into the BMS and run online, using only the signals that are already measured for control (pack/module voltage, current and temperature); they support joint estimation of multiple states (SOC, SOH and internal temperature); and, when based on physically motivated models, they offer some interpretability of how operating conditions accelerate or mitigate ageing. At the same time, their performance is highly dependent on the accuracy and observability of the chosen model structure: parameter drift, unmodelled dynamics, manufacturing dispersion among cells and changing operating regimes can all deteriorate estimation accuracy. High-fidelity electrochemical models may be too

[13] State observers are algorithms that estimate the internal states of a dynamic system from its measurable inputs and outputs, using a mathematical model of the system [174].

computationally demanding for automotive microcontrollers; in practice, a compromise between model complexity and numerical efficiency must be found [163] [168].

4.2.3 Data-Driven and Hybrid SOH Methods

Data-driven methods estimate SOH by learning a mapping from measured signals (or features extracted from them) to SOH using statistical or machine-learning algorithms, without specifying an explicit physical model of the battery. Typical inputs include time-series of current, voltage and temperature during charge or discharge, along with engineered features such as characteristic voltage points, time-to-reach thresholds, partial-capacity segments or impedance features. Algorithms range from classical regression models (e.g. Gaussian process regression, support vector regression, relevance vector machines) to methods aggregation (random forests[14], gradient boosting[15], XGBoost[16]) and deep-learning architectures (feed-forward neural networks, convolutional neural networks, recurrent neural networks such as LSTM and GRU) [175] [176] [177] [178].

Recent reviews highlight that data-driven SOH estimators can achieve very low prediction errors when trained on large, high-quality datasets that capture the relevant operating and ageing conditions. Deep-learning models, in particular, can automatically extract complex temporal and non-linear features from raw voltage-current trajectories, and have shown improved robustness to measurement noise compared with simpler empirical models. At the same time, their performance is strongly linked to the representativeness of the training data: models trained on a specific chemistry, cell format or duty cycle may not generalise to different BEV platforms or to field conditions that differ from laboratory profiles. Purely data-driven models are often treated as black-boxes, which complicates their physical interpretation and safety validation, and their computational requirements can be non-trivial for embedded implementations [168] [175] [176] [179] [180].

To address these limitations, hybrid approaches that combine physical insight and data-driven learning are increasingly proposed. Examples include using electrochemical or ECM models to generate informative health features for machine-learning regressors, constraining neural networks with physically meaningful inputs and outputs, or fusing

[14] Builds hundreds of decision trees on random data subsets and features (bagging), then averages predictions (regression) or majority votes (classification) to reduce overfitting and variance [181].
[15] Sequentially trains weak trees where each corrects errors (residuals) of prior ones via gradient descent on a loss function, yielding high accuracy but risking overfitting without tuning [182].
[16] Optimised “extreme” gradient boosting library with regularization, parallel processing, missing value handling, and tree pruning for speed and precision on large datasets [183].

multiple expert models to balance accuracy and interpretability. In many of these works, experimentally measured capacity-based SOH, defined in the same form as $eq.17$, is used as the ground-truth label for training and validation, emphasising the central role of experimental SOH analysis even in advanced data-driven frameworks [177] [178] [180].

4.3 SOH Analysis

The state-of-health analysis presented in this master's thesis has been carried out for two different 18650-type battery chemistries. In particular, LFP and NMC (Nickel Manganese Cobalt oxide) were examined: the first one offers greater thermal stability and overall safety, but, at the same time, has lower specific energy compared with NMC. The analysis has been conducted at three different temperature levels, 15°C, 25°C and 35°C, in order to examine how the SOH evolution varies with temperature; this parameter is fundamental because it strongly influences the degradation mechanisms of lithium-ion cells. At higher temperatures, side reactions at the electrodes and electrolyte decomposition accelerate, leading to faster growth of the solid-electrolyte interphase and loss of active lithium. Elevated temperature also increases mechanical and structural stress inside the electrodes during cycling. For these reasons, simulations at 35°C show greater degradation than at 25°C and 15°C, since the ageing reactions become more intense as the temperature rises.

4.3.1 MATLAB Implementation for SOH Analysis

Thanks to the elaboration of a MATLAB script, it has been possible to calculate the SOH as:

$$SOH = \frac{Dischage\ capacity_i}{Discharge\ capacity_{ref}} * 100\ [\%]\ (eq.17)$$

As explained in the previous chapter, this formula enables the experimental evaluation of SOH, given the number of cycles and the corresponding discharge capacity value. The number of test cycle and their respective value of discharge capacity have been provided by BatteryArchive.org, a public database of lithium-ion battery cycling and disruptive test data [184].

In *Figure 26* it is explained how the Excel file, obtained from BatteryArchive.org, is read in MATLAB and preserved in its full detail (name, values, digit, special characters).

```
4   %% Import Data
5   filename = 'SNL_18650_LFP_15C_0-100_0.5-1C_a_cycle_data.xlsx';
6   opts = detectImportOptions(filename);
7   opts.VariableNamingRule = 'preserve';
8   data = readtable(filename, opts);
9
```

Figure 26 Import Data.

Next, a table in the software is created. The following section (*Figure 27*) defines the value of the $Discharge\ capacity_{ref}$, denoted *nominal_capacity,* and starts to read the column of interest of the previous uploaded Excel's file. In the end, the SOH is evaluated.

```
10      %% Extract data
11      nominal_capacity = 1.10;  % Ah
12      cycle_index = data{:, 1};
13      discharge_capacity = data{:, 10};
14      SOH_measured = data{:, 17};
15
16      % Calculate SOH
17      SOH_calculated = (discharge_capacity / nominal_capacity) * 100;
```

Figure 27 Extract Data.

A preliminary check for potential numerical inconsistencies is first carried out to ensure the reliability of the processed dataset. In particular, the script verifies the presence of *NaN* (Not a Number) entries, which may arise from missing measurements, failed computations, or corrupted data points.

The MATLAB code shown in *Figure 28* defines a logical index (*valid_idx*) that identifies only those samples for which the cycle index, discharge capacity, and both calculated and measured SOH values are all finite (i.e. not *NaN*). This index is then used to filter each corresponding vector, so that subsequent analysis is performed exclusively on clean, numerically valid data.

```
19      %% Clean data - Remove NaN
20      valid_idx = ~isnan(cycle_index) & ~isnan(discharge_capacity) & ~isnan(SOH_measured);
21      cycle_index = cycle_index(valid_idx);
22      discharge_capacity = discharge_capacity(valid_idx);
23      SOH_calculated = SOH_calculated(valid_idx);
24      SOH_measured = SOH_measured(valid_idx);
```

Figure 28 Clean Data. Remove NaN.

A first graphical overview is now possible: in fact, *Figure 29* shows all the data extrapolated from the Excel file (green line). The second line, the black dashed one, represents the ideal trend that the SOH should follow. This part is obtained by implementing a linear regression performed on the filtered SOH data as a function of cycle number, in order to obtain a compact estimate of the long-term degradation trend. The *polift* command computes the coefficients of a first-order polynomial, which are then used by *polyval* command to reconstruct the best-fit SOH curve; the absolute value of the slope $p(1)$, scaled by 100, provides the degradation rate expressed as percentage SOH loss per 100 cycles (*Figure 30*). As expected, the majority of the points appear to follow a linear trend, but some

SOH values lie far from this ideal trend (*Figure 31*). These data points must be removed during the analysis, otherwise they will compromise the final result. In fact, *Figure 32* shows the difference in reaching the EOL in terms of number of cycles with raw data (no filter applied) and with filtered data, illustrating how data processing slightly reduces the estimated degradation rate and extends the predicted cycle life. The end-of-life, defined as 80% of its initial capacity, is measured as:

$$n_{EOL} = \frac{80 - p_2}{p_1} \quad (eq. 18)$$

Where p_1 represents the slope, so how much the SOH decrease every cycle, while p_2 is the value of SOH at cycle 0.

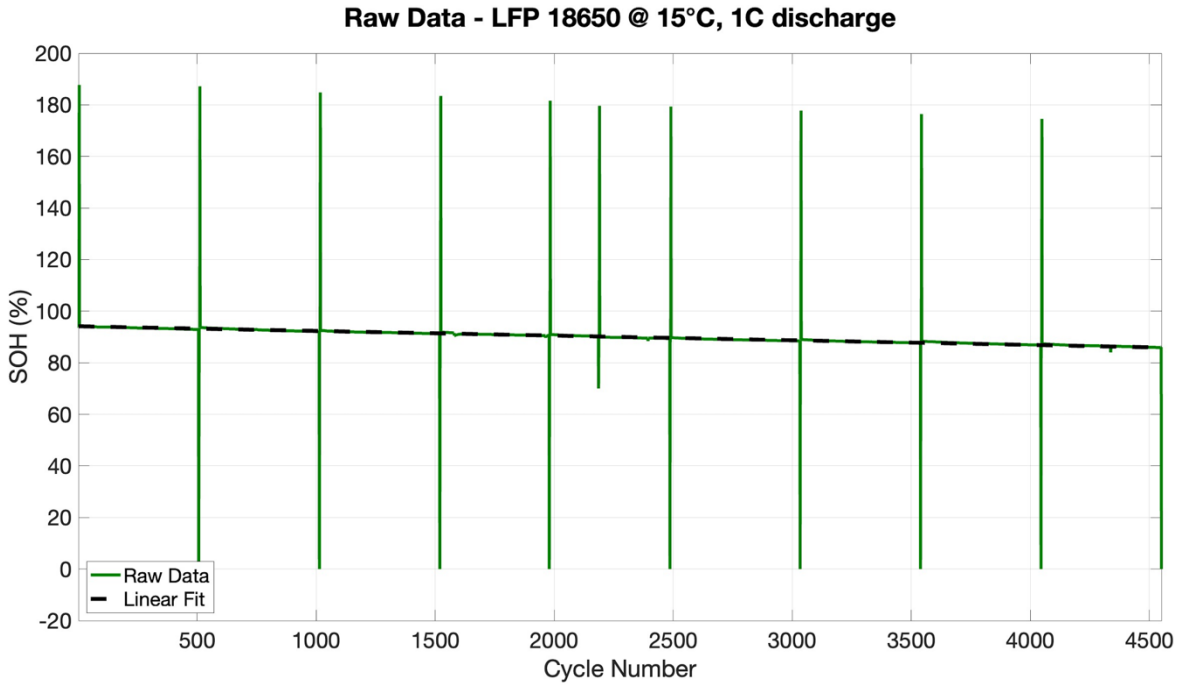

Figure 29 SOH behaviour with Raw Data.

```
40    %% Fit lineare (su dati filtrati)
41    p        = polyfit(cycle_final, SOH_final, 1);
42    SOH_fit  = polyval(p, cycle_final);
43    deg_rate = abs(p(1)) * 100; % %/100 cycles
```

Figure 30 Definition of the Linear trend.

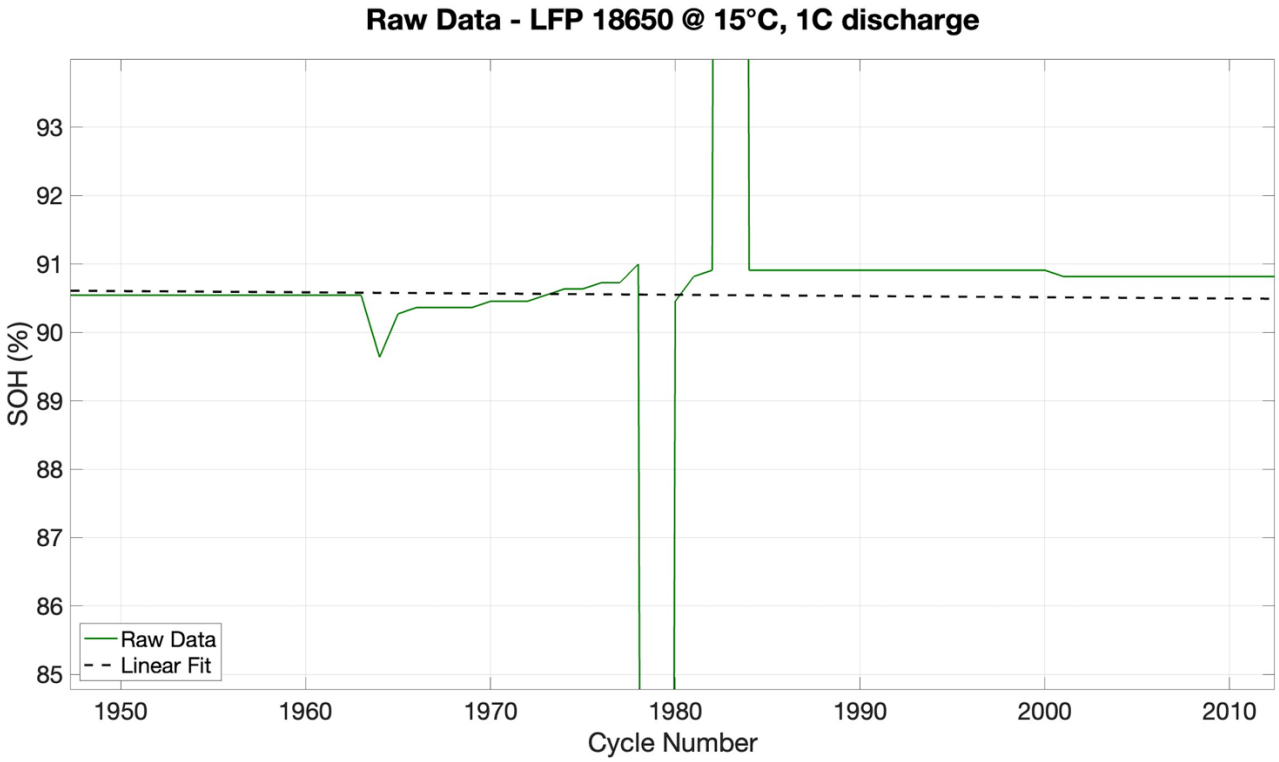

Figure 31 Zoomed view of raw LFP 18650 data at 15°C (1C discharge), highlighting that most SOH points closely follow the black linear fit line, while some outliers deviate significantly upwards and downwards.

```
--- Degradation Rates ---
Raw Data: 0.181 %/100 cycles
Filtered Data: 0.176 %/100 cycles
Smoothed Data: 0.176 %/100 cycles

--- Projected EOL (80% SOH) ---
Using Raw Data: ~7544 cycles
Using Filtered Data: ~7770 cycles
Using Smoothed Data: ~7883 cycles
```

Figure 32 Comparison of degradation rates and projected EOL (80% SOH) obtained from raw, filtered, and smoothed SOH data.

Next, a filtering stage (*Figure 33*) is introduced to remove all data lacking physical meaning because during preliminary analysis (green line in *Figure 29*), several SOH points were found to be inconsistent with physically plausible degradation, exhibiting sudden increases (>105%) or decreases (<70%) that are incompatible with the smooth, monotonic capacity fade expected for lithium-ion cells operated under constant cycling conditions.

These non-physical values are typically caused by measurement noise, logging errors, or incorrect reference capacity calculation rather than genuine changes in cell health and would therefore distort the estimation of the degradation trend if left unfiltered. For this reason, a first filtering step was applied to remove obvious outliers (e.g., SOH values outside a reasonable range or showing large jumps with respect to neighbouring cycles), ensuring that the subsequent regression is fitted only on data points that reflect the actual ageing behaviour of the cell. A similar data quality issue is reported by Alamin et al. (2024), who, working on a similar dataset, found it necessary to discard false SOH values exhibiting non-decreasing trends or anomalous drastic jumps prior to model training [185]. Then, a second filtering method using the standard deviation is applied to remove false SOH estimates caused by measurement noise or algorithmic errors. First, the mean $\bar{x}$ and standard deviation σ of the SOH values are computed, and only points within the interval $\bar{x} \pm 3\sigma$ are kept, following the classical three-sigma rule for outlier rejection. This criterion preserves the vast majority of physically plausible values while discarding statistically rare anomalies. A similar three-sigma-based strategy is adopted by Hu et al. (2026), who apply standard-deviation-driven outlier rejection when constructing randomised and robust operator-network models for battery health estimation, thereby ensuring that false SOH samples do not bias the learned degradation trends [186].

The mathematics behind this implementation is the following:

- Mean: $\bar{x} = \frac{1}{n} \sum_{i=1}^{n} x_i \quad (eq. 19)$
- Standard Deviation: $\sigma = \sqrt{\frac{1}{n} \sum_{i=1}^{n} (x_i - \bar{x})^2} \quad (eq. 20)$
- 3-Sigma Rule[17]: in a normal distribution, 99.7% of the data fall within $\pm 3\sigma$ of the mean.

[17] The 3σ rule is a statistical guideline for spotting outliers in data by using the standard deviation (σ), which quantifies how much your data typically varies from the average (mean, $\bar{x}$) [187].

```
%% Remove outliers - Filtro robusto
% Metodo 1: Rimuovi valori fuori range fisico
physical_limit_idx = (SOH_calculated >= 50) & (SOH_calculated <= 110);
cycle_clean = cycle_index(physical_limit_idx);
SOH_clean = SOH_calculated(physical_limit_idx);
SOH_meas_clean = SOH_measured(physical_limit_idx);
discharge_clean = discharge_capacity(physical_limit_idx);

% Metodo 2: Rimuovi outlier statistici (oltre 3 deviazioni standard)
mean_SOH = mean(SOH_clean);
std_SOH = std(SOH_clean);
outlier_idx = abs(SOH_clean - mean_SOH) < 3*std_SOH;
cycle_final = cycle_clean(outlier_idx);
SOH_final = SOH_clean(outlier_idx);
SOH_meas_final = SOH_meas_clean(outlier_idx);
discharge_final = discharge_clean(outlier_idx);

fprintf('Dati originali: %d | Dopo pulizia: %d | Rimossi: %d outlier\n', ...
        length(cycle_index), length(cycle_final), length(cycle_index)-length(cycle_final));

```

Figure 33 Filters implementation in MATLAB.

After these implementations, the resulting graph is more realistic and representative (*Figure 34).* In the plot showing the data filtered with the applied methods (blue line), the "spikes", i.e. physically impossible values, have been removed, yielding a trend similar to the ideal one. In *Figure 35*, following the two-stage filtering procedure described above, an additional smoothing step is applied to the cleaned SOH data to further reduce high-frequency noise while preserving the underlying long-term degradation trend. Specifically, a moving-average filter with a window size of $w = 10$ cycles is employed, so that each smoothed SOH value at cycle k is computed as:

$$SOH_{smooth}(k) = \frac{1}{w}\sum_{i=0}^{w-1} SOH_{filtered}(k-i) \quad (eq.21)$$

where $SOH_{filtered}(k)$ denotes the SOH value after the preceding filtering stage.

A similar preprocessing strategy is adopted by Zhang et al. (2022), who apply moving-average smoothing to cycle-wise SOH (capacity) trajectories to suppress high-frequency measurement noise before training a data-driven prognostic model for lithium-ion batteries [188]. This operation attenuates cycle-to-cycle fluctuations caused by measurement noise and minor test inconsistencies, without distorting the macroscopic capacity-fade behaviour.

The chosen window size $w = 10$ represents a compromise between noise suppression and temporal resolution: excessively large windows risk masking genuine degradation features such as knee points, which are particularly relevant in LFP chemistries characterised by a flat voltage plateau. With this setting, the resulting SOH trajectory (red line in *Figure*

35) appears cleaner and more linear, while still retaining physically meaningful degradation features.

The MATLAB script that shows this part is illustrated in *Figure 38*, where this code segment applies a simple post-processing step to reduce noise in the SOH trajectory by means of a moving average filter. When the number of available cycles exceeds the predefined window length (here set to 10), the *movmean* function replaces each SOH value with the average of its neighbouring points, producing a smoother and more readable SOH trend; if fewer than 10 cycles are present, the original SOH series is retained without modification.

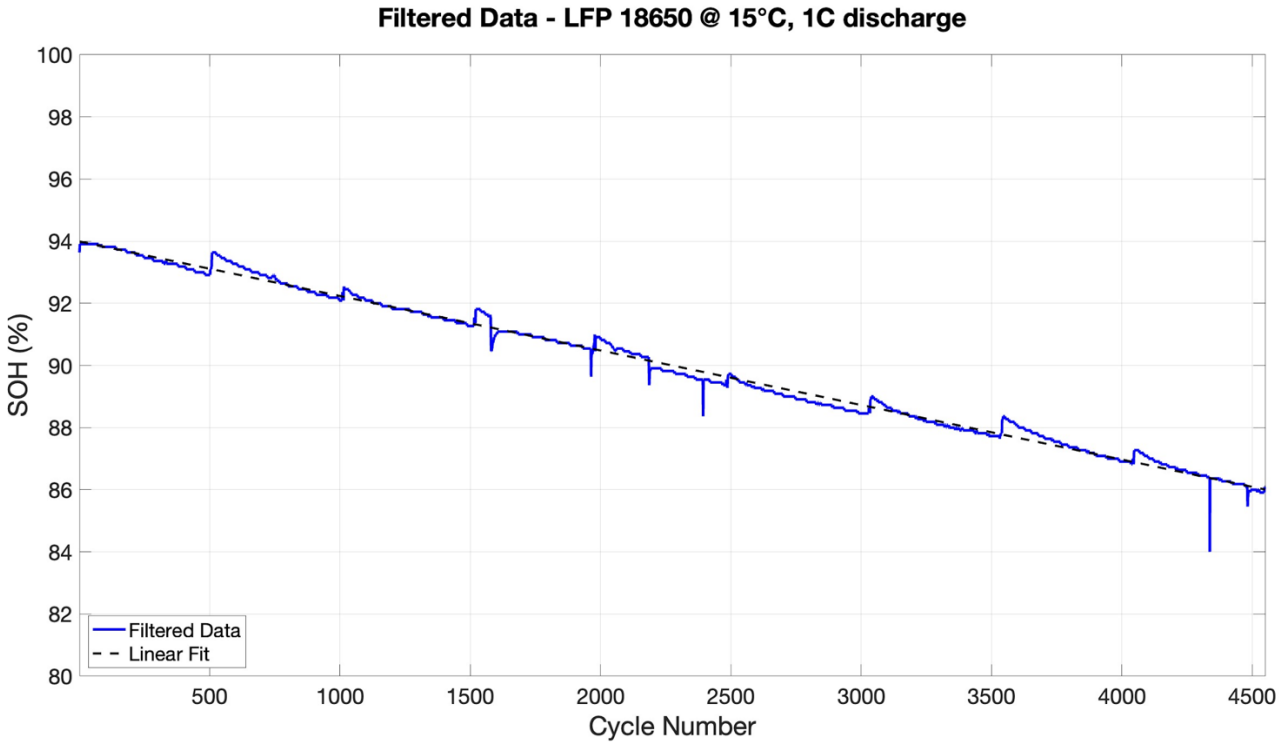

Figure 34 SOH behaviour with filtered data.

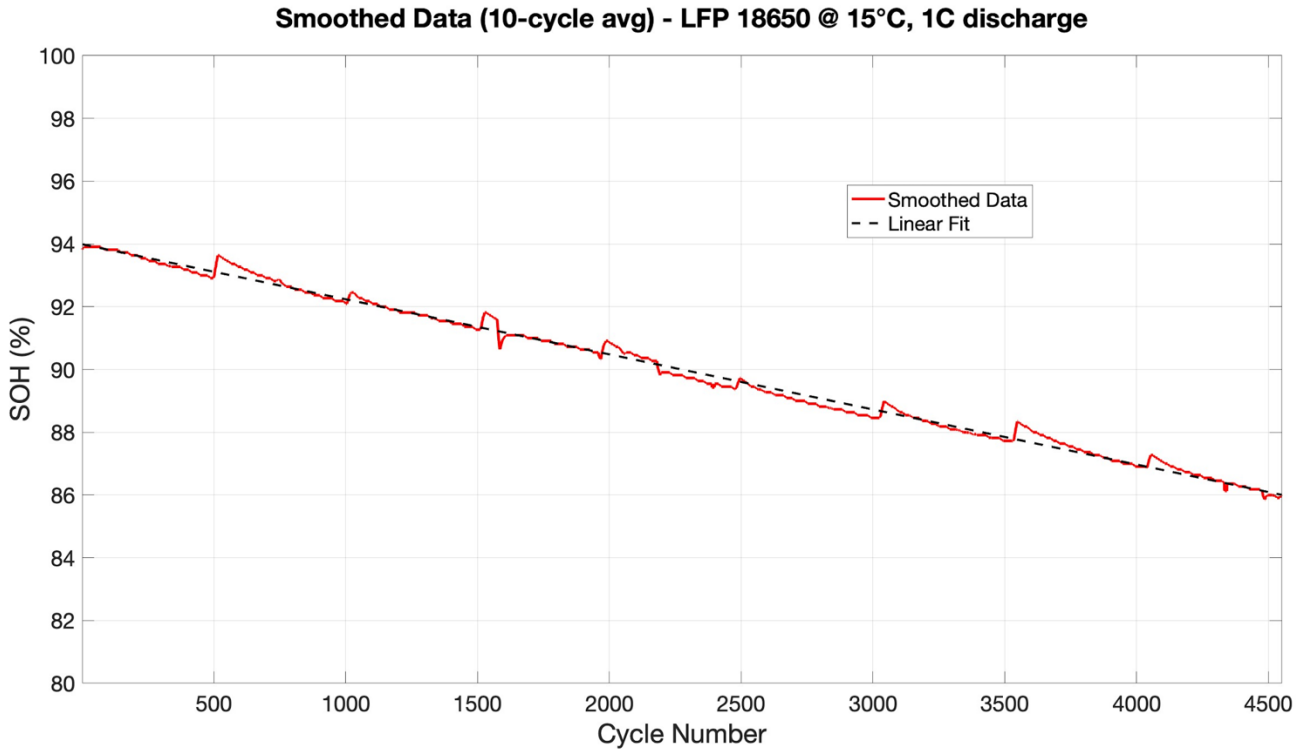

Figure 35 SOH behaviour after the application of the moving-average filter, LFP chemistry case 15°C.

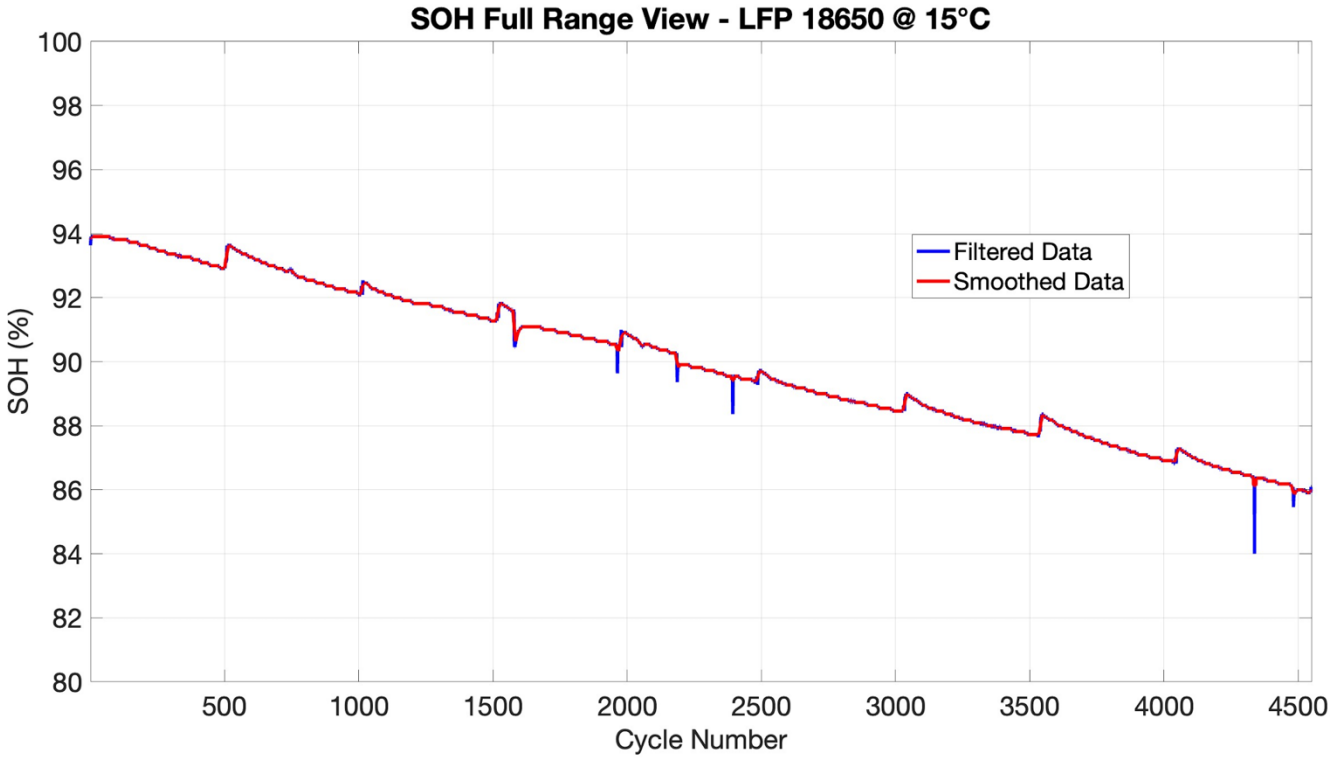

Figure 36 Comparison between Filtered data and Smoothed data.

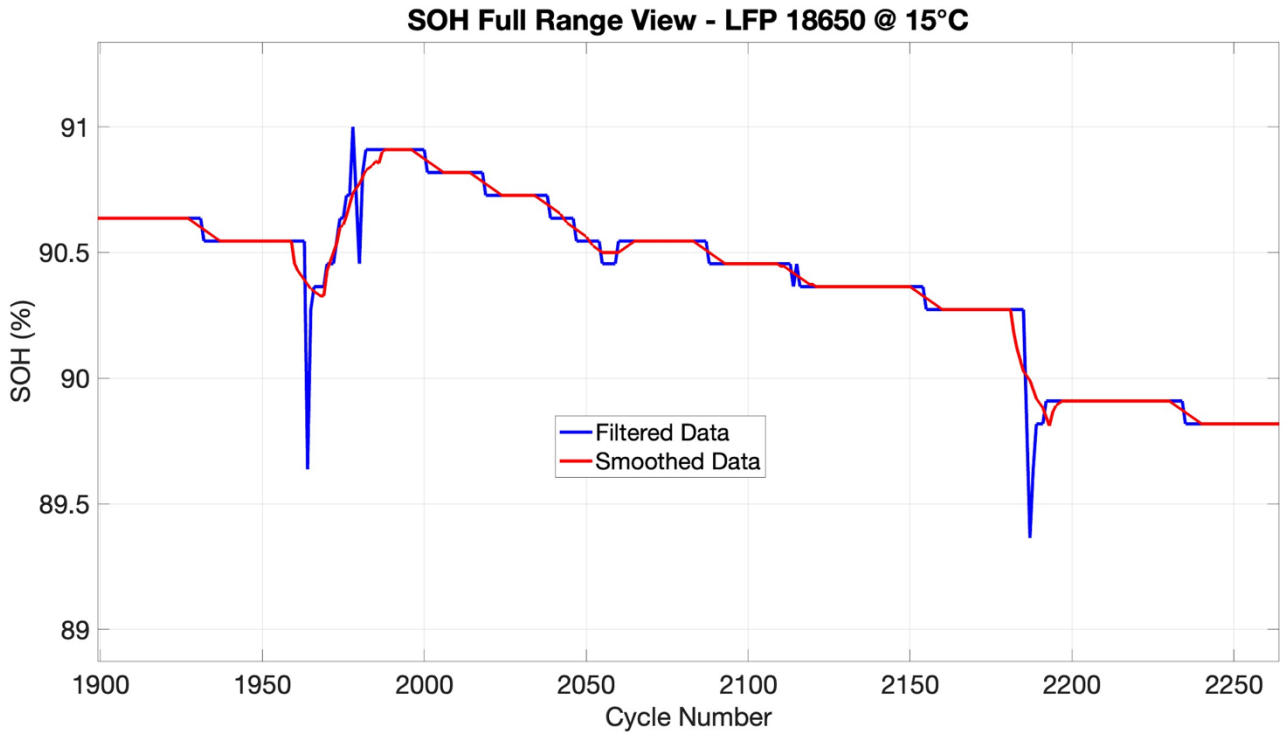

Figure 37 Zoomed section to better understand the differences between Filtered and Smoothed data.

```
33    %% Smoothing con Moving Average
34    window = 10;
35    if length(cycle_final) > window
36        SOH_smooth = movmean(SOH_final, window);
37    else
38        SOH_smooth = SOH_final;
39    end
```

Figure 38 Smoothing with Moving Average.

In conclusion, R-squared (R^2)[18], also known as the coefficient of determination, was employed to quantify the goodness of fit of the linear regression model used to describe the SOH trajectory as a function of cycle number. In this context, R^2 expresses which fraction of the total variability observed in the SOH measurements is explained by the regression line rather than by random scatter around the mean value. Formally, it is defined as:

$$R^2 = 1 - \frac{RSS}{TSS} \quad (eq. 22)$$

[18] MathWorks. (2026). *Coefficient of determination (R-squared)*. Statistics and Machine Learning Toolbox Documentation. from https://it.mathworks.com/help/stats/coefficient-of-determination-r-squared.html

where *RSS* is the sum of squared residuals between the measured SOH values and the fitted model predictions, and *TSS* is the total sum of squares with respect to the mean SOH.

Using R^2 is particularly appropriate here because the aim is to verify that a simple linear model is sufficient to capture the capacity fade behaviour under each operating condition, without relying on more complex, highly parameterised models. High R^2 values (close to 1) indicate that the linear trend accounts for most of the SOH variation and that the remaining unexplained variance is relatively small, thereby supporting the use of a linear degradation rate $k(T)$ for comparing different temperatures. In contrast, low R^2 values would suggest that the degradation pathway is poorly represented by a straight line, calling either for a different functional form or for a more careful inspection of measurement noise and outliers.

In practical terms, the regression and the corresponding R^2 values were obtained in MATLAB using the *fitlm* function, which computes the least-squares linear fit and reports the ordinary coefficient of determination as *mdl.Rsquared.Ordinary*. This provides a consistent quantitative measure that can be directly compared across the different datasets (e.g. various temperatures), ensuring that any analysis of the degradation coefficients $k(T)$ is based on models with demonstrably adequate explanatory power.

For each temperature, the SOH trajectory as a function of cycle number was approximated by a linear model of the form:

$$SOH(N,T) = 100 - k(T) * N \ \ (eq. 23)$$

where $k(T)$denotes the degradation rate at temperature T, expressed in %SOH loss per cycle.

The coefficient $k(T)$ therefore represents the average capacity fade rate under the specific operating condition and provides a compact metric to compare the impact of temperature on ageing behaviour.

```
--- Degradation Coefficients (per cycle) ---
k_raw      = 0.00181 %/cycle
k_filtered = 0.00176 %/cycle
k_smooth   = 0.00176 %/cycle

--- R-squared of Linear Fits ---
R2_raw      = 0.1417
R2_filtered = 0.9937
R2_smooth   = 0.9943

--- Percentage Error (SOH_calculated vs SOH_measured) ---
Mean error = 0.00 %
Max  error = 0.00 %
```

Figure 39 Degradation Coefficients, Coefficient of Determination and Percentage Error.

4.3.2 Analysis on LFP chemistry

The first analysed chemistry at the cathode, which is LFP, has been characterised by the following parameters:

- Number of cycles (it depends on the available data).
- Discharge capacity of reference: 1.10 Ah.
- Battery type: 18650 (*Figure 40*).
- Temperature: 15°C, 25°C and 35°C.

Figure 40 Battery 18650 [189].

Performing three analyses on the same chemistry at different temperature levels (15°C, 25°C, and 35°C) proved useful in better understanding SOH behaviour. Higher temperatures accelerate key degradation processes in lithium-ion batteries, such as solid-electrolyte interphase growth on the anode, electrolyte decomposition, and cathode structural changes, leading to faster capacity fade. These reactions follow Arrhenius kinetics, roughly doubling every 10°C rise, which explains the more pronounced SOH decline at 35 °C [190] [191].

From the analysis conducted at 15 °C, the following results were obtained:

```
Raw data: 4550 | After Filtering: 4530 | Removed: 20 outlier

========== SOH Analysis Summary ==========
Battery: LFP 18650, Nominal Capacity: 1.10 Ah
Test Conditions: 15°C, 0.5C charge, 1C discharge
Total Cycles Analyzed: 4530

Initial SOH: 93.64%
Final SOH: 86.09%
Total Capacity Loss: 7.55%
Average Degradation Rate: 0.0018 %/cycle
Average Degradation Rate: 0.176 %/100 cycles

Projected EOL (80% SOH): ~7770 cycles
```

Figure 41 Outcomes for battery LFP 18650 at 15°C.

Figure 41 shows SOH behaviour over 4,550 cycles of which only 4,530 where analysed (due to the filtering action), for a battery starting at a SOH of 93.64% discharged at 15°C. The graphical result can be observed in *Figure 35*.

From the analysis conducted at 25 °C, the following results were obtained:

```
Raw data: 3546 | After Filtering: 3527 | Removed: 19 outlier

========== SOH Analysis Summary ==========
Battery: LFP 18650, Nominal Capacity: 1.10 Ah
Test Conditions: 25°C, 0.5C charge, 1C discharge
Total Cycles Analyzed: 3527

Initial SOH: 93.82%
Final SOH: 85.82%
Total Capacity Loss: 8.00%
Average Degradation Rate: 0.0023 %/cycle
Average Degradation Rate: 0.230 %/100 cycles

Projected EOL (80% SOH): ~6011 cycles
```

Figure 42 Outcomes for battery LFP 18650 at 25°C.

Figure 42 shows SOH behaviour over 3,546 cycles of which only 3,527 where analysed (due to the filtering action), for a battery starting at a SOH of 93.82% discharged at 25°C, while in *Figure 43* it is possible to see its graphical representation.

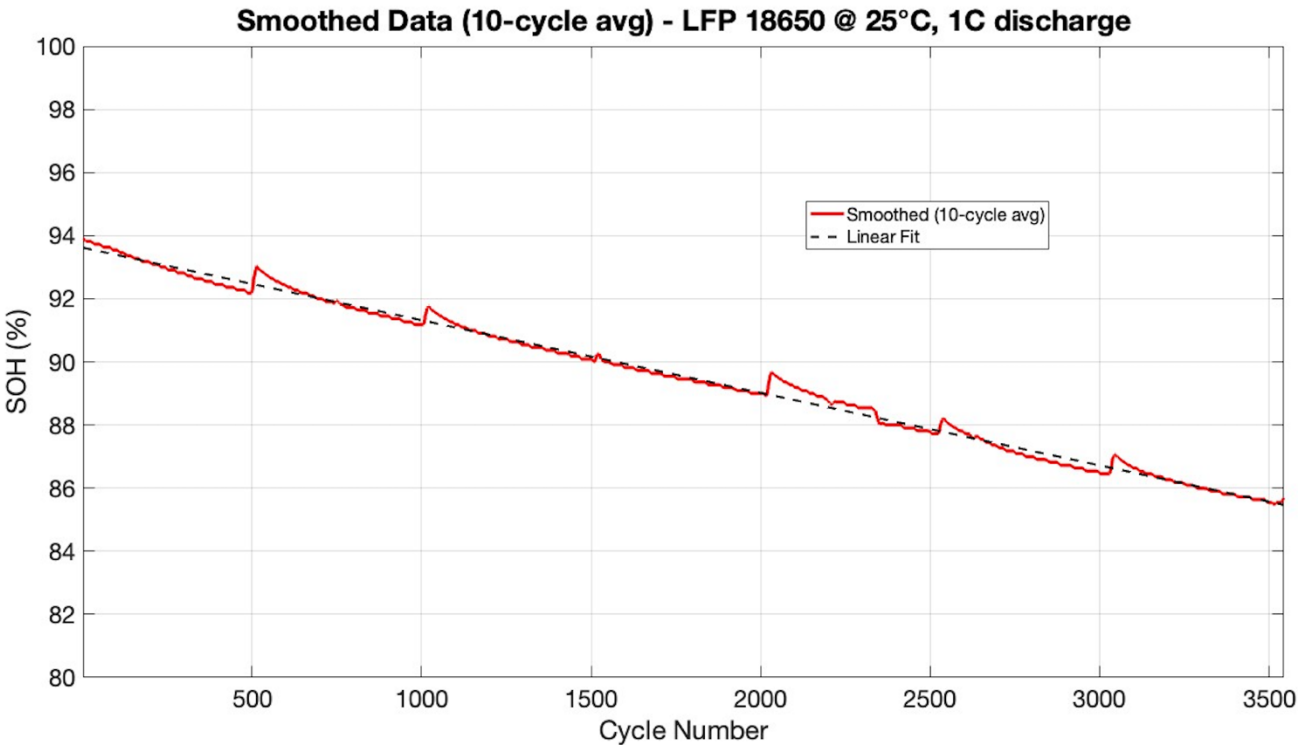

Figure 43 SOH behaviour for LFP chemistry at 25°C.

From the analysis conducted at 35 °C, the following results were obtained:

```
Raw data: 3155 | After Filtering: 3129 | Removed: 26 outlier

========== SOH Analysis Summary ==========
Battery: LFP 18650, Nominal Capacity: 1.10 Ah
Test Conditions: 35°C, 0.5C charge, 1C discharge
Total Cycles Analyzed: 3129

Initial SOH: 97.82%
Final SOH: 83.45%
Total Capacity Loss: 14.36%
Average Degradation Rate: 0.0037 %/cycle
Average Degradation Rate: 0.375 %/100 cycles

Projected EOL (80% SOH): ~4755 cycles
```

Figure 44 Outcomes for battery LFP 18650 at 35°C.

Figure 44 shows SOH behaviour over 3,155 cycles of which only 3,129 where analysed (due to the filtering action), for a battery starting at a SOH of 97.82% discharged at 35°C, while in *Figure 43* it is possible to see its graphical representation.

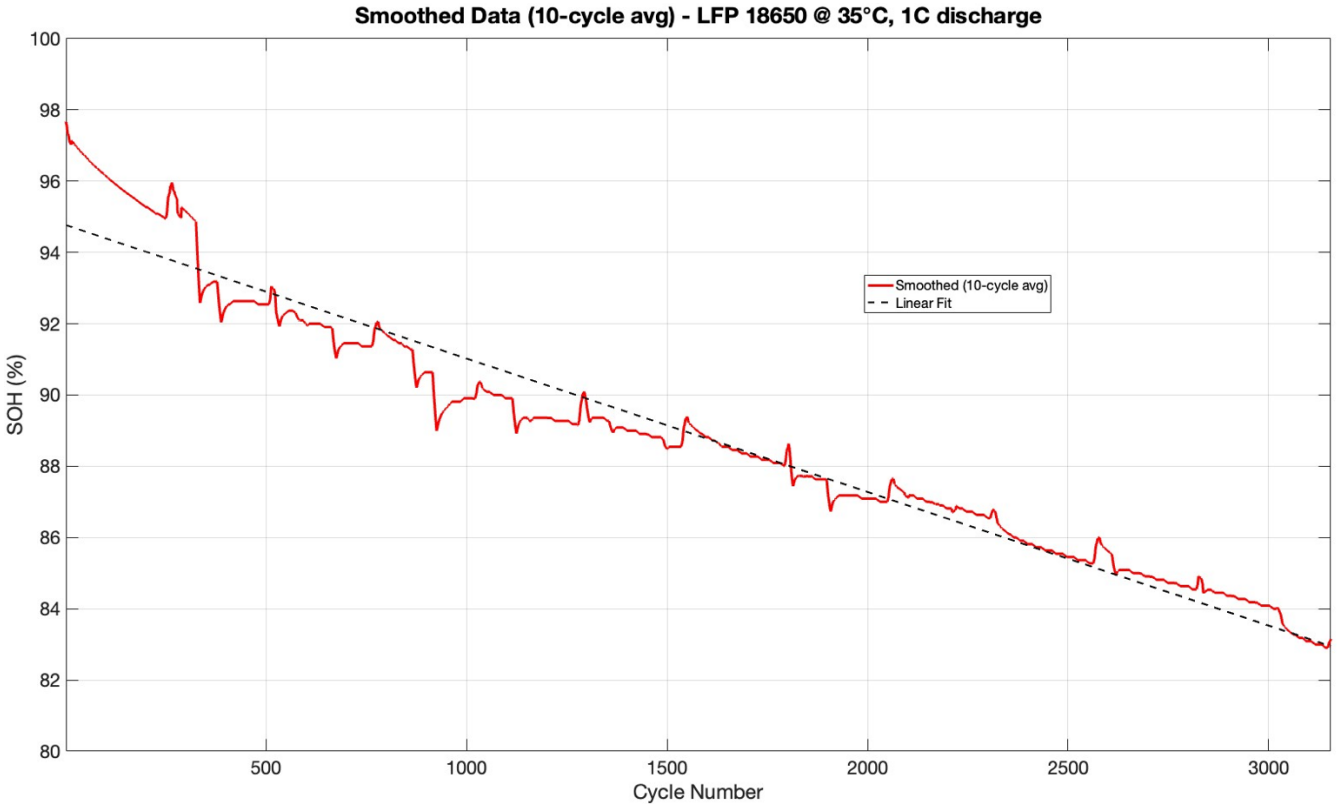

Figure 45 SOH behaviour for LFP chemistry at 35°C.

In order to better understand the differences between the three SOH behaviours at different operating temperatures, it is instructive to examine them within a single comparative plot, as shown in *Figure 46*. The most immediately apparent observation is that the cell cycled at 15°C exhibits the highest SOH retention throughout its entire lifetime, reaching a projected end-of-life, defined as the cycle at which SOH drops to 80% of the nominal capacity, at approximately 7,770 cycles based on the linear fit of the filtered data. By contrast, the cell tested at 25°C reaches the EOL threshold at approximately 6,011 cycles, while the cell operated at 35°C reaches EOL after only approximately 4,755 cycles, despite starting from a notably higher initial SOH value of 97.82% compared to 93.64% at 15°C.

This progressive reduction in cycle life with increasing temperature is consistent with well-established degradation mechanisms in LFP/graphite cells. Temperature plays a fundamental role in accelerating both LLI and LAM at the cathode and anode. In particular, at elevated temperatures, the rate of electrolyte decomposition increases significantly, accelerating the consumption of cyclable lithium through the continuous growth and reformation of the solid-electrolyte interphase layer on the graphite anode. Sun et al. (2017) demonstrated that for LiFePO4/graphite cells cycled at temperatures between 25°C and 55°C, the capacity fade rate is strongly dependent on ambient temperature, with the cell

lifetime at 55°C being approximately one-seventh of that observed at room temperature, due to the dominant contribution of enhanced electrolyte decomposition above 35°C [192]. This finding is further confirmed by Zhang et al. (2011), who reported that capacity fade in LFP cells after 600 cycles was 14.3% at 45°C, whilst at lower test temperatures the primary degradation mechanism shifts from capacity loss to power fade, driven by SEI layer growth on the graphite anode and increased interfacial resistance [193].

The degradation rate observed in this study (rising from 0.176%/100 cycles at 15°C to 0.375%/100 cycles at 35°C) is consistent with these findings, confirming that even a moderate temperature increase of 20°C can more than double the rate of capacity fade in LFP 18650 cells under 1C discharge conditions.

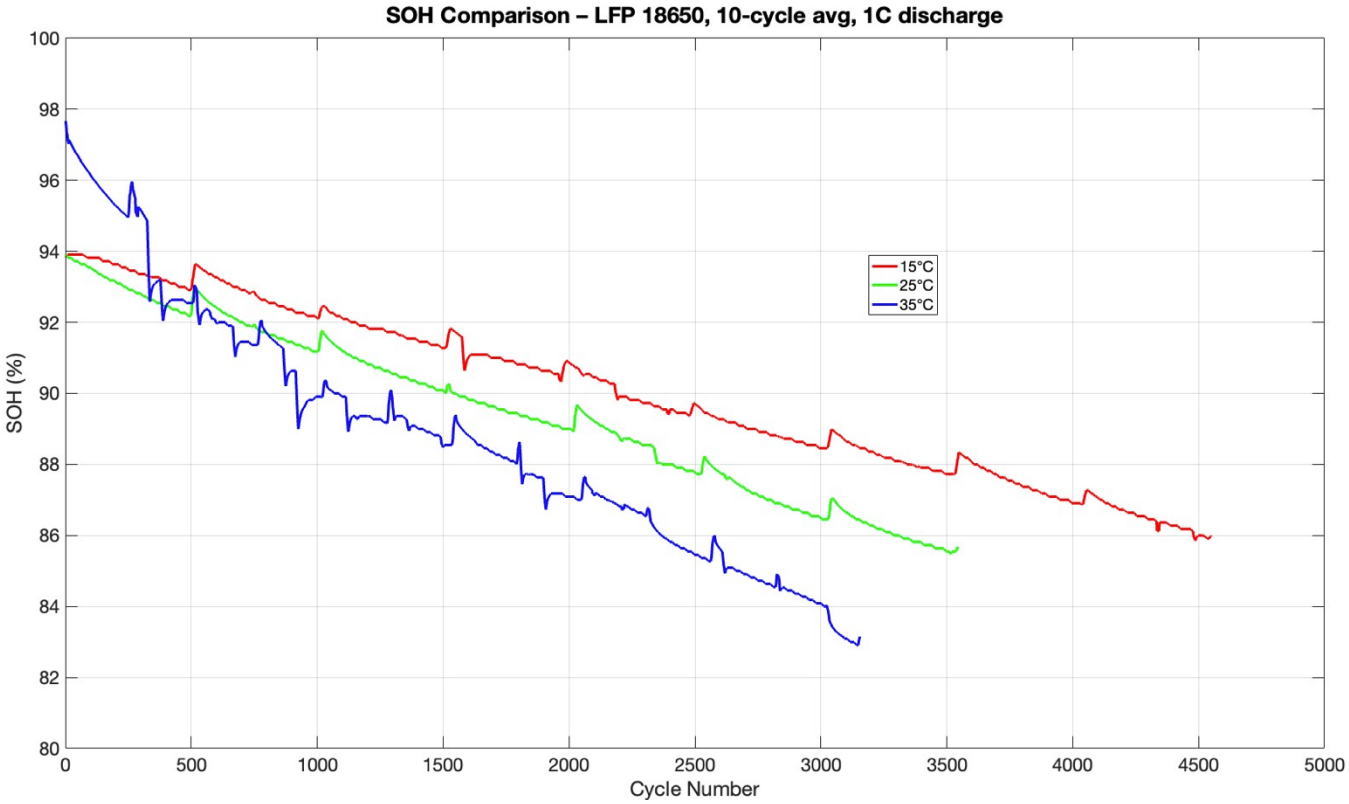

Figure 46 Full view of three SOH behaviours for LFP chemistry: 15°C, 25°C, 35°C.

Parameter	15°C	25°C	35°C
Initial SOH (%)	93.64	93.82	97.82
Final SOH (%)	86.09	85.82	83.45
Total Capacity Loss (%)	7.55	8.00	14.36
Slope (% / cycle)	−0.0018	−0.0023	−0.0037
Avg. Degradation Rate (% / cycle)	0.0018	0.0023	0.0037
Avg. Degradation Rate (% / 100 cycles)	0.176	0.230	0.375
Projected EOL @ 80% SOH (cycles)	~7,770	~6,011	~4,755

Table 8 SOH degradation metrics for battery LFP 18650 cells at 15°C, 25°C and 35°C (0.5C charge, 1C discharge). EOL defined at 80% of nominal capacity (1.10 Ah).

4.3.3 Analysis on NMC chemistry

The other analysed chemistry is NMC: it has been characterised by the following parameters:

- Number of cycles (it depends on the available data).
- Discharge capacity of reference: 3.00 Ah.
- Battery type: 18650 (*Figure 40*).
- Temperature: 15°C, 25°C and 35°C.

Analysing the same LFP chemistry at three temperature levels (15°C, 25°C, and 35°C) confirmed the expected Arrhenius-type dependence of SOH on temperature: capacity fade and SOH loss became noticeably more severe as the cell was cycled at higher temperatures, with the degradation rate at 35°C being markedly greater than at 15°C and 25°C, consistent with reaction rates that approximately double for every 10°C increase [190] [191]. Building on this result, the same experimental procedure was then applied to an NMC cell and tested under the same three temperature conditions but with a higher nominal discharge capacity of 3.00 Ah, compared with 1.10 Ah for the LFP cell, so that any differences in SOH evolution reflect both the change in chemistry and the larger amount of active material. In this context, several experimental studies have shown that NMC cells tend to exhibit stronger temperature-driven degradation than LFP, with faster capacity loss under high-temperature cycling and calendar storage, even though LFP can be more sensitive at very high state of charge, so one may expect a more pronounced SOH decay at 35°C for the NMC cell than for the LFP cell under comparable operating conditions [194] [195] [196].

However, in the present dataset, the NMC cell exhibits a slower degradation at 35°C than at 15°C, suggesting a non-monotonic temperature dependence of ageing under these specific cycling conditions, in contrast with the simple Arrhenius-type trend observed for the LFP cell.

From the analysis conducted at 15 °C, the following results were obtained:

```
Raw data: 512 | After Filtering: 508 | Removed: 4 outlier
EOL reached in dataset at cycle 71 (SOH_smooth = 79.89%)

========== SOH Analysis Summary ==========
Battery: NMC 18650, Nominal Capacity: 3.00 Ah
Test Conditions: 15°C, 0.5C charge, 1C discharge
Total Cycles Analyzed: 508

Initial SOH:         89.90%
Final SOH:           54.27%
Total Capacity Loss: 35.63%
Degradation Rate:    0.0551 %/cycle
Degradation Rate:    5.506 %/100 cycles

--- EOL (SOH = 80%) ---
EOL source: ACTUAL (observed in smoothed data)
EOL cycle:  71  (SOH_smooth = 79.89%)
```

Figure 47 Outcomes for battery NMC 18650 at 15°C

The battery initially exhibits a state of health of 89.90%, which decreases to 54.27% after 508 cycles; this cycle count was obtained after applying the same data-filtering criteria used for the LFP case. The fact that the experimental data exceed the end-of-life threshold (dashed magenta line in *Figure 48*), which in contrast to the LFP analysis is actually reached after 71 cycles within the measured interval rather than only shown as a projection, indicates a more pronounced degradation of the cell. This behaviour can be attributed both to the operating temperature and to the reference discharge capacity of 3 Ah, which is consistent with commercially available 18650 NMC cells reported in the literature and provided by BatteryArchive.org [184] [197] [198].

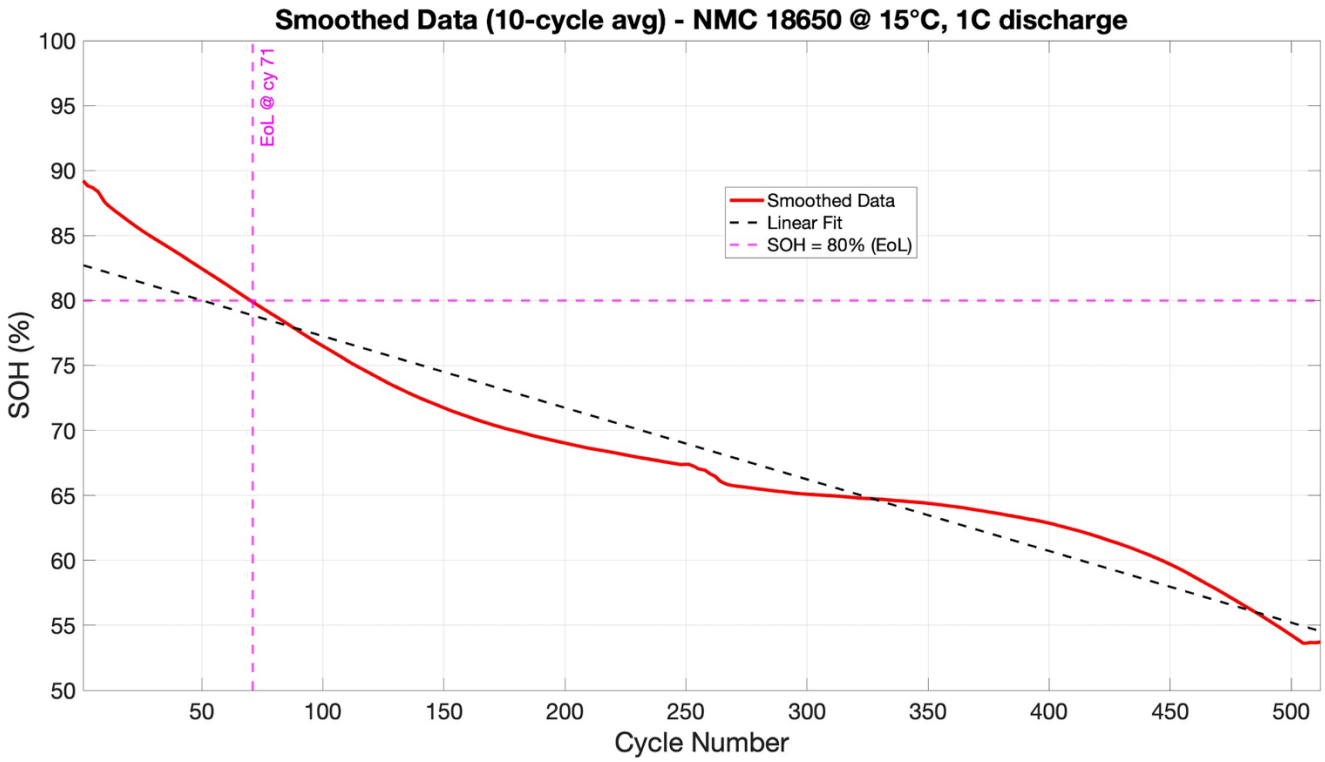

Figure 48 SOH behaviour for NMC chemistry at 15°C.

From the analysis conducted at 25 °C, the following results were obtained:

```
Raw data: 520 | After Filtering: 511 | Removed: 9 outlier
EOL reached in dataset at cycle 459 (SOH_smooth = 79.99%)

========== SOH Analysis Summary ==========
Battery: NMC 18650, Nominal Capacity: 3.00 Ah
Test Conditions: 25°C, 0.5C charge, 1C discharge
Total Cycles Analyzed: 511

Initial SOH:          97.00%
Final SOH:            78.83%
Total Capacity Loss: 18.17%
Degradation Rate:     0.0266 %/cycle
Degradation Rate:     2.658 %/100 cycles

--- EOL (SOH = 80%) ---
EOL source: ACTUAL (observed in smoothed data)
EOL cycle:  459  (SOH_smooth = 79.99%)
```

Figure 49 Outcomes for battery NMC 18650 at 25°C

The battery initially exhibits a state of health of 97.00%, which decreases to 78.83% after 511 cycles. At low temperatures, the cycle degradation of NMC/graphite 18650 cells is significantly accelerated compared with operation at moderate temperatures.

Characterisation studies on commercial NMC and NCA cells by Preger et al. (2024) show that, for NMC chemistry, decreased ambient temperature (from 35 °C to 15 °C) leads to increased capacity fade and more severe materials degradation, largely due to sluggish lithium transport and enhanced lithium plating at the graphite anode. Post-mortem analyses in the same work confirm extensive lithium plating and associated electrode damage at 15°C, whereas cells cycled at 35°C mainly exhibit SEI growth without clear plating signatures [199]. These observations are consistent with the systematic cycle-ageing campaign on NMC and NCA 18650 cells conducted by Wittman et al. (2022), who report a pronounced temperature dependence for NMC cells, with higher degradation rates and earlier knee points at 15°C under 0-100% SOC windows and 0.5C-1C current rates [200].

Taken together, the results of Wittman et al. (2022) and Preger et al. (2024) indicate that, in the 15-35°C range, NMC cells can exhibit shorter cycle life at lower temperatures due to lithium-plating-driven degradation, while operation at moderate temperatures shifts the dominant mechanism towards more gradual SEI-controlled ageing.

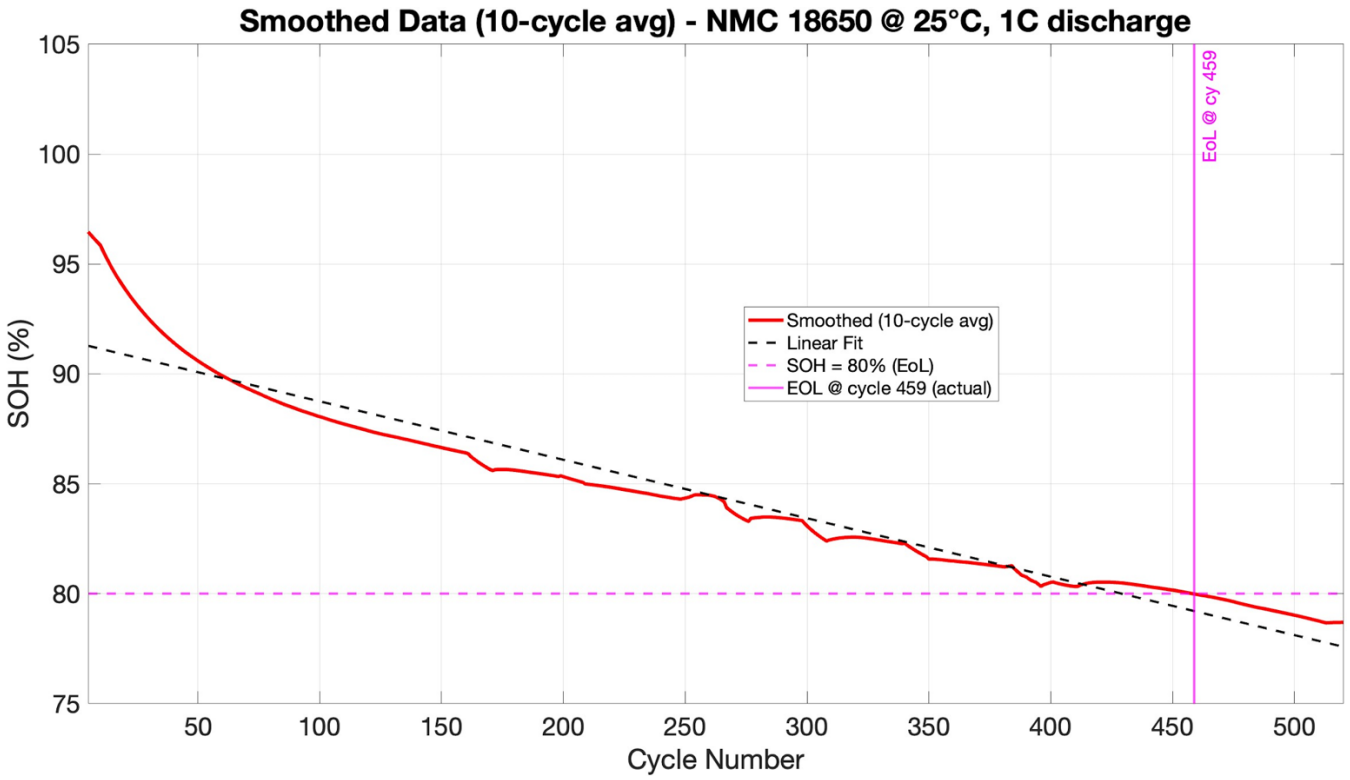

Figure 50 SOH behaviour for NMC chemistry at 25°C.

From the analysis conducted at 35 °C, the following results were obtained:

```
Raw data: 785 | After Filtering: 766 | Removed: 19 outlier
EOL reached in dataset at cycle 504 (SOH_smooth = 79.93%)

========== SOH Analysis Summary ==========
Battery: NMC 18650, Nominal Capacity: 3.00 Ah
Test Conditions: 35°C, 0.5C charge, 1C discharge
Total Cycles Analyzed: 766

Initial SOH:         95.93%
Final SOH:           78.63%
Total Capacity Loss: 17.30%
Degradation Rate:    0.0167 %/cycle
Degradation Rate:    1.672 %/100 cycles

--- EOL (SOH = 80%) ---
EOL source: ACTUAL (observed in smoothed data)
EOL cycle:  504  (SOH_smooth = 79.93%)
```

Figure 51 Outcomes for battery NMC 18650 at 35°C.

Figure 51 shows SOH behaviour over 785 cycles of which only 766 where analysed (due to the filtering action), for a battery starting at a SOH of 95.93% discharged at 35°C. The graphical result can be observed in *Figure 52*.

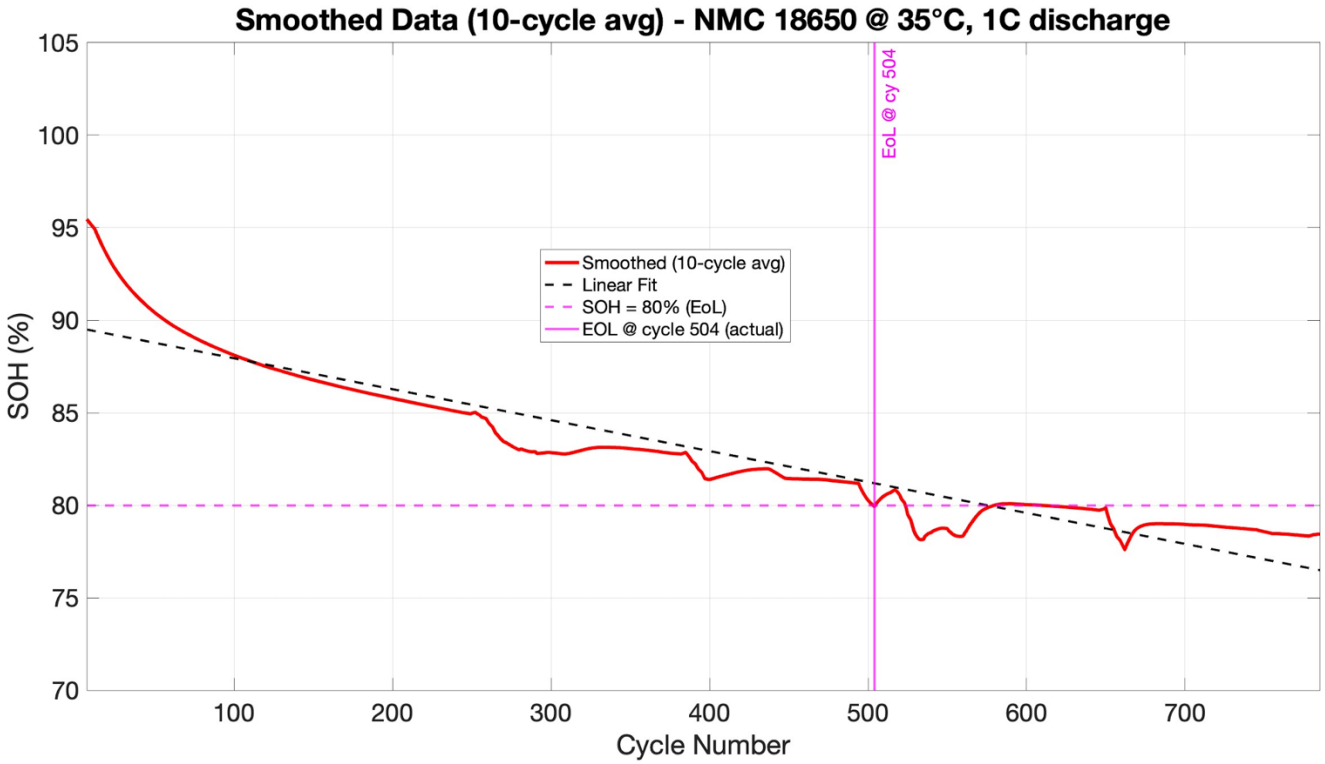

Figure 52 SOH behaviour for NMC chemistry at 35°C.

For the NMC 18650 cell tested at 3C discharge, the SOH analysis shows that the 80% EOL threshold is reached after 70 cycles at 15°C, 390 cycles at 25°C, and 499 cycles at 35°C. Across these conditions, the total capacity loss decreases from 35.63% at 15°C to 18.17% at 25 °C and 17.30% at 35 °C, with the average degradation rate per cycle following the same trend. These results indicate a markedly accelerated ageing at low temperature, while operation at moderate temperature (25-35°C) leads to a slower and more gradual capacity fade. This behaviour is consistent with literature reports for commercial NMC 18650 cells, where lithium-plating-driven degradation dominates at low temperature and is mitigated at moderate temperature in favour of SEI-controlled ageing [200] [201].In summary, the experimental data confirm that, within the investigated range, increasing the operating temperature from 15°C to 35°C significantly extends the cycle life of the NMC 18650 cell under the chosen load profile.

Parameter	15°C	25°C	35°C
Initial SOH (%)	89.90	97.00	95.93
Final SOH (%)	54.27	78.83	78.63
Total Capacity Loss (%)	35.63	18.17	17.30
Slope (% / cycle)	−0.0551	−0.0266	−0.0167
Avg. Degradation Rate (% / cycle)	0.0551	0.0266	0.0167
Avg. Degradation Rate (% / 100 cycles)	5.506	2.658	1.672
Projected EOL @ 80% SOH (cycles)	71	459	504

Table 9 SOH degradation metrics for battery NMC 18650 cells at 15°C, 25°C and 35°C (0.5C charge, 1C discharge). EOL defined at 80% of nominal capacity (3.00 Ah).

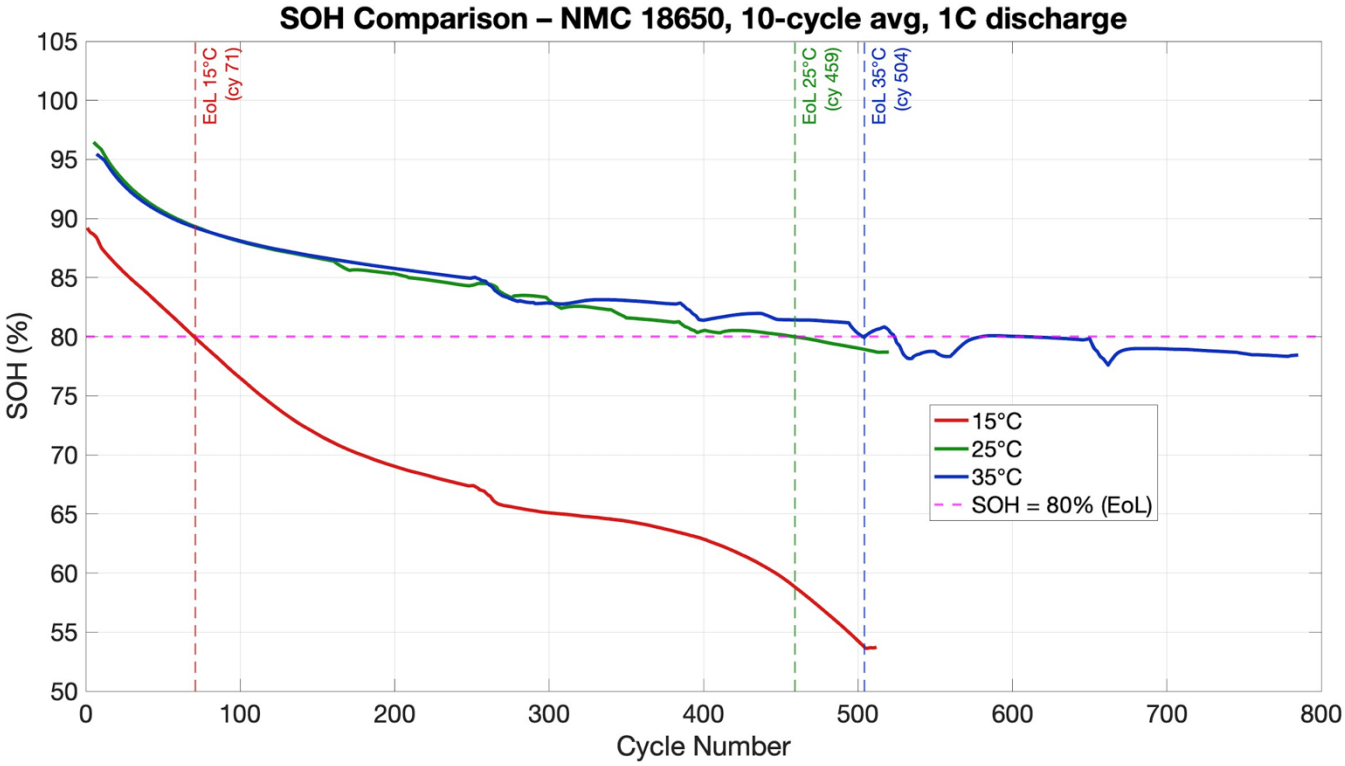

Figure 53 Full view of the three SOH behaviours for NMC chemistry: 15°C, 25°C, 35°C.

The validity of the experimental SOH trends and EOL estimates is confirmed by several independent ageing studies on commercial 18650 NMC and LFP cells reported in the literature. In particular, Preger et al. (2020) and subsequent Sandia datasets for SNL 18650

NMC cells cycled at 0-100% DoD and 0.5C/1C show average lives of approximately 500-550 cycles to 80% capacity at 25-35°C, which is fully consistent with the observed NMC EOL around 500 cycles in this work [198] [200]. The pronounced acceleration of NMC degradation at reduced temperature is also in agreement with systematic studies that report higher fade rates and strong material damage when cycling near 15°C, mainly driven by lithium plating and loss of active material [201] [202]. Conversely, LFP 18650 cells tested under comparable C-rates typically reach several thousand cycles before hitting 80% SOH, with peer-reviewed datasets indicating average lives on the order of 2,000-4,000 cycles at 25°C and even beyond 4,000 cycles at 15°C, in line with the projected EOL between roughly 4,700 and 7,800 cycles obtained here [203]. Overall, the degradation rates, temperature dependence and relative durability of NMC versus LFP derived from the present analysis are therefore consistent with the ranges reported across the available literature, supporting the reliability of the results for further modelling and discussion.

4.4 Future developments and implications for BEVs

The combined analysis of LFP and NMC 18650 cells across 15°C, 25°C and 35°C highlights several practical implications for battery-electric vehicles and points towards clear avenues for future work. For LFP cells, the progressive reduction in projected cycle life from approximately 7,770 cycles at 15°C to 4,755 cycles at 35°C confirms that high operating temperatures markedly accelerate capacity fade, in line with experimental studies on LFP/graphite cells which report significantly faster degradation at elevated temperatures and high SOC windows. This reinforces the need for thermal management strategies that minimise prolonged exposure above about 30-35°C in traction applications. In contrast, the NMC cell shows the opposite trend, with the 80% SOH end-of-life threshold reached after only 71 cycles at 15°C but extended to 459 and 504 cycles at 25°C and 35°C, respectively, indicating that operation at low temperature can be particularly detrimental for this chemistry, most likely due to lithium-plating-driven degradation under high-rate cycling, as also observed in post-mortem studies on commercial NMC/graphite cells [195] [203] [204].

These results suggest that BEV battery management systems should adopt chemistry-specific temperature windows, prioritising moderate temperatures for NMC packs while keeping LFP packs close to ambient and avoiding unnecessary heating, together with temperature-dependent current limits that explicitly account for the different ageing mechanisms, consistent with systematic cycle-ageing investigations on 18650-types of cells.

In practical terms, the temperature-dependent SOH trends observed for LFP and NMC cells have direct implications for the design and operation of BEV battery packs. For LFP-based packs, the strong acceleration of capacity fade at 35°C suggests that the thermal management system should prioritise efficient cooling and restrict prolonged operation at elevated temperatures, especially under high-power driving or fast-charging conditions.

Conversely, for NMC-based packs, the markedly faster degradation at 15°C indicates that very low operating temperatures should be avoided during high-current operation and that active heating may be preferable to ensure operation in a moderate temperature window around 25-35°C. These findings also point to the need for chemistry-specific current derating strategies in the BMS, whereby allowable charge and discharge currents are dynamically adjusted as a function of cell temperature and chemistry, to mitigate lithium plating in NMC cells at low temperature and excessive SEI growth in LFP cells at high temperature. Overall, the results support the adoption of adaptive, chemistry-aware thermal and power management strategies as a key enabler to extend battery lifetime and maintain usable range in future BEV applications.

Conclusions

This master's thesis has evaluated two commercial lithium-ion battery chemistries, LFP and NMC, for battery electric vehicle applications through State-of-Health analysis based on discharge capacity measurements. The LFP chemistry demonstrated superior cycle life, reaching end-of-life (defined at 80% SOH) after 3,000-4,000 cycles under the tested conditions, though effective cooling is essential to mitigate accelerated capacity fade at elevated temperatures (from 0.0018%/cycle at 15°C to 0.0037%/cycle at 35°C). In contrast, NMC cells exhibited the opposite temperature dependence, with markedly higher degradation at low temperatures (0.0551%/cycle at 15°C versus 0.0167%/cycle at 35°C), likely due to lithium plating on the anode, as supported by the experimental data and by literature on similar 18650-format cells. These trends highlight the need for chemistry-specific thermal management: prioritising cooling for LFP packs to avoid excessive SEI growth and electrolyte decomposition at high temperatures, while favouring moderate heating (25-35°C) for NMC to suppress Li-plating risks during high-rate operation. The analysis validates capacity-based SOH estimation as a practical, accurate method for BEV battery management systems, enabling reliable lifetime projections with high coefficients of determination after appropriate data filtering and smoothing. Beyond the comparative assessment of LFP and NMC chemistries, the SOH trends and degradation coefficients extracted from the processed experimental data (including three-sigma outlier rejection and moving-average smoothing) confirm that a simple linear model can reliably capture long-term capacity fade under the tested conditions. These temperature-dependent degradation parameters can be directly embedded into chemistry-aware BMS strategies to guide current limiting and thermal control policies, effectively translating laboratory evidence into operational guidelines for lifetime extension of BEV battery packs. As BEVs emerge as a realistic alternative to hybrid and internal combustion engine vehicles, LFP chemistry appears preferable for longevity in different climates, provided robust cooling is integrated and potentially extending pack life beyond 4,000 cycles while meeting regulatory safety standards.

Ongoing research could extend this framework to hybrid data-driven models incorporating voltage-temperature features for real-time BMS deployment, alongside accelerated testing of larger-format pouch/prismatic cells under WLTP-like duty cycles. Such advancements will further optimise BEV range retention and safety in the transition to widespread electrification.

AI Usage Transparency Statement

During the preparation of this thesis on the ‘State of Health (SOH) Analysis of Automotive Lithium-Ion Battery (LIB) Modules for Battery Electric Vehicles (BEVs): Modelling and Experimental Validation’, I have employed generative artificial intelligence tools as a helpful aid, in keeping with the ethical guidelines of Politecnico di Torino. Specifically, I used Perplexity AI for brainstorming chapter structures and enhancing the readability of certain introductory sections (about 30% of raw text, which was paraphrased and manually revised) and for summarising scientific literature on battery degradation, Electrochemical Impedance Spectroscopy (EIS) (Section 2.1) and verification of my results with online literature; Claude Sonnet 4.6 AI (developed by Anthropic) for generating initial MATLAB code snippets for 3-sigma filtering and discharge data plotting.

All AI outputs were subject to critical review, integration with my original data (thermal tests and capacity fade analysis), and progressive approval by my supervisor, ensuring the core contributions (analysis, modelling, and conclusions) remain entirely my own. Example prompts included: "Generate MATLAB script for SOH calculation from capacity fade with 3-sigma filter on [sample data]" or "Summarise this article on thermal runaway in academic Italian: [DOI]".

Bibliography

[1] Tasneem, O., Tasneem, H., & Xian, X. (2025). Lithium-ion battery technologies for grid-scale renewable energy storage. *Journal of Renewable Energy Storage*.

[2] Suh, J., & Choi, H. (2025). Battery energy storage systems: Energy market review, challenges, and opportunities in frequency control ancillary services.

[3] International Energy Agency. (2024). *Batteries and Secure Energy Transitions* (World Energy Outlook Special Report).

[4] United Nations Department of Economic and Social Affairs. (2021, July 8). *Frontier Technology Issues: Lithium-ion batteries – a pillar for a fossil fuel-free economy?* UN DESA.

[5] Noura, N., Boulon, L., & Jemeï, S. (2020). A review of battery state of health estimation methods: Hybrid electric vehicle challenges. *World Electric Vehicle Journal*, *11*(4), 66.

[6] Council of the European Union. (2025, September 19). *Accordo di Parigi sui cambiamenti climatici*.

[7] Petrone, A. (2025, July 11). Boom delle rinnovabili nel mondo, ma il divario regionale si allarga.

[8] Seminario-Morales, M. V., Sánchez-Prieto, M. G., Cuba Carbajal, N., Chenet Zuta, M. E., & Huamán-Romaní, Y. L. (2024). Smart demand management based on economic and technical objective functions in the autonomous energy system. *Journal of Engineering Research*, *12*(4), 859-866.

[9] Ringler, C., Bhaduri, A., & Lawford, R. (2013). The nexus across water, energy, land and food (WELF): Potential for improved resource use efficiency? *Current Opinion in Environmental Sustainability*, *5*(6), 617-624.

[10] Griggs, D., Stafford-Smith, M., Gaffney, O., Rockström, J., Öhman, M. C., Shyamsundar, P., Steffen, W., Glaser, G., Kanie, N., & Noble, I. (2013). Sustainable development goals for people and planet. *Nature*, *495*, 305-307.

[11] Nikolaos, P. C., Marios, F., & Dimitris, K. (2023). A review of pumped hydro storage systems. *Energies*, *16*(11), 4516.

[12] Rastler, D. (2010). *Electricity energy storage technology options: A white paper primer on applications, costs and benefits* (EPRI Report). Electric Power Research Institute.

[13] International Energy Agency (2020). *Innovation in Batteries and Electricity Storage*.

[14] Gomstyn, A., & Jonker, A. (2024, December 3). Che cos'è lo stoccaggio dell'energia? *IBM Think*.

[15] GivEnergy. (2024, January 30). What is round trip efficiency in battery storage? *GivEnergy Blog*.

[16] Flynn, M. M., McMullen, P., & Solis, O. (2009). Saving energy using flywheels. *IEEE Industry Applications Magazine*, *14*(6), 69-76.

[17] Das, H. S., Tan, C. W., & Yatim, A. H. M. (2017). Fuel cell hybrid electric vehicles: A review on power conditioning units and topologies. *Renewable and Sustainable Energy Reviews*, *76*, 268-291.

[18] Rabi, A. M., Radulovic, J., & Buick, J. M. (2023). Comprehensive review of compressed air energy storage (CAES) technologies. *Thermo*, *3*(1), 104-126.

[19] Mitali, J., Dhinakaran, S., & Mohamad, A. A. (2022). Energy storage systems: A review. *Energy Storage and Saving*, *1*(3), 166-216.

[20] Thomason, H. E., & Thomason, H. J. L. (1979, June 19). *Heat and cold storage apparatus* (U.S. Patent No. 4,158,358). U.S. Patent and Trademark Office.

[21] Reddy, K. S., Mudgal, V., & Mallick, T. K. (2018). Review of latent heat thermal energy storage for improved material stability and effective load management. *Journal of Energy Storage*, *15*, 205-227.

[22] Mohamad, A., Che Sidik, N. A., & Beriache, M. (2019). Thermo physical enhancement of advanced nano-composite phase change material.

[23] Isamotu, O., Musa, N., Aluko, J., & Oriaifo, M. (2020). Eutectic composition of selected phase change materials for thermal energy storage applications. *FUOYE Journal of Engineering and Technology*.

[24] The Editors of Encyclopaedia Britannica. (2025, September 2). Capacitor. *Encyclopaedia Britannica*.

[25] NextPCB. Capacitor symbols: A guide to understanding capacitors in electronics. *NextPCB Blog*.

[26] EE Power. Supercapacitor. *EE Power Capacitor Guide*.

[27] Ligna Energy. What is a supercapacitor?

[28] UTMEL. (2020, March 3). An overview of supercapacitors.

[29] Pandey, A., Rawat, K., Phogat, P., Shreya, Jha, R., & Singh, S. (2025). Next-generation energy storage: A deep dive into experimental and emerging battery technologies. *Journal of Alloys and Compounds*, *1014*.

[30] Poullikkas, A. (2013). A comparative overview of large-scale battery systems for electricity storage. *Renewable and Sustainable Energy Reviews*, *27*, 778-788.

[31] ICAPE Group. Battery types: The comprehensive guide.

[32] Wang, Y., Yu, T., Chen, J., Gao, B., Yu, M., & Zhu, J. (2025). *Advances in safety of lithium-ion batteries for energy storage: Hazard characteristics and active suppression techniques*. Energy Reviews, 4(1).

[33] Nguyen, T. T., Demortière, A., Fleutot, B., Delobel, B., Delacourt, C., & Cooper, S. J. (2023). Safety perceptions of solid-state lithium metal batteries. *Sustainable Energy & Fuels, 7*(11), 2576–2596.

[34] Chiavazzo, E. (2023). *Energy Storage* (Course 01TVHXY, 01TVHND) [Lecture slides]. Politecnico di Torino.

[35] International Renewable Energy Agency. (2017). *Electricity storage and renewables: Costs and markets to 2030*. Abu Dhabi: International Renewable Energy Agency (IRENA).

[36] InnoEnergy Scandinavia, Frost & Sullivan, Skeleton Technologies, & NAWA Technologies. (2020, October). *Unlocking new possibilities through innovative energy storage: The role of ultracapacitors in the energy transition*. EIT InnoEnergy.

[37] DrPress. (2025). Comparative study of supercapacitor, battery and more. *HSET*.

[38] Mahadevan, V., Raja, S. S., Rusho, M. A., & Yishak, S. (2025). Critical review of energy storage systems: A comparative assessment of mechanisms, advantages, challenges, and integration with renewable energy. *Results in Engineering*, *26*.

[39] Mishra, V., Kumar, A., Singh, R., Sharma, P., & Gupta, S. (2025). Integration of supercapacitor and flywheel along with battery for high-performance hybrid energy storage system. *Journal of Electrical Systems*, *21*(01), 138-149.

[40] Jaradat, T., & Khatib, T. (2025). A review of battery energy storage system for renewable energy penetration in electrical power system: Environmental impact, sizing methods, market features, and policy frameworks. *Future Batteries*, *7*.

[41] Abdelkareem, M. A., Ayoub, M., Khuri, S., Alami, A. H., Sayed, E. T., Deepa, T. D., & Olabi, A. G. (2023). Environmental aspects of batteries. *Sustainable Horizons*, *8*.

[42] Krebs, L., Frischknecht, R., Stolz, P., & Sinha, P. (2020). *Environmental life cycle assessment of residential PV and battery storage systems* (IEA PVPS Task 12 Report T12-17:2020). International Energy Agency Photovoltaic Power Systems Programme.

[43] Du, Y., Pei, W., Hao, Y., Zhang, P., Wang, C., Yang, Y., & Zhang, L. (2025). Life cycle assessment of the pumped hydro energy storage system in China. *Energy*, *331*.

[44] Zhang, C., Jing, J., Yun, L., Zheng, Y., & Huang, H. (2022). A cradle-to-grave life cycle assessment of high-voltage aluminum electrolytic capacitors in China. *Journal of Cleaner Production*, *370*.

[45] Li, X., & Palazzolo, A. (2022). A review of flywheel energy storage systems: State of the art and opportunities. *Journal of Energy Storage*, *46*.
[46] De Angelis, P. (2023). *Energy Storage* (Course 01TVHXY, 01TVHND) – Introduction to Batteries Modelling [Lecture slides]. Politecnico di Torino.
[47] Njema, J. M., Ngari, E. W., & Muriithi, N. J. (2024). A review on the recent advances in battery development and energy storage technologies. *Journal of Renewable Energy*, *2024*, Article 2329261.
[48] Santarelli, M. (2024). *Polygeneration and advanced energy systems* (Course 01QGXND) [Lecture slides]. Politecnico di Torino.
[49] Zhao, G., Wang, X., & Negnevitsky, M. (2022). Connecting battery technologies for electric vehicles from battery materials to management. *iScience*, *25*(2).
[50] Akter, S., Badhon, N. M., Mohammad, D., Abid, M., Shahazi, R., Uddin, M. R., & Alam, M. M. (2025). The future of lithium-ion batteries: Innovations, challenges, and prospects for a sustainable energy transition. *Lithium Battery Engineering and Science*, *1*(1), 2029.
[51] Heiskanen, S. K., Kim, J., & Lucht, B. L. (2019). Generation and evolution of the solid electrolyte interphase of lithium-ion batteries. *Joule*, *3*(10), 2322-2333.
[52] Seo, G., Ha, J., Kim, M., Park, J., Lee, J., Park, E., Bong, S., Lee, K., Kwon, S. J., Moon, S., Choi, J., & Lee, J. (2022). Rapid determination of lithium-ion battery degradation: High C-rate LAM and calculated limiting LLI. *Journal of Energy Chemistry, 67*, 663–671.
[53] Nazeeruddin, M. A., Li, R., O'Kane, S. E. J., Marinescu, M., & Offer, G. J. (2025). Lithium-ion battery degradation: Introducing the concept of reservoirs to design for lifetime. *arXiv*. Advance online publication.
[54] Wu, Z., Wang, H., & Zhang, Y. (2025). Mechanism-traced diagnosis of lithium inventory loss for lithium-ion batteries using physics-driven machine learning. *Energy, 338*, 138936.
[55] Juarez-Robles, D., Vyas, A. A., Fear, C., Jeevarajan, J. A., & Mukherjee, P. P. (2020). Overcharge and aging analytics of Li-ion cells. *Journal of the Electrochemical Society*, *167*(9), 090547.
[56] Che, Y., Zheng, Y., Forest, F. E., Sui, X., Hu, X., & Teodorescu, R. (2024). Predictive health assessment for lithium-ion batteries with probabilistic degradation prediction and accelerating aging detection. *Reliability Engineering & System Safety*, *241*, 109603.
[57] Koleti, U. R., Rajan, A., Tan, C., Moharana, S., Dinh, T. Q., & Marco, J. (2020). A study on the influence of lithium plating on battery degradation. *Energies*, *13*(13), 3458.

[58] Ando, K., Matsuda, T., Miwa, T., Kawai, M., & Imamura, D. (2023). Degradation mechanism of all-solid-state lithium-ion batteries with argyrodite $Li_{7-x}PS_{6-x}Cl_x$ sulfide through high-temperature cycling test. *Battery Energy*.

[59] Xiong, R., Pan, Y., Shen, W., Li, H., & Sun, F. (2020). Lithium-ion battery aging mechanisms and diagnosis method for automotive applications: Recent advances and perspectives. *Renewable and Sustainable Energy Reviews*, *131*.

[60] Janakiraman, U., Garrick, T., & Fathima, J. (2020). Review—Lithium plating detection methods in Li-ion batteries. *Journal of the Electrochemical Society*, *167*(16), 160552.

[61] Zhang, G., Wei, X., Han, G., Dai, H., Zhu, J., Wang, X., Tang, X., & Ye, J. (2021). Lithium plating on the anode for lithium-ion batteries during long-term low temperature cycling. *Journal of Power Sources*, *484*.

[62] Siczek, K. J. (2019). Negative electrode (anode) materials. In *Next-generation batteries with sulfur cathodes*. Elsevier.

[63] Diallo, M. S., Shi, T., Zhang, Y., Dalavi, S., Schreiber, N. J., McDowell, M. T., Monroe, C. W., & Janek, J. (2024). Effect of solid-electrolyte pellet density on failure of solid-state batteries. *Nature Communications*, *15*, 858.

[64] Luo, H., Cai, T., Yuan, A., & He, S. (2024). Research on the early warning method of thermal runaway of lithium battery based on strain detection of explosion-proof valve. In *Lecture Notes in Electrical Engineering* (pp. 602–614).

[65] Luo, H., Cai, T., Yuan, A., & He, S. (2024). Research on the early warning method of thermal runaway of lithium battery based on strain detection of explosion-proof valve. In Q. Yang, Z. Li, & A. Luo (Eds.), *The proceedings of the 18th Annual Conference of China Electrotechnical Society (ACCES 2023)* (Lecture Notes in Electrical Engineering, Vol. 1167, pp. 602–614). Springer, Singapore.

[66] Wang, H., & Whitacre, J. F. (2021). Inhomogeneous aging of cathode materials in commercial 18650 lithium-ion battery cells. *Journal of Energy Storage*, *35*.

[67] Gao, X., Ikuhara, Y. H., Fisher, C. A. J., Huang, R., Kuwabara, A., Moriwake, H., Kohama, K., & Ikuhara, Y. (2019). Oxygen loss and surface degradation during electrochemical cycling of lithium-ion battery cathode material $LiMn_2O_4$. *Journal of Materials Chemistry A*, *7*, 8845-8854.

[68] Zhao, X., Li, H., Han, F., Dai, M., Sun, Y., Song, Z., Han, D., & Niu, L. (2020). Electrochemical exfoliation of graphene as an anode material for ultra-long cycle lithium-ion batteries. *Journal of Physics and Chemistry of Solids*, *139*, 109301.

[69] Asenbauer, J., Eisenmann, T., Kuenzel, M., Kazzazi, A., Chen, Z., & Bresser, D. (2020). The success story of graphite as a lithium-ion anode material – fundamentals, remaining challenges, and recent developments including silicon (oxide) composites. *Sustainable Energy & Fuels*, *4*(11), 5387-5416.

[70] Barré, A., Deguilhem, B., Grolleau, S., Gérard, M., Suard, F., & Riu, D. (2013). A review on lithium-ion battery ageing mechanisms and estimation for automotive applications. *Journal of Power Sources*, *241*, 680-689.

[71] Roy, P. K., Shahjalal, M., Shams, T., Fly, A., Stoyanov, S., Ahsan, M., & Haider, J. (2023). A critical review on battery aging and state estimation technologies of lithium-ion batteries: Prospects and issues. *Electronics*, *12*(19), 4105.

[72] Li, W. (2020). Review—An unpredictable hazard in lithium-ion batteries from transition metal ions: Dissolution from cathodes, deposition on anodes and elimination strategies. *Journal of the Electrochemical Society*, *167*, 090514.

[73] Rodríguez, R. A., González Montiel, M., Mohallem, N. D. S., Laffita, Y. M., Montoro, L. A., Santos, M. A., Ramírez, H. L., & Pérez-Cappe, E. L. (2021). The role of defects on the Jahn-Teller effect and electrochemical charge storage in nanometric $LiMn_2O_4$ material. *Solid State Ionics*, *369*, 115707.

[74] Liao, X., Huang, Q., Mai, S., Wang, X., Xu, M., Xing, L., Liao, Y., & Li, W. (2015). Understanding self-discharge mechanism of layered nickel cobalt manganese oxide at high potential. *Journal of Power Sources*, *286*, 551-556.

[75] Hunter, J. C. (1981). Preparation of a new crystal form of manganese dioxide: λ-MnO_2. *Journal of Solid-State Chemistry*, *39*(2), 142-147.

[76] Huang, D., Engtrakul, C., Nanayakkara, S., Mulder, D. W., Han, S. D., Zhou, M., Luo, H., & Tenent, R. C. (2021). Understanding degradation at the lithium-ion battery cathode/electrolyte interface: Connecting transition-metal dissolution mechanisms to electrolyte additives. *ACS Applied Materials & Interfaces*, *13*(10), 11930-11939.

[77] Lucu, M., Martinez-Laserna, E., Gandiaga, I., Liu, K., Camblong, H., Widanage, W. D., & Marco, J. (2020). Data-driven nonparametric Li-ion battery ageing model aiming at learning from real operation data - Part B: Cycling operation. *Journal of Energy Storage*, *30*, 101410.

[78] Serhan, M., Sprowls, M., Jackemeyer, D., Long, M., Perez, I. D., Maret, W., Chen, W., Liptak, M., & Forzani, E. (2019). Total iron measurement in human serum with a smartphone. *AIChE Annual Meeting Conference Proceedings*, *2019-November*, 1-20.

[79] Pinson, M. B., & Bazant, M. Z. (2012). Theory of SEI formation in rechargeable batteries: Capacity fade, accelerated aging and lifetime prediction. *arXiv preprint arXiv: 1210.3672*.

[81] Xu, J., Deshpande, R. D., Pan, J., Cheng, Y. T., & Battaglia, V. S. (2015). Electrode side reactions, capacity loss and mechanical degradation in lithium-ion batteries. *Journal of the Electrochemical Society*, *162*(10), A2026-A2035.

[82] Wood, S. M., Fang, C., Dufek, E. J., Nagpure, S. C., Sazhin, S. V., Liaw, B., & Meng, Y. S. (2018). Predicting calendar aging in lithium metal secondary batteries: The impacts of solid electrolyte interphase composition and stability. *Advanced Energy Materials*, *8*(26), 1801427.

[83] Fermín-Cueto, P., McTurk, E., Allerhand, M., Medina-Lopez, E., Anjos, M. F., Sylvester, J., & Dos Reis, G. (2020). Identification and machine learning prediction of knee-point and knee-onset in capacity degradation curves of lithium-ion cells. *Energy and AI*, *1*, 100006.

[84] Aris, A. M., & Shabani, B. (2017). An experimental study of a lithium-ion cell operation at low temperature conditions. *Energy Procedia*, *110*, 128-135.

[85] Kalaga, K., Rodrigues, M. T. F., Trask, S. E., Shkrob, I. A., & Abraham, D. P. (2018). Calendar-life versus cycle-life aging of lithium-ion cells with silicon-graphite composite electrodes. *Electrochimica Acta*, *280*, 221-228.

[86] Yang, B., Zhang, H., Yu, L., Fan, W., & Huang, D. (2016). Lithium difluorophosphate as an additive to improve the low temperature performance of LiNi0 5Co0 2Mn0 3O2/graphite cells. *Electrochimica Acta*, *221*, 107-114.

[87] Gao, F., & Tang, Z. (2008). Kinetic behavior of $LiFePO_4$/C cathode material for lithium-ion batteries. *Electrochimica Acta*, *53*(15), 5071-5075.

[88] Almeida, C. S. (2016). Analysis of the co-dispersion structure of health-related indicators, the center of the subject's sense of health, and the elderly people living at home. *Revista Brasileira de Linguística Aplicada*, *5*, 1689-1699.

[89] Röder, P., Stiaszny, B., Ziegler, J. C., Baba, N., Lagaly, P., & Wiemhöfer, H. D. (2014). The impact of calendar aging on the thermal stability of a $LiMn_2O_4$–Li(Ni1/3Mn1/3Co1/3)O2/graphite lithium-ion cell. *Journal of Power Sources*, *268*, 315-325.

[90] Rahman, T., & Alharbi, T. (2024). Exploring lithium-ion battery degradation: A concise review of critical factors, impacts, data-driven degradation estimation techniques, and sustainable directions for energy storage systems. *Batteries*, *10*(7), 220.

[91] Lamb, J., & Orendorff, C. J. (2014). Evaluation of mechanical abuse techniques in lithium-ion batteries. *Journal of Power Sources*, *247*, 189-196.

[91] Kim, G. H., Pesaran, A., & Spotnitz, R. (2007). A three-dimensional thermal abuse model for lithium-ion cells. *Journal of Power Sources*, *170*(2), 476-489.

[92] Chen, Y., Kang, Y., Zhao, Y., Wang, L., Liu, J., Li, Y., Liang, Z., He, X., Li, X., Tavajohi, N., & Li, B. (2021). A review of lithium-ion battery safety concerns: The issues, strategies, and testing standards. *Journal of Energy Chemistry*, *59*, 83-99.

[93] Wandt, J., Freiberg, A., Thomas, R., Gorlin, Y., Siebel, A., Jung, R., Gasteiger, H. A., & Tromp, M. (2016). Singlet oxygen evolution from layered transition metal oxide cathode materials and its implications for lithium-ion batteries. *Journal of Materials Chemistry A*, *4*.

[94] Wang, J., Hu, Z., Yin, X., Li, Y., Huo, H., Zhou, J., & Li, L. (2015). Alumina/phenolphthalein polyetherketone ceramic composite polypropylene separator film for lithium-ion power batteries. *Electrochimica Acta*, *159*, 61-65.

[95] Ren, D., Feng, X., Lu, L., Ouyang, M., Zheng, S., Li, J., & He, X. (2017). An electrochemical-thermal coupled overcharge-to-thermal-runaway model for lithium-ion battery. *Journal of Power Sources*, *364*, 328-340.

[96] Kim, S. H., Choi, K. H., Cho, S. J., Park, J. S., Cho, K. Y., Lee, C. K., Shim, S. B., & Lee, S. Y. (2014). A shape-deformable and thermally stable solid-state electrolyte based on a plastic crystal composite polymer electrolyte for flexible/safer lithium-ion batteries. *Journal of Materials Chemistry A*, *2*(28), 10854-10861.

[97] Liu, B., Jia, Y., Yuan, C., Wang, L., Gao, X., Yin, S., & Xu, J. (2020). Safety issues and mechanisms of lithium-ion battery cell upon mechanical abusive loading: A review. *Energy Storage Materials*, *24*, 85-112.

[98] Sahraei, E., Meier, J., & Wierzbicki, T. (2014). Characterizing and modeling mechanical properties and onset of short circuit for three types of lithium-ion pouch cells. *Journal of Power Sources*, *247*, 503-516.

[99] Zhang, X., & Wierzbicki, T. (2015). Characterization of plasticity and fracture of shell casing of lithium-ion cylindrical battery. *Journal of Power Sources*, *280*, 47-56.

[100] Xiao, Y., Zhang, H., Wang, J., Liu, X., & Chen, L. (2023). Review of mechanical abuse related thermal runaway of lithium-ion batteries. *Renewable and Sustainable Energy Reviews, 187*, 113717.

[101] Finegan, D. P., Scheel, M., Robinson, J. B., Tjaden, B., Hunt, I., Mason, T. J., Millichamp, J., Di Michiel, M., Offer, G. J., Hinds, G., Brett, D. J. L., & Shearing, P. R.

(2015). In-operando high-speed tomography of lithium-ion batteries during thermal runaway. *Nature Communications*, *6*, 6924.

[102] Arai, J., Okada, Y., Sugiyama, T., Izuka, M., Gotoh, K., & Takeda, K. (2015). In situ solid state ^{7}Li NMR observations of lithium metal deposition during overcharge in lithium-ion batteries. *Journal of the Electrochemical Society*, *162*(6), A952.

[103] Lisbona, D., & Snee, T. (2011). A review of hazards associated with primary lithium and lithium-ion batteries. *Process Safety and Environmental Protection*, *89*(6), 434-442.

[104] Li, H. F., Gao, J. K., & Zhang, S. L. (2008). Effect of overdischarge on swelling and recharge performance of lithium-ion cells. *Chinese Journal of Chemistry*, *26*(9), 1585-1588.

[105] Larsson, F., & Mellander, B. E. (2014). Abuse by external heating, overcharge and short circuiting of commercial lithium-ion battery cells. *Journal of the Electrochemical Society*, *161*(10), A1611.

[106] Guo, G., Long, B., Cheng, B., Zhou, S., Xu, P., & Cao, B. (2010). Three-dimensional thermal finite element modeling of lithium-ion battery in thermal abuse application. *Journal of Power Sources*, *195*(8), 2393-2398.

[107] Chen, Y., Kang, Y., Zhao, Y., Wang, L., Liu, J., Li, Y., Liang, Z., He, X., Li, X., Tavajohi, N., & Li, B. (2021). A review of lithium-ion battery safety concerns: The issues, strategies, and testing standards. *Journal of Energy Chemistry*, *59*, 83-99.

[108] Maleki, H., Deng, G., Anani, A., & Howard, J. (1999). Thermal stability studies of Li-ion cells and components. *Journal of the Electrochemical Society*, *146*(9), 3224-3229.

[109] Wang, H., Du, Z., Rui, X., Wang, S., Jin, C., He, L., Zhang, J., Wen, D., Zhang, C., & Feng, X. (2020). A comparative analysis on thermal runaway behavior of Li ($Ni_xCo_\gamma Mn_u$) O_2 battery with different nickel contents at cell and module level. *Journal of Hazardous Materials*, *393*, 122361.

[110] Mehne, J., & Nowak, W. (2017). Improving temperature predictions for Li-ion batteries: Data assimilation with a stochastic extension of a physically based, thermo-electrochemical model. *Journal of Energy Storage*, *12*, 288-296.

[111] Yu, X., Chen, R., Gan, L., Li, H., & Chen, L. (2023). Battery safety: From lithium-ion to solid-state batteries. *Engineering*, *21*, 9-14.

[112] Shahid, S., & Agelin-Chaab, M. (2022). A review of thermal runaway prevention and mitigation strategies for lithium-ion batteries. *Energy Conversion and Management: X*, *16*, 100310.

[113] International Electrotechnical Commission. (2017). *IEC 61851-1: Electric vehicle conductive charging system – Part 1: General requirements* (3rd ed.).

[114] Alsharif, A., Tan, C. W., Ayop, R., Dobi, A., & Lau, K. Y. (2021). A comprehensive review of energy management strategy in vehicle-to-grid technology integrated with renewable energy sources. *Sustainable Energy Technologies and Assessments*, *47*, 101439.
[115] ACTE Technologies. (2025). Hybrid electric vehicles: Explained clearly | Updated 2025.
[116] Ali, Z. M., Calasan, M., Gandoman, F. H., Jurado, F., & Abdel Aleem, S. H. E. (2024). Review of batteries reliability in electric vehicle and E-mobility applications. *Ain Shams Engineering Journal*, *15*(2), 102442.
[117] Zhang, X., Mi, C. C., & Yin, C. (2014). Active-charging based powertrain control in series hybrid electric vehicles for efficiency improvement and battery lifetime extension. *Journal of Power Sources*, *245*, 292-300.
[118] Sivertsson, M., & Eriksson, L. (2017). Optimal powertrain lock-up transients for a heavy-duty series hybrid electric vehicle. *IFAC-PapersOnLine*, *50*(1), 7842-7848.
[119] Zhao, C., Zu, B., Xu, Y., Wang, Z., Zhou, J., & Liu, L. (2020). Design and analysis of an engine-start control strategy for a single-shaft parallel hybrid electric vehicle. *Energy*, *202*, 117621.
[120] Wang, Y., Wu, Z., Chen, Y., Xia, A., Guo, C., & Tang, Z. (2018). Research on energy optimization control strategy of the hybrid electric vehicle based on Pontryagin's minimum principle. *Computers & Electrical Engineering*, *72*, 203-213.
[121] Liu, J., & Peng, H. (2008). Modeling and control of a power-split hybrid vehicle. *IEEE Transactions on Control Systems Technology*, *16*(6), 1247-1251.
[122] Waraich, R. A., Galus, M. D., Dobler, C., Balmer, M., Andersson, G., & Axhausen, K. W. (2013). Plug-in hybrid electric vehicles and smart grids: Investigations based on a microsimulation. *Transportation Research Part C: Emerging Technologies*, *28*, 74-86.
[123] Green, R. C., Wang, L., & Alam, M. (2010). The impact of plug-in hybrid electric vehicles on distribution networks: A review and outlook. In *IEEE PES General Meeting* (pp. 1-8).
[124] Hertzke, P., Müller, N., Schenk, S., & Wu, T. (2018). The global electric-vehicle market is amped up and on the rise. *McKinsey Center for Future Mobility*, *1*, 1-8.
[125] Ritchie, H. (2024). Tracking global data on electric vehicles. *Our World in Data*.
[126] Li, W., Long, R., Chen, H., & Geng, J. (2017). A review of factors influencing consumer intentions to adopt battery electric vehicles. *Renewable and Sustainable Energy Reviews*, *78*, 318-328.

[127] Mishra, S., Verma, S., Chowdhury, S., Gaur, A., Mohapatra, S., Dwivedi, G., & Verma, P. (2021). A comprehensive review on developments in electric vehicle charging station infrastructure and present scenario of India. *Sustainability*, *13*(4), 2396.

[128] Ashkrof, P., de Almeida Correia, G. H., & Van Arem, B. (2020). Analysis of the effect of charging needs on battery electric vehicle drivers' route choice behaviour: A case study in the Netherlands. *Transportation Research Part D: Transport and Environment*, *78*, 102206.

[129] Lyu, Y., Siddique, A. R. M., Majid, S. H., Biglarbegian, M., Gadsden, S. A., & Mahmud, S. (2019). Electric vehicle battery thermal management system with thermoelectric cooling. *Energy Reports*, *5*, 822-827.

[130] Offer, G. J., Howey, D., Contestabile, M., Clague, R., & Brandon, N. P. (2010). Comparative analysis of battery electric, hydrogen fuel cell and hybrid vehicles in a future sustainable road transport system. *Energy policy*, *38*(1), 24-29.

[131] El Fadil, H., Giri, F., Guerrero, J. M., & Tahri, A. (2014). Modeling and nonlinear control of a fuel cell/supercapacitor hybrid energy storage system for electric vehicles. *IEEE Transactions on Vehicular Technology*, *63*(7), 3011-3018.

[132] Song, K., Li, F., Hu, X., He, L., Niu, W., Lu, S., & Zhang, T. (2018). Multi-mode energy management strategy for fuel cell electric vehicles based on driving pattern identification using learning vector quantization neural network algorithm. *Journal of Power Sources*, *389*, 230-239.

[133] Nassif, G. G., & de Almeida, S. C. (2020). Impact of powertrain hybridization on the performance and costs of a fuel cell electric vehicle. *International Journal of Hydrogen Energy*, *45*(41), 21722-21737.

[134] Verma, S., Mishra, S., Gaur, A., Chowdhury, S., Mohapatra, S., Dwivedi, G., & Verma, P. (2021). A comprehensive review on energy storage in hybrid electric vehicle. *Journal of Traffic and Transportation Engineering (English Edition), 8*(5), 621–637.

[135] Remarkable Cars. (n.d.). *Hybrid information*. Retrieved February 10, 2026, from https://www.remarkablecars.nz/hybrid-information .

[136] United Nations Economic Commission for Europe. (2022). *Uniform provisions concerning the approval of vehicles with regard to specific requirements for the electric power train (UN Regulation No. 100, Revision 3)*.

[137] National Highway Traffic Safety Administration. (2024, December 20). *Federal Motor Vehicle Safety Standards; FMVSS No. 305a Electric-Powered Vehicles: Electric*

Powertrain Integrity Global Technical Regulation No. 20 Incorporation by Reference (Docket No. NHTSA–2024–0091; RIN 2127–AM43). Federal Register, 89(245), 104318–104462.

[138] Standardization Administraion of China. (2025). *GB 38031-2025: Electric vehicles traction battery safety requirements*. State Administration for Market Regulation; Standardization Administration of China.

[139] Hildebrand, S., Eddarir, A., & Lebedeva, N. (2024). *Overview of battery safety tests in standards for stationary battery energy storage systems* (JRC Technical Report, EUR 31823 EN). Publications Office of the European Union.

[140] Vaielettrico. (2025, January). *Batterie cinesi: ecco lo standard di sicurezza più severo di sempre*.

[141] In Compliance Magazine. (2024). Testing to UNECE Regulation 100 requirements for electric vehicle batteries. *In Compliance Magazine*.

[142] Atomfair. (2025). *Battery safety standards for electric vehicles*. Atomfair Battery Primer.

[143] National Highway Traffic Safety Administration. (2024). *Federal Motor Vehicle Safety Standards; FMVSS No. 305a Electric-Powered Vehicles: Electric Powertrain Integrity Global Technical Regulation No. 20, Incorporation by Reference* (Notice of proposed rulemaking, Docket No. NHTSA–2024–0012).

[144] InterRegs. (2025). Significant amendments to UN ECE Regulation No. 100 on vehicles with an electric powertrain adopted.

[145] European Parliament, & Council of the European Union. (2019). *Regulation (EU) 2019/631 of 17 April 2019 setting CO_2 emission performance standards for new passenger cars and for new light commercial vehicles, and repealing Regulations (EC) No 443/2009 and (EU) No 510/2011* (Text with EEA relevance). Official Journal of the European Union, L 111, 13–53.

[146] European Commission. (2023). *Commission Regulation (EU) 2023/443 of 8 February 2023 amending Regulation (EU) 2017/1151 as regards the emission type-approval procedures for light passenger and commercial vehicles* (Text with EEA relevance). Official Journal of the European Union, L 66, 1–63.

[147] United Nations Economic Commission for Europe. (2014, March 14). *UNECE adopts more accurate fuel efficiency and CO_2 test for new cars (WLTP).*

[148] The Mobility House. (n.d.). *WLTP for electric cars:*

The new test procedure for range and energy consumption. Retrieved February 10, 2026, from: https://www.mobilityhouse.com/int_en/knowledge-center/article/wltp-for-electric-car-new-test-procedure

[149] Transport & Environment. (2026, January). *Position paper on the revision of the EU car CO_2 standards.*

[150] Dornoff, J., Mock, P., Baldino, C., Bieker, G., Díaz, S., Miller, J., Sen, A., Tietge, U., & Wappelhorst, S. (2021). *Fit for 55: A review and evaluation of the European Commission proposal for amending the CO_2 targets for new cars and vans* (ICCT Briefing, September 2021). International Council on Clean Transportation.

[151] European Alternative Fuels Observatory. (2018). *Glossary: NEDC (New European Driving Cycle)*.

[152] Environmental Protection Agency. (2024). 40 C.F.R. § 86.1865-12 – How to comply with the fleet average CO_2 standards. *Electronic Code of Federal Regulations*.

[153] Gowri Sankar, P. A., Shanmuga Priya, S. R., Karthikumar, K., & Suba, S. (2025). Electric vehicle battery management system: A comprehensive review. In *Proceedings of the 1st International Conference on Research and Development in Information, Communication, and Computing Technologies (ICRDICCT '25)* (pp. 402–412). SciTePress.

[154] Li, M., Xu, W., Zhang, S., Liu, L., Hussain, A., Hu, E., Zhang, J., Mao, Z., & Chen, Z. (2025). State of health estimation and battery management: A review of health indicators, models and machine learning. *Materials, 18*(1), 145.

[155] Wang, Y., Tian, J., Sun, Z., Wang, L., Xu, R., Li, M., & Chen, Z. (2020). A comprehensive review of battery modeling and state estimation approaches for advanced battery management systems. *Renewable and Sustainable Energy Reviews, 131*, Article 110015.

[156] Sarmiento Maldonado, H. O. *SoC Estimation for Lithium-ion Batteries: Review and Future Challenges*. Electronics.

[157] Zhao, F. M., Gao, D. X., Cheng, Y. M., Yang, Q., & Liu, X. (2024). *Application of state of health estimation and remaining useful life prediction for lithium-ion batteries based on AT-CNN-BiLSTM*. Scientific Reports, 14, 29026.

[158] Xbattery Energy. (2026). *SOC vs SOH: Understanding the critical difference in battery health.*

[159] Ofoegbu, E. O. (2025). *State of charge (SOC) estimation in electric vehicle (EV) battery management systems using ensemble methods and neural networks*. Journal of Energy Storage, 114(Part B), Article 11583.

[160] von Bülow, F., & Meisen, T. (2023). *A review on methods for state of health forecasting of lithium-ion batteries applicable in real-world operational conditions*.

[161] Li, Y., Abdel-Monem, M., Gopalakrishnan, R., Berecibar, M., Nanini-Maury, E., Omar, N., van den Bossche, P., & Van Mierlo, J. (2018*). A quick on-line state of health estimation method for Li-ion battery with incremental capacity curves processed by Gaussian filter.* Journal of Power Sources, 373, 40–53.

[162] Chiang, Y.-H., Sean, W.-Y., & Ke, J.-C. (2011). *Online estimation of internal resistance and open-circuit voltage of lithium-ion batteries in electric vehicles*. Journal of Power Sources, 196(8), 3921–3932.

[163] Nuhic, A., Terzimehic, T., Soczka-Guth, T., Buchholz, M., & Dietmayer, K. (2013). *Health diagnosis and remaining useful life prognostics of lithium-ion batteries using data-driven methods*. Journal of Power Sources, 239, 680–688.

[164] Yang, S., Zhang, C., Jiang, J., Zhang, W., Zhang, L., & Wang, Y. (2021). *Review on state-of-health of lithium-ion batteries: Characterizations, estimations and applications*. Journal of Cleaner Production, 314, Article 128015.

[165] Wang, F., Liu, S., Chen, S, Zhang, Q., Wang, D., Ma, X., & Dai, X. (2025). *SOH estimation for lithium-ion batteries using the distribution of relaxation time and feature optimized multilayer perceptron.* iScience*, 28*(9), 113443.

[166] Liu, W., Placke, T., & Chau, K. T. (2022). *Overview of batteries and battery management for electric vehicles*. Energy Reports*, 8*, 4058–4084.

[167] Klink, R. (2025*). Review: Electrochemical impedance spectroscopy for lithium-ion batteries: Measurement and analysis (for automotive applications)*. Current Opinion in Electrochemistry, 41, Article 101498.

[168] Li, Q., Song, R., & Wei, Y. (2025). *A review of state-of-health estimation for lithium-ion battery packs*. Journal of Energy Storage, 118, Article 116078.

[169] Li, Y., Wang, L., Feng, Y., Liao, C., & Yang, J. (2024). *An online state-of-health estimation method for lithium-ion battery based on linear parameter-varying modeling framework*. Energy, 298, Article 131277.

[170] Hemavathi, S. (2025). *Lithium-ion battery state of health estimation using intelligent methods*. Franklin Open, 10, Article 100237.

[171] Mehta, C., Sant, A. V., & Sharma, P. (2021). *Analysis of state of health estimation for lithium-ion cell using unscented and extended Kalman filter*. Conference paper, Pandit Deendayal Energy University, Gandhinagar, India.

[172] Xie, J., Wei, X., Bo, X., Zhang, P., Chen, P., Hao, W., & Yuan, M. (2023). *State of charge estimation of lithium-ion battery based on extended Kalman filter algorithm*. Frontiers in Energy Research, 11, 1180881.

[173] Ahmed, F., Abdulsamad, K., & Massoud, A. M. (2025). *On equivalent circuit model-based state-of-charge estimation for lithium-ion batteries in electric vehicles*. IEEE Access, 13, 35065–35080.

[174] Fiveable. (2025). *State observers – Control Theory Unit 5 Class Notes*: https://fiveable.me/control-theory/unit-5/state-observers/studyguide/z1JGyPVYmDNr5jSp

[175] Liu, M., & Lu, Z. (2026). *A data-driven framework for lithium-ion battery SOH estimation using VMD-GRU hybrid approach with multi-scale feature analysis*. Energy Engineering, 123(3), 12.

[176] Rout, S., Samal, S. K., Gelmecha, D. J., Mishra, S., Shukla, V., & Ghosh, S. (2025). *Estimation of state of health for lithium-ion batteries using advanced data-driven techniques*. Scientific Reports, 15, 30438.

[177] Zhang, M., Yang, D., Du, J., Sun, H., Li, L., Wang, L., & Wang, K. (2023). *A review of SOH prediction of Li-ion batteries based on data-driven algorithms*. Energies, 16(7), 3167.

[178] Xu, G., Xu, J., & Zhu, Y. (2024). *LSTM-based estimation of lithium-ion battery SOH using data characteristics and spatio-temporal attention*. PLOS ONE, 19(12), e0312856.

[179] Li, X., Ju, L., Geng, G., & Jiang, Q. (2023). *Data-driven state-of-health estimation for lithium-ion battery based on aging features*. Energy, 274, 127378.

[180] Ye, Z., Deng, Z., Xu, Y., Lai, L., Zhang, R., Tong, L., Zhang, H., Li, Y., Gong, M., Liu, G., & Yan, M. (2025). *Joint estimation of SOC and SOH for lithium-ion batteries based on FOAMIUHF-UKF model*. Scientific Reports, 15, 40743.

[181] Google Developers. (n.d.). *Foreste decisionali casuali (Random forests)*. In Machine learning crash course, from: https://developers.google.com/machine-learning/decision-forests/random-forests

[182] Sapien. (n.d.). *Explanation of gradient boosting*. Sapien AI Glossary. From: https://www.sapien.io/glossary/definition/gradient-boosting

[183] NVIDIA. (2026). *XGBoost – What is it and why does it matter?* From: https://www.nvidia.com/en-in/glossary/xgboost/

[184] BatteryArchive.org. (n.d.). *BatteryArchive.org* [Data repository]. Retrieved 2 March 2026, from: https://batteryarchive.org/index.html

[185] Alamin, K., Jahier Pagliari, D., Chen, Y., Macii, E., Vinco, S., & Poncino, M. (2024). Model-driven feature engineering for data-driven battery SOH model. In *2024 Design, Automation & Test in Europe Conference & Exhibition (DATE)* (pp. 1–6). EDAA.

[186] Hu, H., Liang, C., Huang, X., Mo, H., Zou, C., & Tao, S. (2026). ONET: Operator network for randomized and robust battery health estimation using operation condition and cycling data matching. *Journal of Power Sources, 672*, 239592.

[187] Indeed Editorial Team. (2025, December 15). *What is 3 sigma in statistics? (And how to find it).* Indeed Career Guide. From: https://www.indeed.com/career-advice/career-development/3-sigma

[188] Zhang, X., Sun, J., Shang, Y., Ren, S., Liu, Y., & Wang, D. (2022). A novel state-of-health prediction method based on long short-term memory network with attention mechanism for lithium-ion battery. *Frontiers in Energy Research, 10*, 972486.

[189] LiFePO4 Battery. (2023, May 26). *What is 18650 lithium battery?* Retrieved March 3, 2026, from: https://www.lifepo4-battery.com/News/what-is-18650-battery.html

[190] Leng, F., Tan, C. M., & Pecht, M. (2015). *Effect of temperature on the aging rate of Li-ion battery operating above room temperature.* Scientific Reports, 5, 12967.

[191] Li, Z., Qu, Z., Jiang, Z., Huang, H., & Tao, W. (2025). *Degradation mechanism of lithium-ion battery under appropriate in-plane temperature gradient*. Green Energy and Intelligent Transportation, 4(6), 100352.

[192] Sun, S., Guan, T., Shen, B., Leng, K., Gao, Y., Cheng, X., & Yin, G. (2017). Changes of degradation mechanisms of LiFePO4/graphite batteries cycled at different ambient temperatures. *Electrochimica Acta*, 237, 248–258.

[193] Zhang, Y., Wang, C.-Y., & Tang, X. (2011). Cycling degradation of an automotive LiFePO4 lithium-ion battery. *Journal of Power Sources*, 196(3), 1513–1520.

[194] Wittman, R. (2022). *Systematic cycle and calendar aging of commercial 18650 LFP lithium-ion cells* (SAND2022-6841C). Sandia National Laboratories.

[195] Preger, Y., Barkholtz, H. M., Fresquez, A., Campbell, D. L., Juba, B. W., Romàn-Kustas, J., Ferreira, S. R., & Chalamala, B. (2020). Degradation of commercial lithium-ion cells as a function of chemistry and cycling conditions. *Journal of The Electrochemical Society, 167*(12), 120532.

[196] Kubal, J. J., Knehr, K. W., Susarla, N., Tornheim, A., Dunlop, A. R., Dees, D. D., Jansen, A. N., & Ahmed, S. (2022). The influence of temperature on area-specific impedance and capacity of Li-ion cells with nickel-containing positive electrodes. *Journal of Power Sources, 543*, 231864.

[197] Jaguemont, J., Darwiche, A., & Bardé, F. (2025). Complete electrothermal and lifetime model of 18650 nickel manganese cobalt cell based on artificial neural network. *Explora: Environment and Resource, 2*(1), 7228.

[198] Preger, Y., Barkholtz, H. M., Fresquez, A., Al Rashdan, A., Michelbacher, C., Hewson, J. C., Keyser, M., Pesaran, A., Smith, K., & Wood, E. (2020). Degradation of commercial lithium-ion cells as a function of chemistry and cycling conditions. *Journal of The Electrochemical Society, 167*(12), 120532.

[199] Preger, Y., Ruiz Diaz, D. F., Barkholtz, H. M., Fresquez, A., Campbell, D. L., Juba, B. W., Román-Kustas, J., Ferreira, S. R., Chalamala, B., & White, R. E. (2024). Characterization of cycle-aged commercial NMC and NCA lithium-ion batteries. *Journal of The Electrochemical Society, 171*(1), 010508.

[200] Wittman, R., Reed, D., Preger, Y., & Alamgir, M. (2022, October). Update on systematic cycle aging of NMC and NCA 18650 Li-ion batteries. In *Power Sources Conference 2022*. Sandia National Laboratories.

[201] Li, X., Wang, Y., Zhang, H., & Chen, R. (2025). Impact of low temperature exposure on lithium-ion batteries: A multi-scale study of performance degradation, predictive signals and underlying mechanisms. *Chemical Engineering Journal*. Advance online publication.

[202] Bloom, I., Preger, Y., & Dubarry, M. (2019). Characterization of cycle-aged commercial NMC and NCA lithium-ion batteries. *Journal of The Electrochemical Society, 166*(13), A3031–A3044.

[203] Thomas, A., Pelissier, S., Gyan, P., Venet, P., & Delaille, A. (2025). An ageing study of twenty 18650 lithium-ion Graphite/LFP cells in first and second life use. *Scientific Data, 12*, Article 123.

[204] Wittman, R., Fresquez, A., Chalamala, B., & Preger, Y. (2022, October). *Update on systematic cycle aging of NMC and NCA 18650 Li-ion batteries* (SAND2022-13700C) [Conference presentation]. 242nd ECS Meeting, Atlanta, GA, United States. Sandia National Laboratories.

Appendix A: MATLAB script for SOH estimation at 15°C with LFP chemistry

```
%% Advanced SOH Analysis - SNL 18650 LFP 15°C
clear all; close all; clc;
%% Import Data
filename = 'SNL_18650_LFP_15C_0-100_0.5-1C_a_cycle_data.xlsx';
opts = detectImportOptions(filename);
opts.VariableNamingRule = 'preserve';
data = readtable(filename, opts);
%% Extract data
nominal_capacity = 1.10;  % Ah
cycle_index = data{:, 1};
discharge_capacity = data{:, 10};
SOH_measured = data{:, 17};
SOH_calculated = (discharge_capacity / nominal_capacity) * 100;
%% Clean data - Remove NaN
valid_idx   =   ~isnan(cycle_index)   &   ~isnan(discharge_capacity)   &
~isnan(SOH_measured);
cycle_index        = cycle_index(valid_idx);
discharge_capacity = discharge_capacity(valid_idx);
SOH_calculated     = SOH_calculated(valid_idx);
SOH_measured       = SOH_measured(valid_idx);
%% Remove outliers - Filtro robusto
% Metodo 1: Rimuovi valori fuori range fisico
physical_limit_idx = (SOH_calculated >= 50) & (SOH_calculated <= 110);
cycle_clean        = cycle_index(physical_limit_idx);
SOH_clean          = SOH_calculated(physical_limit_idx);
SOH_meas_clean     = SOH_measured(physical_limit_idx);
discharge_clean    = discharge_capacity(physical_limit_idx);
% Metodo 2: Rimuovi outlier statistici (oltre 3 deviazioni standard)
mean_SOH    = mean(SOH_clean);
std_SOH     = std(SOH_clean);
outlier_idx = abs(SOH_clean - mean_SOH) < 3*std_SOH;
cycle_final     = cycle_clean(outlier_idx);
SOH_final       = SOH_clean(outlier_idx);
SOH_meas_final  = SOH_meas_clean(outlier_idx);
discharge_final = discharge_clean(outlier_idx);
fprintf('Raw data: %d | After Filtering: %d | Removed: %d outlier\n', ...
        length(cycle_index),  length(cycle_final),  length(cycle_index)-
length(cycle_final));
%% Smoothing con Moving Average
window = 10;
if length(cycle_final) > window
    SOH_smooth = movmean(SOH_final, window);
else
    SOH_smooth = SOH_final;
end
%% Fit lineari per ciascun dataset
p_raw      = polyfit(cycle_index, SOH_calculated, 1);
SOH_fit_raw = polyval(p_raw, cycle_index);
deg_rate_raw = abs(p_raw(1)) * 100;

p_filtered      = polyfit(cycle_final, SOH_final, 1);
SOH_fit_filtered = polyval(p_filtered, cycle_final);
```

```
deg_rate_filtered = abs(p_filtered(1)) * 100;

p_smooth      = polyfit(cycle_final, SOH_smooth, 1);
SOH_fit_smooth = polyval(p_smooth, cycle_final);
deg_rate_smooth = abs(p_smooth(1)) * 100;

% coefficienti di degradazione per ciclo (%/cycle)
k_raw      = abs(p_raw(1));      % % per ciclo
k_filtered = abs(p_filtered(1)); % % per ciclo
k_smooth   = abs(p_smooth(1));   % % per ciclo

fprintf('\n--- Degradation Coefficients (per cycle) ---\n');
fprintf('k_raw      = %.5f %%/cycle\n', k_raw);
fprintf('k_filtered = %.5f %%/cycle\n', k_filtered);
fprintf('k_smooth   = %.5f %%/cycle\n', k_smooth);

mdl_raw      = fitlm(cycle_index, SOH_calculated);
mdl_filtered = fitlm(cycle_final, SOH_final);
mdl_smooth   = fitlm(cycle_final, SOH_smooth);

R2_raw      = mdl_raw.Rsquared.Ordinary;
R2_filtered = mdl_filtered.Rsquared.Ordinary;
R2_smooth   = mdl_smooth.Rsquared.Ordinary;

fprintf('\n--- R-squared of Linear Fits ---\n');
fprintf('R2_raw      = %.4f\n', R2_raw);
fprintf('R2_filtered = %.4f\n', R2_filtered);
fprintf('R2_smooth   = %.4f\n', R2_smooth);

% Assumo SOH_meas_final come riferimento 'vero'
percent_error = abs(SOH_meas_final - SOH_final) ./ abs(SOH_meas_final) *
100;

mean_error = mean(percent_error);
max_error  = max(percent_error);

fprintf('\n--- Percentage Error (SOH_calculated vs SOH_measured) ---\n');
fprintf('Mean error = %.2f %%\n', mean_error);
fprintf('Max  error = %.2f %%\n', max_error);


%% ============================================================
%  FIGURA 1: Raw Data + Linear Fit
%% ============================================================
figure('Position', [100 100 1400 700]);
plot(cycle_index, SOH_calculated, 'Color', [0 0.5 0], 'LineWidth', 1.5);
hold on;
plot(cycle_index, SOH_fit_raw, 'k--', 'LineWidth', 2);
grid on;
ax = gca; ax.FontSize = 22; ax.TitleFontSizeMultiplier = 1.2;
xlabel('Cycle Number', 'FontSize', 24);
ylabel('SOH (%)', 'FontSize', 24);
T = title('Raw Data - LFP 18650 @ 15°C, 1C discharge', 'FontWeight',
'bold');
T.Units = 'normalized'; pos = T.Position;
T.Position = [pos(1) pos(2)+0.03 pos(3)];
legend('Raw Data', 'Linear Fit', 'Location', 'southwest');
xlim([min(cycle_index) max(cycle_index)]);
ylim([-20 200]);
```

```
%% ============================================================
%  FIGURA 2: Filtered Data + Linear Fit
%% ============================================================
figure('Position', [150 150 1400 700]);
plot(cycle_final, SOH_final, 'b-', 'LineWidth', 3);
hold on;
plot(cycle_final, SOH_fit_filtered, 'k--', 'LineWidth', 2);
grid on;
ax = gca; ax.FontSize = 20; ax.TitleFontSizeMultiplier = 1.2;
xlabel('Cycle Number', 'FontSize', 24);
ylabel('SOH (%)', 'FontSize', 24);
T = title('Filtered Data - LFP 18650 @ 15°C, 1C discharge', 'FontWeight',
'bold');
T.Units = 'normalized'; pos = T.Position;
T.Position = [pos(1) pos(2)+0.03 pos(3)];
legend('Filtered Data', 'Linear Fit', 'Location', 'southwest');
xlim([min(cycle_final) max(cycle_final)]);
ylim([80 100]);

%% ============================================================
%  FIGURA 3: Smoothed Data + Linear Fit
%% ============================================================
figure('Position', [200 200 1400 700]);
plot(cycle_final, SOH_smooth, 'r-', 'LineWidth', 3);
hold on;
plot(cycle_final, SOH_fit_smooth, 'k--', 'LineWidth', 2);
grid on;
ax = gca; ax.FontSize = 20; ax.TitleFontSizeMultiplier = 1.2;
xlabel('Cycle Number', 'FontSize', 24);
ylabel('SOH (%)', 'FontSize', 24);
T = title(sprintf('Smoothed Data (%d-cycle avg) - LFP 18650 @ 15°C, 1C
discharge', window), ...
          'FontWeight', 'bold');
T.Units = 'normalized'; pos = T.Position;
T.Position = [pos(1) pos(2)+0.03 pos(3)];
legend('Smoothed Data', 'Linear Fit', 'Location', 'southwest');
xlim([min(cycle_final) max(cycle_final)]);
ylim([80 100]);

%% ============================================================
%  EOL Calculation - (SOH = p(1)*cycle + p(2) → cycle = (80 - p(2)) / p(1))
%% ============================================================
EOL_threshold = 80;  % %

EOL_raw      = (EOL_threshold - p_raw(2))      / p_raw(1);
EOL_filtered = (EOL_threshold - p_filtered(2)) / p_filtered(1);
EOL_smooth   = (EOL_threshold - p_smooth(2))   / p_smooth(1);

remaining_raw      = EOL_raw      - cycle_index(end);
remaining_filtered = EOL_filtered - cycle_final(end);
remaining_smooth   = EOL_smooth   - cycle_final(end);

%% Summary Statistics
fprintf('\n========== SOH Analysis Summary ==========\n');
fprintf('Battery:   LFP   18650,   Nominal   Capacity:   %.2f   Ah\n',
nominal_capacity);
fprintf('Test Conditions: 15°C, 0.5C charge, 1C discharge\n');
fprintf('Total Cycles Analyzed: %d\n', length(cycle_final));
fprintf('\nInitial SOH:        %.2f%%\n', SOH_final(1));
fprintf('Final SOH:         %.2f%%\n', SOH_final(end));
```

```
fprintf('Total Capacity Loss: %.2f%%\n', SOH_final(1) - SOH_final(end));
fprintf('\n--- Degradation Rates ---\n');
fprintf('Raw Data:      %.3f %%/100 cycles\n', deg_rate_raw);
fprintf('Filtered Data: %.3f %%/100 cycles\n', deg_rate_filtered);
fprintf('Smoothed Data: %.3f %%/100 cycles\n', deg_rate_smooth);
fprintf('\n--- Projected EOL (SOH = %d%%) ---\n', EOL_threshold);
fprintf('Using Raw Data:       ~%.0f cycles  (%.0f remaining from last
measured cycle %d)\n', ...
        EOL_raw, remaining_raw, cycle_index(end));
fprintf('Using Filtered Data: ~%.0f cycles  (%.0f remaining from last
measured cycle %d)\n', ...
        EOL_filtered, remaining_filtered, cycle_final(end));
fprintf('Using Smoothed Data: ~%.0f cycles  (%.0f remaining from last
measured cycle %d)\n', ...
        EOL_smooth, remaining_smooth, cycle_final(end));
fprintf('========================================\n\n');
```

Appendix B: MATLAB script for SOH estimation at 25°C with LFP chemistry

```
%% Advanced SOH Analysis - SNL 18650 LFP 25°C
clear all; close all; clc;
%% Import Data
filename = 'SNL_18650_LFP_25C_0-100_0.5-1C_a_cycle_data.xlsx';
opts = detectImportOptions(filename);
opts.VariableNamingRule = 'preserve';
data = readtable(filename, opts);
%% Extract data
nominal_capacity = 1.10;  % Ah
cycle_index = data{:, 1};
discharge_capacity = data{:, 10};
SOH_calculated = (discharge_capacity / nominal_capacity) * 100;
%% Clean data - Remove NaN
valid_idx = ~isnan(cycle_index) & ~isnan(discharge_capacity);
cycle_index = cycle_index(valid_idx);
discharge_capacity = discharge_capacity(valid_idx);
SOH_calculated = SOH_calculated(valid_idx);
%% Remove outliers - Filtro robusto
% Metodo 1: Rimuovi valori fuori range fisico
physical_limit_idx = (SOH_calculated >= 50) & (SOH_calculated <= 110);
cycle_clean     = cycle_index(physical_limit_idx);
SOH_clean       = SOH_calculated(physical_limit_idx);
discharge_clean = discharge_capacity(physical_limit_idx);
% Metodo 2: Rimuovi outlier statistici (oltre 3 deviazioni standard)
mean_SOH    = mean(SOH_clean);
std_SOH     = std(SOH_clean);
outlier_idx = abs(SOH_clean - mean_SOH) < 3*std_SOH;
cycle_final     = cycle_clean(outlier_idx);
SOH_final       = SOH_clean(outlier_idx);
discharge_final = discharge_clean(outlier_idx);
fprintf('Raw data: %d | After Filtering: %d | Removed: %d outlier\n', ...
        length(cycle_index),  length(cycle_final),  length(cycle_index)-
length(cycle_final));
%% Smoothing con Moving Average
window = 10;
if length(cycle_final) > window
    SOH_smooth = movmean(SOH_final, window);
else
    SOH_smooth = SOH_final;
end
%% Fit lineare (su dati filtrati)
p        = polyfit(cycle_final, SOH_final, 1);
SOH_fit  = polyval(p, cycle_final);
deg_rate = abs(p(1)) * 100; % %/100 cycles

%% ============================================================
%  FIGURA 1: Smoothed Data + Linear Fit
%% ============================================================
figure('Position', [100 100 1400 700]);
plot(cycle_final, SOH_smooth, 'r-', 'LineWidth', 3);
hold on;
plot(cycle_final, SOH_fit, 'k--', 'LineWidth', 2);
grid on;
ax = gca;
```

```
ax.FontSize = 22;
ax.TitleFontSizeMultiplier = 1.2;
xlabel('Cycle Number', 'FontSize', 24);
ylabel('SOH (%)', 'FontSize', 24);
T = title(sprintf('Smoothed Data (%d-cycle avg) - LFP 18650 @ 25°C, 1C
discharge', window), ...
          'FontWeight', 'bold');
T.Units = 'normalized';
pos = T.Position;
T.Position = [pos(1) pos(2)+0.003 pos(3)];
legend(sprintf('Smoothed (%d-cycle avg)', window), 'Linear Fit', ...
       'Location', 'southwest', 'FontSize', 16);
xlim([min(cycle_final) max(cycle_final)]);
ylim([80 100]);
% text(max(cycle_final)*0.55, min(SOH_smooth)+1.5, ...
%      sprintf('Linear Fit: SOH = %.4f × cycle + %.2f\nDegradation Rate:
%.3f %%/100 cycles', ...
%      p(1), p(2), deg_rate), ...
%      'FontSize', 14, 'BackgroundColor', 'w', 'EdgeColor', 'k');

%% ============================================================
%  FIGURA 2: Filtered Data + Smoothed Data + Linear Fit
%% ============================================================
figure('Position', [150 150 1400 700]);
plot(cycle_final, SOH_final, 'b-', 'MarkerSize', 5);
hold on;
plot(cycle_final, SOH_smooth, 'r-', 'LineWidth', 3);
plot(cycle_final, SOH_fit, 'k--', 'LineWidth', 2);
grid on;
ax = gca;
ax.FontSize = 22;
ax.TitleFontSizeMultiplier = 1.2;
xlabel('Cycle Number', 'FontSize', 24);
ylabel('SOH (%)', 'FontSize', 24);
T = title('Filtered & Smoothed Data - LFP 18650 @ 25°C, 1C discharge', ...
          'FontWeight', 'bold');
T.Units = 'normalized';
pos = T.Position;
T.Position = [pos(1) pos(2)+0.003 pos(3)];
legend('Filtered  Data',  sprintf('Smoothed  (%d-cycle  avg)',  window),
'Linear Fit', ...
       'Location', 'southwest', 'FontSize', 16);
xlim([min(cycle_final) max(cycle_final)]);
ylim([80 100]);
% text(max(cycle_final)*0.55, min(SOH_final)+1.5, ...
%      sprintf('Linear Fit: SOH = %.4f × cycle + %.2f\nDegradation Rate:
%.3f %%/100 cycles', ...
%      p(1), p(2), deg_rate), ...
%      'FontSize', 14, 'BackgroundColor', 'w', 'EdgeColor', 'k');

%% Summary Statistics
fprintf('\n========== SOH Analysis Summary ==========\n');
fprintf('Battery:   LFP   18650,   Nominal   Capacity:   %.2f   Ah\n',
nominal_capacity);
fprintf('Test Conditions: 25°C, 0.5C charge, 1C discharge\n');
fprintf('Total Cycles Analyzed: %d\n', length(cycle_final));
fprintf('\nInitial SOH: %.2f%%\n', SOH_final(1));
fprintf('Final SOH: %.2f%%\n', SOH_final(end));
fprintf('Total Capacity Loss: %.2f%%\n', SOH_final(1) - SOH_final(end));
fprintf('Average Degradation Rate: %.4f %%/cycle\n', abs(p(1)));
```

```
fprintf('Average Degradation Rate: %.3f %%/100 cycles\n', deg_rate);
fprintf('\n--- Projected EOL (80%% SOH) ---\n');
fprintf('Using Filtered Data: ~%.0f cycles\n', (SOH_final(1) - 80) /
abs(p(1)));
fprintf('Using Smoothed Data: ~%.0f cycles\n', (SOH_smooth(1) - 80) /
abs(p(1)));
fprintf('========================================\n\n');
```

Appendix C: MATLAB script for SOH estimation at 35°C with LFP chemistry

```
%% Advanced SOH Analysis - SNL 18650 LFP 35°C
clear all; close all; clc;
%% Import Data
filename = 'SNL_18650_LFP_35C_0-100_0.5-1C_a_cycle_data.xlsx';
opts = detectImportOptions(filename);
opts.VariableNamingRule = 'preserve';
data = readtable(filename, opts);
%% Extract data
nominal_capacity = 1.10;  % Ah
cycle_index = data{:, 1};
discharge_capacity = data{:, 10};
SOH_calculated = (discharge_capacity / nominal_capacity) * 100;
%% Clean data - Remove NaN
valid_idx = ~isnan(cycle_index) & ~isnan(discharge_capacity);
cycle_index = cycle_index(valid_idx);
discharge_capacity = discharge_capacity(valid_idx);
SOH_calculated = SOH_calculated(valid_idx);
%% Remove outliers - Filtro robusto
% Metodo 1: Rimuovi valori fuori range fisico
physical_limit_idx = (SOH_calculated >= 50) & (SOH_calculated <= 110);
cycle_clean     = cycle_index(physical_limit_idx);
SOH_clean       = SOH_calculated(physical_limit_idx);
discharge_clean = discharge_capacity(physical_limit_idx);
% Metodo 2: Rimuovi outlier statistici (oltre 3 deviazioni standard)
mean_SOH    = mean(SOH_clean);
std_SOH     = std(SOH_clean);
outlier_idx = abs(SOH_clean - mean_SOH) < 3*std_SOH;
cycle_final     = cycle_clean(outlier_idx);
SOH_final       = SOH_clean(outlier_idx);
discharge_final = discharge_clean(outlier_idx);
fprintf('Raw data: %d | After Filtering: %d | Removed: %d outlier\n', ...
        length(cycle_index),  length(cycle_final),  length(cycle_index)-
length(cycle_final));
%% Smoothing con Moving Average
window = 10;
if length(cycle_final) > window
    SOH_smooth = movmean(SOH_final, window);
else
    SOH_smooth = SOH_final;
end
%% Fit lineare (su dati filtrati)
p        = polyfit(cycle_final, SOH_final, 1);
SOH_fit  = polyval(p, cycle_final);
deg_rate = abs(p(1)) * 100; % %/100 cycles

%% ============================================================
%  FIGURA 1: Smoothed Data + Linear Fit
%% ============================================================
figure('Position', [100 100 1400 700]);
plot(cycle_final, SOH_smooth, 'r-', 'LineWidth', 3);
hold on;
plot(cycle_final, SOH_fit, 'k--', 'LineWidth', 2);
grid on;
ax = gca;
```

```
ax.FontSize = 22;
ax.TitleFontSizeMultiplier = 1.2;
xlabel('Cycle Number', 'FontSize', 24);
ylabel('SOH (%)', 'FontSize', 24);
T = title(sprintf('Smoothed Data (%d-cycle avg) - LFP 18650 @ 35°C, 1C
discharge', window), ...
          'FontWeight', 'bold');
T.Units = 'normalized';
pos = T.Position;
T.Position = [pos(1) pos(2)+0.003 pos(3)];
legend(sprintf('Smoothed (%d-cycle avg)', window), 'Linear Fit', ...
       'Location', 'southwest', 'FontSize', 16);
xlim([min(cycle_final) max(cycle_final)]);
ylim([80' 100]);
% text(max(cycle_final)*0.55, min(SOH_smooth)+1.5, ...
%      sprintf('Linear Fit: SOH = %.4f × cycle + %.2f\nDegradation Rate:
%.3f %%/100 cycles', ...
%      p(1), p(2), deg_rate), ...
%      'FontSize', 14, 'BackgroundColor', 'w', 'EdgeColor', 'k');

%% ============================================================
%  FIGURA 2: Filtered Data + Smoothed Data + Linear Fit
%% ============================================================
figure('Position', [150 150 1400 700]);
plot(cycle_final, SOH_final, 'b.', 'MarkerSize', 5);
hold on;
plot(cycle_final, SOH_smooth, 'r-', 'LineWidth', 3);
plot(cycle_final, SOH_fit, 'k--', 'LineWidth', 2);
grid on;
ax = gca;
ax.FontSize = 22;
ax.TitleFontSizeMultiplier = 1.2;
xlabel('Cycle Number', 'FontSize', 24);
ylabel('SOH (%)', 'FontSize', 24);
T = title('Filtered & Smoothed Data - LFP 18650 @ 35°C, 1C discharge', ...
          'FontWeight', 'bold');
T.Units = 'normalized';
pos = T.Position;
T.Position = [pos(1) pos(2)+0.003 pos(3)];
legend('Filtered  Data',  sprintf('Smoothed  (%d-cycle  avg)',  window),
'Linear Fit', ...
       'Location', 'southwest', 'FontSize', 16);
xlim([min(cycle_final) max(cycle_final)]);
ylim([80 100]);
% text(max(cycle_final)*0.55, min(SOH_final)+1.5, ...
%      sprintf('Linear Fit: SOH = %.4f × cycle + %.2f\nDegradation Rate:
%.3f %%/100 cycles', ...
%      p(1), p(2), deg_rate), ...
%      'FontSize', 14, 'BackgroundColor', 'w', 'EdgeColor', 'k');

%% Summary Statistics
fprintf('\n========== SOH Analysis Summary ==========\n');
fprintf('Battery:   LFP   18650,   Nominal   Capacity:   %.2f   Ah\n',
nominal_capacity);
fprintf('Test Conditions: 35°C, 0.5C charge, 1C discharge\n');
fprintf('Total Cycles Analyzed: %d\n', length(cycle_final));
fprintf('\nInitial SOH: %.2f%%\n', SOH_final(1));
fprintf('Final SOH: %.2f%%\n', SOH_final(end));
fprintf('Total Capacity Loss: %.2f%%\n', SOH_final(1) - SOH_final(end));
fprintf('Average Degradation Rate: %.4f %%/cycle\n', abs(p(1)));
```

```
fprintf('Average Degradation Rate: %.3f %%/100 cycles\n', deg_rate);
fprintf('\n--- Projected EOL (80%% SOH) ---\n');
fprintf('Using Filtered Data: ~%.0f cycles\n', (SOH_final(1) - 80) /
abs(p(1)));
fprintf('Using Smoothed Data: ~%.0f cycles\n', (SOH_smooth(1) - 80) /
abs(p(1)));
fprintf('========================================\n\n');
```

Appendix D: MATLAB script for SOH estimation at 15°C, 25°C and 35°C together with LFP chemistry

```
%% SOH Comparison - SNL 18650 LFP: 15°C vs 25°C vs 35°C
clear all; close all; clc;

nominal_capacity = 1.10;
window = 10;

%% Seleziona i file manualmente tramite finestra di dialogo
disp('Seleziona il file 15°C...');
[f15, p15] = uigetfile('*.xlsx', 'Seleziona file 15°C');
filename_15 = fullfile(p15, f15);

disp('Seleziona il file 25°C...');
[f25, p25] = uigetfile('*.xlsx', 'Seleziona file 25°C');
filename_25 = fullfile(p25, f25);

disp('Seleziona il file 35°C...');
[f35, p35] = uigetfile('*.xlsx', 'Seleziona file 35°C');
filename_35 = fullfile(p35, f35);

%% ============================================================
%  LOAD & PROCESS - 15°C
%% ============================================================
opts = detectImportOptions(filename_15);
opts.VariableNamingRule = 'preserve';
data = readtable(filename_15, opts);

cycle_index        = data{:, 1};
discharge_capacity = data{:, 10};
SOH_calculated     = (discharge_capacity / nominal_capacity) * 100;

valid_idx          = ~isnan(cycle_index) & ~isnan(discharge_capacity);
cycle_index        = cycle_index(valid_idx);
SOH_calculated     = SOH_calculated(valid_idx);

physical_limit_idx = (SOH_calculated >= 50) & (SOH_calculated <= 110);
cycle_clean        = cycle_index(physical_limit_idx);
SOH_clean          = SOH_calculated(physical_limit_idx);

mean_SOH    = mean(SOH_clean);
std_SOH     = std(SOH_clean);
outlier_idx = abs(SOH_clean - mean_SOH) < 3*std_SOH;
cycle_15    = cycle_clean(outlier_idx);
SOH_15      = SOH_clean(outlier_idx);

if length(SOH_15) > window
    smooth_15 = movmean(SOH_15, window);
else
    smooth_15 = SOH_15;
end

fprintf('15°C - Raw: %d | After Filtering: %d | Removed: %d outlier\n',
...
```

```
        length(cycle_index),    length(cycle_15),    length(cycle_index)-
length(cycle_15));

%% ============================================================
%  LOAD & PROCESS - 25°C
%% ============================================================
opts = detectImportOptions(filename_25);
opts.VariableNamingRule = 'preserve';
data = readtable(filename_25, opts);

cycle_index        = data{:, 1};
discharge_capacity = data{:, 10};
SOH_calculated     = (discharge_capacity / nominal_capacity) * 100;

valid_idx          = ~isnan(cycle_index) & ~isnan(discharge_capacity);
cycle_index        = cycle_index(valid_idx);
SOH_calculated     = SOH_calculated(valid_idx);

physical_limit_idx = (SOH_calculated >= 50) & (SOH_calculated <= 110);
cycle_clean        = cycle_index(physical_limit_idx);
SOH_clean          = SOH_calculated(physical_limit_idx);

mean_SOH    = mean(SOH_clean);
std_SOH     = std(SOH_clean);
outlier_idx = abs(SOH_clean - mean_SOH) < 3*std_SOH;
cycle_25    = cycle_clean(outlier_idx);
SOH_25      = SOH_clean(outlier_idx);

if length(SOH_25) > window
    smooth_25 = movmean(SOH_25, window);
else
    smooth_25 = SOH_25;
end

fprintf('25°C - Raw: %d | After Filtering: %d | Removed: %d outlier\n',
...
        length(cycle_index),    length(cycle_25),    length(cycle_index)-
length(cycle_25));

%% ============================================================
%  LOAD & PROCESS - 35°C
%% ============================================================
opts = detectImportOptions(filename_35);
opts.VariableNamingRule = 'preserve';
data = readtable(filename_35, opts);

cycle_index        = data{:, 1};
discharge_capacity = data{:, 10};
SOH_calculated     = (discharge_capacity / nominal_capacity) * 100;

valid_idx          = ~isnan(cycle_index) & ~isnan(discharge_capacity);
cycle_index        = cycle_index(valid_idx);
SOH_calculated     = SOH_calculated(valid_idx);

physical_limit_idx = (SOH_calculated >= 50) & (SOH_calculated <= 110);
cycle_clean        = cycle_index(physical_limit_idx);
SOH_clean          = SOH_calculated(physical_limit_idx);

mean_SOH    = mean(SOH_clean);
std_SOH     = std(SOH_clean);
```

```
outlier_idx = abs(SOH_clean - mean_SOH) < 3*std_SOH;
cycle_35    = cycle_clean(outlier_idx);
SOH_35      = SOH_clean(outlier_idx);

if length(SOH_35) > window
    smooth_35 = movmean(SOH_35, window);
else
    smooth_35 = SOH_35;
end

fprintf('35°C - Raw: %d | After Filtering: %d | Removed: %d outlier\n',
...
        length(cycle_index),    length(cycle_35),    length(cycle_index)-
length(cycle_35));

%% ============================================================
%  FIGURA UNICA: Confronto SOH Smoothed 15°C vs 25°C vs 35°C
%% ============================================================
figure('Position', [100 100 1400 700]);
plot(cycle_15, smooth_15, 'r-', 'LineWidth', 3);
hold on;
plot(cycle_25, smooth_25, 'g-', 'LineWidth', 3);
plot(cycle_35, smooth_35, 'b-', 'LineWidth', 3);
grid on;

ax = gca;
ax.FontSize = 22;
ax.TitleFontSizeMultiplier = 1.2;
xlabel('Cycle Number', 'FontSize', 24);
ylabel('SOH (%)', 'FontSize', 24);
ylim([80 100]);

T = title(sprintf('SOH Comparison - LFP 18650, %d-cycle avg, 1C discharge',
window), ...
          'FontWeight', 'bold');
T.Units = 'normalized';
pos = T.Position;
T.Position = [pos(1) pos(2)+0.003 pos(3)];

legend('15°C', '25°C', '35°C', 'Location', 'southwest', 'FontSize', 20);

%% Summary Statistics
fprintf('\n========== SOH Comparison Summary ==========\n');
fprintf('Battery:   LFP   18650,   Nominal   Capacity:   %.2f   Ah\n',
nominal_capacity);
fprintf('Charge: 0.5C | Discharge: 1C\n\n');
fprintf('%-10s %-15s %-15s %-20s %-25s\n', ...
        'Temp', 'Cycles', 'Initial SOH', 'Final SOH', 'Total Capacity
Loss');
fprintf('%-10s %-15d %-15.2f %-20.2f %-25.2f\n', ...
        '15°C',    length(cycle_15),    smooth_15(1),    smooth_15(end),
smooth_15(1)-smooth_15(end));
fprintf('%-10s %-15d %-15.2f %-20.2f %-25.2f\n', ...
        '25°C',    length(cycle_25),    smooth_25(1),    smooth_25(end),
smooth_25(1)-smooth_25(end));
fprintf('%-10s %-15d %-15.2f %-20.2f %-25.2f\n', ...
        '35°C',    length(cycle_35),    smooth_35(1),    smooth_35(end),
smooth_35(1)-smooth_35(end));
fprintf('============================================\n\n');
```

Appendix E: MATLAB script for SOH estimation at 15°C with NMC chemistry

```
%% Advanced SOH Analysis - SNL 18650 NMC 15°C
clear all; close all; clc;

%% Import Data
filename = 'SNL_18650_NMC_15C_0-100_0.5-1C_a_cycle_data.xlsx';
opts = detectImportOptions(filename);
opts.VariableNamingRule = 'preserve';
data = readtable(filename, opts);

%% Extract data
nominal_capacity   = 3.0;  % Ah - NMC 18650
cycle_index        = data{:, 1};
discharge_capacity = data{:, 10};
SOH_measured       = data{:, 17};
SOH_calculated     = (discharge_capacity / nominal_capacity) * 100;

%% Clean data - Remove NaN
valid_idx   =   ~isnan(cycle_index)   &   ~isnan(discharge_capacity)   &
~isnan(SOH_measured);
cycle_index        = cycle_index(valid_idx);
discharge_capacity = discharge_capacity(valid_idx);
SOH_calculated     = SOH_calculated(valid_idx);
SOH_measured       = SOH_measured(valid_idx);

%% Remove outliers
physical_limit_idx = (SOH_calculated >= 50) & (SOH_calculated <= 110);
cycle_clean        = cycle_index(physical_limit_idx);
SOH_clean          = SOH_calculated(physical_limit_idx);
SOH_meas_clean     = SOH_measured(physical_limit_idx);
discharge_clean    = discharge_capacity(physical_limit_idx);

mean_SOH    = mean(SOH_clean);
std_SOH     = std(SOH_clean);
outlier_idx = abs(SOH_clean - mean_SOH) < 3*std_SOH;

cycle_final     = cycle_clean(outlier_idx);
SOH_final       = SOH_clean(outlier_idx);
SOH_meas_final  = SOH_meas_clean(outlier_idx);
discharge_final = discharge_clean(outlier_idx);

fprintf('Raw data: %d | After Filtering: %d | Removed: %d outlier\n', ...
        length(cycle_index),  length(cycle_final),  length(cycle_index)-
length(cycle_final));

%% Smoothing con Moving Average
window = 10;
if length(cycle_final) > window
    SOH_smooth = movmean(SOH_final, window);
else
    SOH_smooth = SOH_final;
end

%% Fit lineari (solo per visualizzazione)
p_raw             = polyfit(cycle_index, SOH_calculated, 1);
```

```
SOH_fit_raw       = polyval(p_raw, cycle_index);
deg_rate_raw      = abs(p_raw(1)) * 100;

p_filtered        = polyfit(cycle_final, SOH_final, 1);
SOH_fit_filtered  = polyval(p_filtered, cycle_final);
deg_rate_filtered = abs(p_filtered(1)) * 100;

p_smooth          = polyfit(cycle_final, SOH_smooth, 1);
SOH_fit_smooth    = polyval(p_smooth, cycle_final);
deg_rate_smooth   = abs(p_smooth(1)) * 100;

%% EOL Calculation - dal dato reale, non dal fit
EOL_threshold = 80;

idx_eol_raw    = find(SOH_calculated <= EOL_threshold, 1, 'first');
idx_eol_filt   = find(SOH_final      <= EOL_threshold, 1, 'first');
idx_eol_smooth = find(SOH_smooth     <= EOL_threshold, 1, 'first');

if ~isempty(idx_eol_raw),     EOL_raw        = cycle_index(idx_eol_raw);
else, EOL_raw      = NaN; end
if ~isempty(idx_eol_filt),    EOL_filtered = cycle_final(idx_eol_filt);
else, EOL_filtered = NaN; end
if       ~isempty(idx_eol_smooth),       EOL_smooth                    =
cycle_final(idx_eol_smooth);else, EOL_smooth   = NaN; end

remaining_raw      = EOL_raw      - cycle_index(end);
remaining_filtered = EOL_filtered - cycle_final(end);
remaining_smooth   = EOL_smooth   - cycle_final(end);

%% ============================================================
%  FIGURA 1: Raw Data + Linear Fit
%% ============================================================
figure('Position', [100 100 1400 700]);

plot(cycle_index, SOH_calculated, 'Color', [0 0.5 0], 'LineWidth', 1.5);
hold on;
plot(cycle_index, SOH_fit_raw, 'k--', 'LineWidth', 2);
yline(80, 'm--', 'LineWidth', 2);
if ~isnan(EOL_raw)
    xline(EOL_raw, 'm--', 'LineWidth', 2, ...
          'Label', sprintf('EoL @ cy %.0f', EOL_raw), ...
          'LabelVerticalAlignment', 'top', ...
          'LabelHorizontalAlignment', 'right', ...
          'FontSize', 16);
end

grid on;
ax = gca; ax.FontSize = 22; ax.TitleFontSizeMultiplier = 1.2;
xlabel('Cycle Number', 'FontSize', 24);
ylabel('SOH (%)', 'FontSize', 24);
T = title('Raw Data - NMC 18650 @ 15°C, 1C discharge', 'FontWeight',
'bold');
T.Units = 'normalized'; pos = T.Position;
T.Position = [pos(1) pos(2)+0.03 pos(3)];
legend('Raw Data', 'Linear Fit', 'SOH = 80% (EoL)', ...
       'Location', 'southwest', 'FontSize', 16);
xlim([min(cycle_index) max(cycle_index)]);
ylim([50 110]);

%% ============================================================
```

```
%  FIGURA 2: Filtered Data + Linear Fit
%% ============================================================
figure('Position', [150 150 1400 700]);

plot(cycle_final, SOH_final, 'b-', 'LineWidth', 3);
hold on;
plot(cycle_final, SOH_fit_filtered, 'k--', 'LineWidth', 2);
yline(80, 'm--', 'LineWidth', 2);
if ~isnan(EOL_filtered)
    xline(EOL_filtered, 'm--', 'LineWidth', 2, ...
          'Label', sprintf('EoL @ cy %.0f', EOL_filtered), ...
          'LabelVerticalAlignment', 'top', ...
          'LabelHorizontalAlignment', 'right', ...
          'FontSize', 16);
end

grid on;
ax = gca; ax.FontSize = 20; ax.TitleFontSizeMultiplier = 1.2;
xlabel('Cycle Number', 'FontSize', 24);
ylabel('SOH (%)', 'FontSize', 24);
T = title('Filtered Data - NMC 18650 @ 15°C, 1C discharge', 'FontWeight',
'bold');
T.Units = 'normalized'; pos = T.Position;
T.Position = [pos(1) pos(2)+0.03 pos(3)];
legend('Filtered Data', 'Linear Fit', 'SOH = 80% (EoL)', ...
       'Location', 'southwest', 'FontSize', 16);
xlim([min(cycle_final) max(cycle_final)]);
ylim([60 100]);

%% ============================================================
%  FIGURA 3: Smoothed Data + Linear Fit
%% ============================================================
figure('Position', [200 200 1400 700]);

plot(cycle_final, SOH_smooth, 'r-', 'LineWidth', 3);
hold on;
plot(cycle_final, SOH_fit_smooth, 'k--', 'LineWidth', 2);
yline(80, 'm--', 'LineWidth', 2);
if ~isnan(EOL_smooth)
    xline(EOL_smooth, 'm--', 'LineWidth', 2, ...
          'Label', sprintf('EoL @ cy %.0f', EOL_smooth), ...
          'LabelVerticalAlignment', 'top', ...
          'LabelHorizontalAlignment', 'right', ...
          'FontSize', 16);
end

grid on;
ax = gca; ax.FontSize = 20; ax.TitleFontSizeMultiplier = 1.2;
xlabel('Cycle Number', 'FontSize', 24);
ylabel('SOH (%)', 'FontSize', 24);
T = title(sprintf('Smoothed Data (%d-cycle avg) - NMC 18650 @ 15°C, 1C
discharge', window), ...
          'FontWeight', 'bold');
T.Units = 'normalized'; pos = T.Position;
T.Position = [pos(1) pos(2)+0.003 pos(3)];
legend('Smoothed Data', 'Linear Fit', 'SOH = 80% (EoL)', ...
       'Location', 'southwest', 'FontSize', 16);
xlim([min(cycle_final) max(cycle_final)]);
ylim([50 100]);
```

```
%% Summary Statistics
fprintf('\n========== SOH Analysis Summary ==========\n');
fprintf('Battery:   NMC   18650,   Nominal   Capacity:   %.2f   Ah\n',
nominal_capacity);
fprintf('Test Conditions: 15°C, 0.5C charge, 1C discharge\n');
fprintf('Total Cycles Analyzed: %d\n', length(cycle_final));
fprintf('\nInitial SOH:         %.2f%%\n', SOH_final(1));
fprintf('Final SOH:           %.2f%%\n', SOH_final(end));
fprintf('Total Capacity Loss: %.2f%%\n', SOH_final(1) - SOH_final(end));
fprintf('\n--- Degradation Rates (Linear Fit) ---\n');
fprintf('Raw Data:      %.3f %%/100 cycles\n', deg_rate_raw);
fprintf('Filtered Data: %.3f %%/100 cycles\n', deg_rate_filtered);
fprintf('Smoothed Data: %.3f %%/100 cycles\n', deg_rate_smooth);
fprintf('\n---  Projected  EOL  (SOH  =  %d%%,  dal  dato  reale)  ---\n',
EOL_threshold);
if ~isnan(EOL_raw)
    fprintf('Using Raw Data:       cycle %.0f  (%.0f remaining from cycle
%d)\n', ...
            EOL_raw, remaining_raw, cycle_index(end));
else
    fprintf('Using Raw Data:      EoL non raggiunto nel dataset\n');
end
if ~isnan(EOL_filtered)
    fprintf('Using Filtered Data: cycle %.0f  (%.0f remaining from cycle
%d)\n', ...
            EOL_filtered, remaining_filtered, cycle_final(end));
else
    fprintf('Using Filtered Data: EoL non raggiunto nel dataset\n');
end
if ~isnan(EOL_smooth)
    fprintf('Using Smoothed Data: cycle %.0f  (%.0f remaining from cycle
%d)\n', ...
            EOL_smooth, remaining_smooth, cycle_final(end));
else
    fprintf('Using Smoothed Data: EoL non raggiunto nel dataset\n');
end
fprintf('==========================================\n\n');
```

Appendix F: MATLAB script for SOH estimation at 25°C with NMC chemistry

```
%% Advanced SOH Analysis - SNL 18650 NMC 25°C
clear all; close all; clc;

%% Import Data
filename = 'SNL_18650_NMC_25C_0-100_0.5-1C_a_cycle_data.xlsx';
opts = detectImportOptions(filename);
opts.VariableNamingRule = 'preserve';
data = readtable(filename, opts);

%% Extract data
nominal_capacity   = 3.0;
cycle_index        = data{:, 1};
discharge_capacity = data{:, 10};
SOH_calculated     = (discharge_capacity / nominal_capacity) * 100;

%% Clean data - Remove NaN
valid_idx          = ~isnan(cycle_index) & ~isnan(discharge_capacity);
cycle_index        = cycle_index(valid_idx);
discharge_capacity = discharge_capacity(valid_idx);
SOH_calculated     = SOH_calculated(valid_idx);

%% Remove outliers
physical_limit_idx = (SOH_calculated >= 50) & (SOH_calculated <= 110);
cycle_clean        = cycle_index(physical_limit_idx);
SOH_clean          = SOH_calculated(physical_limit_idx);
discharge_clean    = discharge_capacity(physical_limit_idx);

mean_SOH    = mean(SOH_clean);
std_SOH     = std(SOH_clean);
outlier_idx = abs(SOH_clean - mean_SOH) < 3*std_SOH;

cycle_final     = cycle_clean(outlier_idx);
SOH_final       = SOH_clean(outlier_idx);
discharge_final = discharge_clean(outlier_idx);

fprintf('Raw data: %d | After Filtering: %d | Removed: %d outlier\n', ...
        length(cycle_index),  length(cycle_final),  length(cycle_index)-
length(cycle_final));

%% Smoothing
window = 10;
if length(cycle_final) > window
    SOH_smooth = movmean(SOH_final, window);
else
    SOH_smooth = SOH_final;
end

%% Fit lineare (solo visualizzazione)
p        = polyfit(cycle_final, SOH_final, 1);
SOH_fit  = polyval(p, cycle_final);
deg_rate = abs(p(1)) * 100;

%% EOL Calculation - dal dato SMOOTHED reale, non dal fit
EOL_threshold = 80;
```

```
eol_idx = find(SOH_smooth <= EOL_threshold, 1, 'first');

if ~isempty(eol_idx)
    EOL_cycle  = cycle_final(eol_idx);
    EOL_source = 'actual';
    remaining  = 0;
    fprintf('EOL reached in dataset at cycle %d (SOH_smooth = %.2f%%)\n',
...
            EOL_cycle, SOH_smooth(eol_idx));
else
    EOL_cycle  = (EOL_threshold - p(2)) / p(1);
    EOL_source = 'projected';
    remaining  = EOL_cycle - cycle_final(end);
    fprintf('EOL not reached in dataset. Projected at cycle ~%.0f (%.0f
remaining)\n', ...
            EOL_cycle, remaining);
end

if strcmp(EOL_source, 'actual')
    eol_label = sprintf('EOL @ cycle %d (actual)', EOL_cycle);
else
    eol_label = sprintf('EOL @ cycle %.0f (projected)', EOL_cycle);
end

%% ============================================================
%  FIGURA 1: Smoothed Data + Linear Fit
%% ============================================================
figure('Position', [100 100 1400 700]);

plot(cycle_final, SOH_smooth, 'r-', 'LineWidth', 3);
hold on;
plot(cycle_final, SOH_fit, 'k--', 'LineWidth', 2);

% Linea orizzontale SOH = 80%
yline(80, 'm--', 'LineWidth', 2);

% Linea verticale al ciclo in cui SOH_smooth tocca 80%
if strcmp(EOL_source, 'actual')
    xline(EOL_cycle, 'm-', 'LineWidth', 2, ...
          'Label', sprintf('EoL @ cy %d', EOL_cycle), ...
          'LabelVerticalAlignment', 'top', ...
          'LabelHorizontalAlignment', 'right', ...
          'FontSize', 16);
else
    xline(EOL_cycle, 'm--', 'LineWidth', 2, ...
          'Label', sprintf('EoL @ cy %.0f (proj.)', EOL_cycle), ...
          'LabelVerticalAlignment', 'top', ...
          'LabelHorizontalAlignment', 'right', ...
          'FontSize', 16);
end

plot(nan, nan, 'm--', 'LineWidth', 2);  % dummy legenda

grid on;
ax = gca; ax.FontSize = 22; ax.TitleFontSizeMultiplier = 1.2;
xlabel('Cycle Number', 'FontSize', 24);
ylabel('SOH (%)', 'FontSize', 24);
T = title(sprintf('Smoothed Data (%d-cycle avg) - NMC 18650 @ 25°C, 1C
discharge', window), ...
          'FontWeight', 'bold');
```

```
T.Units = 'normalized'; pos = T.Position;
T.Position = [pos(1) pos(2)+0.003 pos(3)];
legend(sprintf('Smoothed (%d-cycle avg)', window), 'Linear Fit', ...
       'SOH = 80% (EoL)', eol_label, ...
       'Location', 'southwest', 'FontSize', 16);
xlim([min(cycle_final) max(cycle_final)]);
ylim([75 105]);

%% ============================================================
%  FIGURA 2: Filtered + Smoothed + Linear Fit
%% ============================================================
figure('Position', [150 150 1400 700]);

plot(cycle_final, SOH_final,  'b-', 'LineWidth', 1.5);
hold on;
plot(cycle_final, SOH_smooth, 'r-', 'LineWidth', 3);
plot(cycle_final, SOH_fit,    'k--', 'LineWidth', 2);

% Linea orizzontale SOH = 80%
yline(80, 'm--', 'LineWidth', 2);

% Linea verticale al ciclo in cui SOH_smooth tocca 80%
if strcmp(EOL_source, 'actual')
    xline(EOL_cycle, 'm-', 'LineWidth', 2, ...
          'Label', sprintf('EoL @ cy %d', EOL_cycle), ...
          'LabelVerticalAlignment', 'top', ...
          'LabelHorizontalAlignment', 'right', ...
          'FontSize', 16);
else
    xline(EOL_cycle, 'm--', 'LineWidth', 2, ...
          'Label', sprintf('EoL @ cy %.0f (proj.)', EOL_cycle), ...
          'LabelVerticalAlignment', 'top', ...
          'LabelHorizontalAlignment', 'right', ...
          'FontSize', 16);
end

plot(nan, nan, 'm--', 'LineWidth', 2);  % dummy legenda

grid on;
ax = gca; ax.FontSize = 22; ax.TitleFontSizeMultiplier = 1.2;
xlabel('Cycle Number', 'FontSize', 24);
ylabel('SOH (%)', 'FontSize', 24);
T = title('Filtered & Smoothed Data - NMC 18650 @ 25°C, 1C discharge',
'FontWeight', 'bold');
T.Units = 'normalized'; pos = T.Position;
T.Position = [pos(1) pos(2)+0.003 pos(3)];
legend('Filtered  Data',  sprintf('Smoothed  (%d-cycle  avg)',  window),
'Linear Fit', ...
       'SOH = 80% (EoL)', eol_label, ...
       'Location', 'southwest', 'FontSize', 16);
xlim([min(cycle_final) max(cycle_final)]);
ylim([75 105]);

%% Summary Statistics
fprintf('\n========== SOH Analysis Summary ==========\n');
fprintf('Battery:   NMC   18650,   Nominal   Capacity:   %.2f   Ah\n',
nominal_capacity);
fprintf('Test Conditions: 25°C, 0.5C charge, 1C discharge\n');
fprintf('Total Cycles Analyzed: %d\n', length(cycle_final));
fprintf('\nInitial SOH:        %.2f%%\n', SOH_final(1));
```

```
fprintf('Final SOH:           %.2f%%\n', SOH_final(end));
fprintf('Total Capacity Loss: %.2f%%\n', SOH_final(1) - SOH_final(end));
fprintf('Degradation Rate:    %.4f %%/cycle\n', abs(p(1)));
fprintf('Degradation Rate:    %.3f %%/100 cycles\n', deg_rate);
fprintf('\n--- EOL (SOH = %d%%) ---\n', EOL_threshold);
if strcmp(EOL_source, 'actual')
    fprintf('EOL source: ACTUAL (observed in smoothed data)\n');
    fprintf('EOL  cycle:    %d    (SOH_smooth  =  %.2f%%)\n',  EOL_cycle,
SOH_smooth(eol_idx));
else
    fprintf('EOL source: PROJECTED (linear fit extrapolation)\n');
    fprintf('EOL cycle:  ~%.0f  (%.0f remaining from cycle %d)\n', ...
            EOL_cycle, remaining, cycle_final(end));
end
fprintf('========================================\n\n');
```

Appendix G: MATLAB script for SOH estimation at 35°C with NMC chemistry

```
%% Advanced SOH Analysis - SNL 18650 NMC 35°C
clear all; close all; clc;

%% Import Data
filename = 'SNL_18650_NMC_35C_0-100_0.5-1C_a_cycle_data.xlsx';
opts = detectImportOptions(filename);
opts.VariableNamingRule = 'preserve';
data = readtable(filename, opts);

%% Extract data
nominal_capacity   = 3.0;
cycle_index        = data{:, 1};
discharge_capacity = data{:, 10};
SOH_calculated     = (discharge_capacity / nominal_capacity) * 100;

%% Clean data - Remove NaN
valid_idx          = ~isnan(cycle_index) & ~isnan(discharge_capacity);
cycle_index        = cycle_index(valid_idx);
discharge_capacity = discharge_capacity(valid_idx);
SOH_calculated     = SOH_calculated(valid_idx);

%% Remove outliers
physical_limit_idx = (SOH_calculated >= 50) & (SOH_calculated <= 110);
cycle_clean        = cycle_index(physical_limit_idx);
SOH_clean          = SOH_calculated(physical_limit_idx);
discharge_clean    = discharge_capacity(physical_limit_idx);

mean_SOH    = mean(SOH_clean);
std_SOH     = std(SOH_clean);
outlier_idx = abs(SOH_clean - mean_SOH) < 3*std_SOH;

cycle_final     = cycle_clean(outlier_idx);
SOH_final       = SOH_clean(outlier_idx);
discharge_final = discharge_clean(outlier_idx);

fprintf('Raw data: %d | After Filtering: %d | Removed: %d outlier\n', ...
        length(cycle_index),  length(cycle_final),  length(cycle_index)-
length(cycle_final));

%% Smoothing
window = 10;
if length(cycle_final) > window
    SOH_smooth = movmean(SOH_final, window);
else
    SOH_smooth = SOH_final;
end

%% Fit lineare (solo visualizzazione)
p        = polyfit(cycle_final, SOH_final, 1);
SOH_fit  = polyval(p, cycle_final);
deg_rate = abs(p(1)) * 100;

%% EOL Calculation - dal dato SMOOTHED (curva rossa), non dal fit
EOL_threshold = 80;
```

```
eol_idx = find(SOH_smooth <= EOL_threshold, 1, 'first');

if ~isempty(eol_idx)
    EOL_cycle  = cycle_final(eol_idx);
    EOL_source = 'actual';
    remaining  = 0;
    fprintf('EOL reached in dataset at cycle %d (SOH_smooth = %.2f%%)\n',
...
            EOL_cycle, SOH_smooth(eol_idx));
else
    EOL_cycle  = (EOL_threshold - p(2)) / p(1);
    EOL_source = 'projected';
    remaining  = EOL_cycle - cycle_final(end);
    fprintf('EOL not reached in dataset. Projected at cycle ~%.0f (%.0f
remaining)\n', ...
            EOL_cycle, remaining);
end

if strcmp(EOL_source, 'actual')
    eol_label = sprintf('EOL @ cycle %d (actual)', EOL_cycle);
else
    eol_label = sprintf('EOL @ cycle %.0f (projected)', EOL_cycle);
end

%% ============================================================
%  FIGURA 1: Smoothed Data + Linear Fit
%% ============================================================
figure('Position', [100 100 1400 700]);

plot(cycle_final, SOH_smooth, 'r-', 'LineWidth', 3);
hold on;
plot(cycle_final, SOH_fit, 'k--', 'LineWidth', 2);

% Linea orizzontale SOH = 80%
yline(80, 'm--', 'LineWidth', 2);

% Linea verticale al ciclo in cui SOH_smooth tocca 80%
if strcmp(EOL_source, 'actual')
    xline(EOL_cycle, 'm-', 'LineWidth', 2, ...
          'Label', sprintf('EoL @ cy %d', EOL_cycle), ...
          'LabelVerticalAlignment', 'top', ...
          'LabelHorizontalAlignment', 'right', ...
          'FontSize', 16);
else
    xline(EOL_cycle, 'm--', 'LineWidth', 2, ...
          'Label', sprintf('EoL @ cy %.0f (proj.)', EOL_cycle), ...
          'LabelVerticalAlignment', 'top', ...
          'LabelHorizontalAlignment', 'right', ...
          'FontSize', 16);
end

plot(nan, nan, 'm--', 'LineWidth', 2);  % dummy per legenda

grid on;
ax = gca; ax.FontSize = 22; ax.TitleFontSizeMultiplier = 1.2;
xlabel('Cycle Number', 'FontSize', 24);
ylabel('SOH (%)', 'FontSize', 24);
T = title(sprintf('Smoothed Data (%d-cycle avg) - NMC 18650 @ 35°C, 1C
discharge', window), ...
          'FontWeight', 'bold');
```

```
T.Units = 'normalized'; pos = T.Position;
T.Position = [pos(1) pos(2)+0.003 pos(3)];
legend(sprintf('Smoothed (%d-cycle avg)', window), 'Linear Fit', ...
       'SOH = 80% (EoL)', eol_label, ...
       'Location', 'southwest', 'FontSize', 16);
xlim([min(cycle_final) max(cycle_final)]);
ylim([70 105]);

%% ============================================================
%  FIGURA 2: Filtered + Smoothed + Linear Fit
%% ============================================================
figure('Position', [150 150 1400 700]);

plot(cycle_final, SOH_final,  'b-', 'LineWidth', 1.5);
hold on;
plot(cycle_final, SOH_smooth, 'r-', 'LineWidth', 3);
plot(cycle_final, SOH_fit,    'k--', 'LineWidth', 2);

% Linea orizzontale SOH = 80%
yline(80, 'm--', 'LineWidth', 2);

% Linea verticale al ciclo in cui SOH_smooth tocca 80%
if strcmp(EOL_source, 'actual')
    xline(EOL_cycle, 'm-', 'LineWidth', 2, ...
          'Label', sprintf('EoL @ cy %d', EOL_cycle), ...
          'LabelVerticalAlignment', 'top', ...
          'LabelHorizontalAlignment', 'right', ...
          'FontSize', 16);
else
    xline(EOL_cycle, 'm--', 'LineWidth', 2, ...
          'Label', sprintf('EoL @ cy %.0f (proj.)', EOL_cycle), ...
          'LabelVerticalAlignment', 'top', ...
          'LabelHorizontalAlignment', 'right', ...
          'FontSize', 16);
end

plot(nan, nan, 'm--', 'LineWidth', 2);  % dummy per legenda

grid on;
ax = gca; ax.FontSize = 22; ax.TitleFontSizeMultiplier = 1.2;
xlabel('Cycle Number', 'FontSize', 24);
ylabel('SOH (%)', 'FontSize', 24);
T = title('Filtered & Smoothed Data - NMC 18650 @ 35°C, 1C discharge',
'FontWeight', 'bold');
T.Units = 'normalized'; pos = T.Position;
T.Position = [pos(1) pos(2)+0.003 pos(3)];
legend('Filtered  Data',  sprintf('Smoothed  (%d-cycle  avg)',  window),
'Linear Fit', ...
       'SOH = 80% (EoL)', eol_label, ...
       'Location', 'southwest', 'FontSize', 16);
xlim([min(cycle_final) max(cycle_final)]);
ylim([50 105]);

%% Summary Statistics
fprintf('\n========== SOH Analysis Summary ==========\n');
fprintf('Battery:   NMC   18650,   Nominal   Capacity:   %.2f   Ah\n',
nominal_capacity);
fprintf('Test Conditions: 35°C, 0.5C charge, 1C discharge\n');
fprintf('Total Cycles Analyzed: %d\n', length(cycle_final));
fprintf('\nInitial SOH:        %.2f%%\n', SOH_final(1));
```

```
fprintf('Final SOH:           %.2f%%\n', SOH_final(end));
fprintf('Total Capacity Loss: %.2f%%\n', SOH_final(1) - SOH_final(end));
fprintf('Degradation Rate:    %.4f %%/cycle\n', abs(p(1)));
fprintf('Degradation Rate:    %.3f %%/100 cycles\n', deg_rate);
fprintf('\n--- EOL (SOH = %d%%) ---\n', EOL_threshold);
if strcmp(EOL_source, 'actual')
    fprintf('EOL source: ACTUAL (observed in smoothed data)\n');
    fprintf('EOL  cycle:    %d    (SOH_smooth  =  %.2f%%)\n',  EOL_cycle,
SOH_smooth(eol_idx));
else
    fprintf('EOL source: PROJECTED (linear fit extrapolation)\n');
    fprintf('EOL cycle:  ~%.0f  (%.0f remaining from cycle %d)\n', ...
            EOL_cycle, remaining, cycle_final(end));
end
fprintf('========================================\n\n');
```

Appendix H: MATLAB script for SOH estimation at 15°C, 25°C and 35°C together with NMC chemistry

```
%% SOH Comparison - SNL 18650 NMC: 15°C vs 25°C vs 35°C
clear all; close all; clc;

nominal_capacity = 3.00;   % Ah - NMC 18650
window           = 10;

%% Seleziona i file manualmente tramite finestra di dialogo
disp('Seleziona il file 15°C...');
[f15, p15] = uigetfile('*.xlsx', 'Seleziona file 15°C');
filename_15 = fullfile(p15, f15);

disp('Seleziona il file 25°C...');
[f25, p25] = uigetfile('*.xlsx', 'Seleziona file 25°C');
filename_25 = fullfile(p25, f25);

disp('Seleziona il file 35°C...');
[f35, p35] = uigetfile('*.xlsx', 'Seleziona file 35°C');
filename_35 = fullfile(p35, f35);

%% ============================================================
%  LOAD & PROCESS - 15°C
%% ============================================================
opts = detectImportOptions(filename_15);
opts.VariableNamingRule = 'preserve';
data = readtable(filename_15, opts);

cycle_index        = data{:, 1};
discharge_capacity = data{:, 10};
SOH_calculated     = (discharge_capacity / nominal_capacity) * 100;

valid_idx      = ~isnan(cycle_index) & ~isnan(discharge_capacity);
cycle_index    = cycle_index(valid_idx);
SOH_calculated = SOH_calculated(valid_idx);

physical_limit_idx = (SOH_calculated >= 50) & (SOH_calculated <= 110);
cycle_clean        = cycle_index(physical_limit_idx);
SOH_clean          = SOH_calculated(physical_limit_idx);

mean_SOH    = mean(SOH_clean);
std_SOH     = std(SOH_clean);
outlier_idx = abs(SOH_clean - mean_SOH) < 3*std_SOH;

cycle_15 = cycle_clean(outlier_idx);
SOH_15   = SOH_clean(outlier_idx);

if length(SOH_15) > window
    smooth_15 = movmean(SOH_15, window);
else
    smooth_15 = SOH_15;
end
```

```
fprintf('15°C - Raw: %d | After Filtering: %d | Removed: %d outlier\n',
...
        length(cycle_index),    length(cycle_15),    length(cycle_index)-
length(cycle_15));

%% ============================================================
%  LOAD & PROCESS - 25°C
%% ============================================================
opts = detectImportOptions(filename_25);
opts.VariableNamingRule = 'preserve';
data = readtable(filename_25, opts);

cycle_index        = data{:, 1};
discharge_capacity = data{:, 10};
SOH_calculated     = (discharge_capacity / nominal_capacity) * 100;

valid_idx      = ~isnan(cycle_index) & ~isnan(discharge_capacity);
cycle_index    = cycle_index(valid_idx);
SOH_calculated = SOH_calculated(valid_idx);

physical_limit_idx = (SOH_calculated >= 50) & (SOH_calculated <= 110);
cycle_clean        = cycle_index(physical_limit_idx);
SOH_clean          = SOH_calculated(physical_limit_idx);

mean_SOH    = mean(SOH_clean);
std_SOH     = std(SOH_clean);
outlier_idx = abs(SOH_clean - mean_SOH) < 3*std_SOH;

cycle_25 = cycle_clean(outlier_idx);
SOH_25   = SOH_clean(outlier_idx);

if length(SOH_25) > window
    smooth_25 = movmean(SOH_25, window);
else
    smooth_25 = SOH_25;
end

fprintf('25°C - Raw: %d | After Filtering: %d | Removed: %d outlier\n',
...
        length(cycle_index),    length(cycle_25),    length(cycle_index)-
length(cycle_25));

%% ============================================================
%  LOAD & PROCESS - 35°C
%% ============================================================
opts = detectImportOptions(filename_35);
opts.VariableNamingRule = 'preserve';
data = readtable(filename_35, opts);

cycle_index        = data{:, 1};
discharge_capacity = data{:, 10};
SOH_calculated     = (discharge_capacity / nominal_capacity) * 100;

valid_idx      = ~isnan(cycle_index) & ~isnan(discharge_capacity);
cycle_index    = cycle_index(valid_idx);
SOH_calculated = SOH_calculated(valid_idx);

physical_limit_idx = (SOH_calculated >= 50) & (SOH_calculated <= 110);
cycle_clean        = cycle_index(physical_limit_idx);
SOH_clean          = SOH_calculated(physical_limit_idx);
```

```
mean_SOH    = mean(SOH_clean);
std_SOH     = std(SOH_clean);
outlier_idx = abs(SOH_clean - mean_SOH) < 3*std_SOH;

cycle_35 = cycle_clean(outlier_idx);
SOH_35   = SOH_clean(outlier_idx);

if length(SOH_35) > window
    smooth_35 = movmean(SOH_35, window);
else
    smooth_35 = SOH_35;
end

fprintf('35°C - Raw: %d | After Filtering: %d | Removed: %d outlier\n',
...
        length(cycle_index),    length(cycle_35),    length(cycle_index)-
length(cycle_35));

%% ============================================================
%  FIGURA UNICA: Confronto SOH Smoothed 15°C vs 25°C vs 35°C
%% ============================================================
figure('Position', [100 100 1400 700]);

plot(cycle_15, smooth_15, 'r-', 'LineWidth', 3); hold on;
plot(cycle_25, smooth_25, 'g-', 'LineWidth', 3);
plot(cycle_35, smooth_35, 'b-', 'LineWidth', 3);

% --- Soglia End-of-Life: SOH = 80% ---
yline(80, 'm--', 'LineWidth', 2);

grid on;
ax = gca;
ax.FontSize = 22;
ax.TitleFontSizeMultiplier = 1.2;

xlabel('Cycle Number', 'FontSize', 24);
ylabel('SOH (%)', 'FontSize', 24);
ylim([50 100]);   % abbassato a 78 per mostrare la linea 80% con margine

T = title(sprintf('SOH Comparison – NMC 18650, %d-cycle avg, 1C discharge',
window), ...
          'FontWeight', 'bold');
T.Units   = 'normalized';
pos       = T.Position;
T.Position = [pos(1) pos(2)+0.003 pos(3)];

legend('15°C', '25°C', '35°C', 'SOH = 80% (EoL)', ...
       'Location', 'southwest', 'FontSize', 20);

%% Summary Statistics
fprintf('\n========== SOH Comparison Summary ==========\n');
fprintf('Battery:   NMC   18650,   Nominal   Capacity:   %.2f   Ah\n',
nominal_capacity);
fprintf('Charge: 0.5C | Discharge: 1C\n\n');

fprintf('%-10s %-15s %-15s %-20s %-25s\n', ...
        'Temp', 'Cycles', 'Initial SOH', 'Final SOH', 'Total Capacity
Loss');
```

```
fprintf('%-10s %-15d %-15.2f %-20.2f %-25.2f\n', ...
        '15°C',    length(cycle_15),    smooth_15(1),    smooth_15(end),
smooth_15(1)-smooth_15(end));
fprintf('%-10s %-15d %-15.2f %-20.2f %-25.2f\n', ...
        '25°C',    length(cycle_25),    smooth_25(1),    smooth_25(end),
smooth_25(1)-smooth_25(end));
fprintf('%-10s %-15d %-15.2f %-20.2f %-25.2f\n', ...
        '35°C',    length(cycle_35),    smooth_35(1),    smooth_35(end),
smooth_35(1)-smooth_35(end));

fprintf('=============================================\n\n');
```